The defect structure and magnetic ground state of ytterbium titanate

David Fielding Bowman

A thesis submitted to the

University of London

for the degree of Doctor of Philosophy

Department of Physics

Royal Holloway, University of London

June 29, 2018

Declaration of Authorship

I, David Fielding Bowman, hereby declare that this thesis and the work presented in it, is entirely my own. Where I have consulted the work of others, I have clearly stated as such.

Sign: .....

Abstract

The pyrochlore lattice is ideally suited to the exploration of geometrical frustration in three dimensions, and provide the first context in which to study emergent magnetic monopoles. For the quantum analogue of this system, $Yb_2Ti_2O_7$, whether the magnetic ground state assumes a quantum spin ice state or a Higgs transition to a ferromagnetic phase appears to be sample dependent.

Here the defect structure of $Yb_2Ti_2O_7$ has been characterised and understood using single crystal diffuse scattering obtained on SXD along with balls and springs Monte Carlo modelling. The results show diffuse scattering different to that of other pyrochlores like $Y_2Ti_2O_7$. In both stuffed and oxygen depleted samples vacancies are appear to be present on the 48f oxygen sites. Annealing was found to eliminate the structural diffuse scattering in an as-grown sample indicating the dominant role of isolated oxygen vacancies.

The magnetism of the $Yb_2Ti_2O_7$ samples was determined using polarised diffuse neutron scattering on D7. The as-grown sample exhibits the magnetic diffuse scattering features observed in previous measurements of $Yb_2Ti_2O_7$ while annealing in oxygen gives a ferromagnetic ground state. Hence, the true ground state of stoichiometric $Yb_2Ti_2O_7$ is ferromagnetic and analysis of the peak intensities compared to the existing literature found that ferromagnetism to be all-in all-out. The diffuse scattering observed in the as-grown sample persists in a heavily oxygen depleted sample while stuffing shows suppression of the correlations from the Coulomb phase.

Acknowledgements

I would first and foremost like to thank my supervisor Professor Jon Goff who consistently went above and beyond in supporting and advising me during the project. My research group Dan, David, Toby, Eron, Uthay and Gabriele also all contributed massively in providing their time, expertise and friendship.

Having been at Royal Holloway for eight years I am acutely aware of the hard work done by the administrative staff and the workshop team, who were always on hand to help me out. On SXD the instrument scientists Matthias and Silvia and on D7, Andrew, Goran and Lucile were happy to answer the phone at unsociable hours and help put out fires, sometimes literally. Being a project that relied on high quality single crystals I could not have asked to work with a higher quality crystal grower than Prabhakaran at the University of Oxford.

Thank you to my tea break and office mates for providing snacks and excellent company and thank you to my parents whose phone calls were often a highlight of my week. My friends and colleagues Katie and Jimmy have my sincerest gratitude for all their support throughout our eight years at Holloway; its been a privilege to work alongside such caring and excellent people.

Contents

List of Figures

List of Tables

Chapter 1

Introduction

1.1 The pyrochlore structure

The compounds of the generalised formula $A_2B_2O_7$ form the crystallographic group referred to as pyrochlores. This system allows for a wide variety of chemical substitution on each site, with the only restriction being that of ionic radius and charge neutrality. Doping, stuffing and defects can be introduced to yield a wide range of possible compounds with a corresponding diversity in its physical and magnetic properties.

Due to the extensive compositional variety of pyrochlores, this family of compounds have a wide range of physical properties including but not limited to: superconductivity [1, 2, 3], semiconductivity [4, 5, 6], antiferromagnetism [7, 8, 9] and spin glass behaviour [4, 10, 11] depending on the precise stoichiometry. This diversity of behaviour lends itself the possibility for a wide range of applications, both potential and realised, including: photoelectrodes [6, 12], catalysts [13, 14], solid-state electrolytes [15, 16], thermal barrier coating [17, 18] and nuclear waste encapsulation [19, 20].

1.1.1 Crystallographic Structure

The pyrochlore system is described by the crystallographic space group $Fd\bar{3}m$ and contains eight formula units per unit cell i.e Z = 8. Oxide pyrochlores have four crystallographically distinct groups of atomic sites which can be expressed as $A_2B_2O_6O'$ where oxygen sits on two sites of different symmetry. The structure can be understood as two networks of coordination polyhedra. The A cations have a coordination of eight and sit within an approximately cubic scalenohedron of six O and two O′ anions, illustrated in Fig. 1.1. These A ions tend to be trivalent rare earth cations (e.g. Yb^{3+}, Dy^{3+}, Ho^{3+}) or metal cations (e.g. Y^{3+}, Pb^{3+}) [21]. The B cations have sixfold coordination and are positioned within trigonal antiprisms of oxygen ions. These are most commonly transition metals such as Ti^{3+} but can also take the form of basic metals like Sn^{3+} or semimetals such as Te^{3+} [22]. The fact that the system forms scalenohedra and trigonal antiprisms is on account of the impossibility of the conditions required for regular octahedra and cubic polyhedra to be fulfilled simultaneously [23].

There are 16 ions of each A and B type per unit cell and then 48 O and 8 O′ ions. It will be particularly important going forward to make a clear distinction between the two sets of positions, as which of these sites deviate from being perfectly symmetric will determine a great deal about the behaviour of the materials discussed here. The O′ ions which will subsequently be referred to as O(1) sites are contained within tetrahedra of A type ions while the O sites which will now be referred to as O(2) sites form trigonal antiprisms containing the B cations. These O(2) anions fill the interstitial sites between the A and B cations. The ionic positions are given in table 1.1.

It is mostly unimportant which of the four atomic symmetries contains the origin position but for consistencies sake the B cation will be used. The only free positional parameter, x is associated with the O(2) sites and can be determined by x-ray or neutron structure analysis. For an ideal pyrochlore lattice this value is $x = 0.3125$ although this

Ion	Location	Coordinates
		(0,0,0; 0,1/2,1/2; 1/2,0,1/2; 1/2,1/2,0) +
A	16d	1/2,1/2,1/2; 1/2,1/4,1/4; 1/4,1/2,1/4; 1/4,1/4,1/2
B	16c	0,0,0; 0,1/4,1/4; 1/4,0,1/4; 1/4,1/4,0
O(2)	48f	x,1/8,1/8; $\bar{x}$,7/8,7/8; 1/4-x,1/8,1/8; 3/4+x,7/8,7/8; 1/8,x,1/8; 7/8,$\bar{x}$,7/8; 1/8,1/4-x,1/8; 7/8,3/4,+x,7/8; 1/8,1/8,x; 7/8,7/8,$\bar{x}$; 1/8,1/8,1/4-x; 7/8,7/8,3/4+x
O(1)	8b	3/8,3/8,3/8; 5/8,5/8,5/8

Table 1.1: Pyrochlore structure data. The first line indicates that each of the values given could be added to each of those in the first line to give positions valid for the pyrochlore lattice.

value can vary between $0.3125 \leq x \leq 0.375$ [24]. In discussing the distinct polyhedra it is worth noting that they can be understood as a network of corner sharing polyhedra as shown in Fig. 1.2. Alternatively it can be thought of as a series of interpenetrating networks as shown in Fig. 1.1.

Considering the corner sharing polyhedra conception of the system, for the lower limit of x the A ion is coordinated in a distorted hexagon with a plane perpendicular to the O(1)-A-O(1) bond where the A-O(1) bond length is shorter than that of the A-O(2). The A-O(1)-A angle is independent of the positional parameter and always takes the value of 109°,28′. The B ions have perfect octahedral coordination for a system where x takes the lower limit value [23]. This can also be understood as the B cation being at the centre of a cube of O(2) anions with two diagonal O(2) anions absent. The B-O(2)-B bond length is in the range 120-140° depending on the value of x.

Considering the interpenetrating network conception of the system, the A tetrahedra can be written as $A_2O(1)$ and the B octahedra as $B_2O(2)_6$. The B octahedra consists

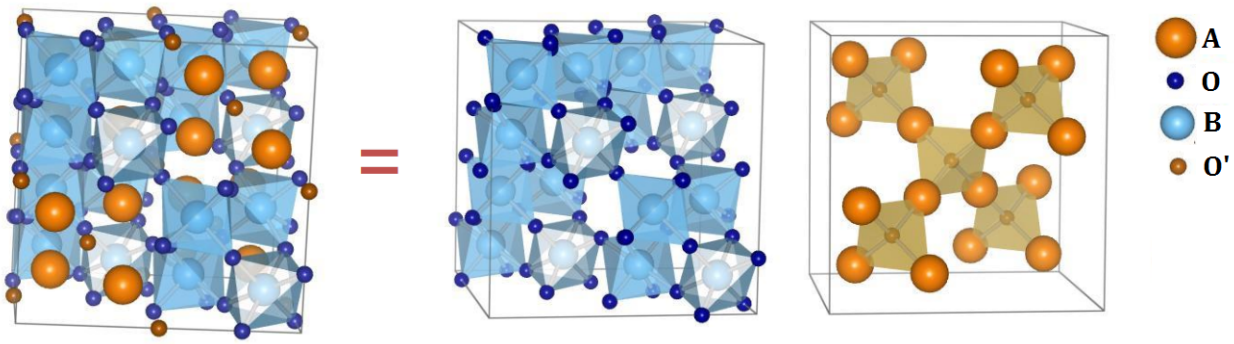

Figure 1.1: The pyrochlore lattice represented as a network of corner-sharing polyhedra. Figure reproduced from [25].

of O(2)-B-O(2) chains that form zig-zagging lines along the $\langle 110 \rangle$ directions [25]. The A cations are at the centre of a puckered hexagonal ring of six O(2) ions and normal to the plane of the hexagon is a pair of O(1) ions. The A-O(1) bond length is determined exclusively by the lattice parameter for a system with perfect stoichiometry on account of the lack of a positional parameter. These bonds form a series of interlinking chains intersecting on O(1) sites. As the A-O(1) bond length is shorter than that of the A-O(2) bond length the $A_2O(1)$ and $B_2O(2)_6$ units can be considered as mutually interpenetrating networks.

In the A network coordination of the anion are four A atoms that form a regular tetrahedron. In the $B_2O(2)_6$ network the B cation has a distorted octahedral coordination which at $x = 0.3125$ is perfectly octahedral with the distortion increasing with x. The point at which each network is closest to one another is between A sites and O(2) ions. However this distance is substantially larger than the bond lengths within each network [23].

When the value of the positional value reaches its highest value $x = 0.375$ the system assumes the fluorite structure which provides an alternative way of describing the system [26]. This typically assumes the form $A_2B_2O_8$ but for a highly distorted py-

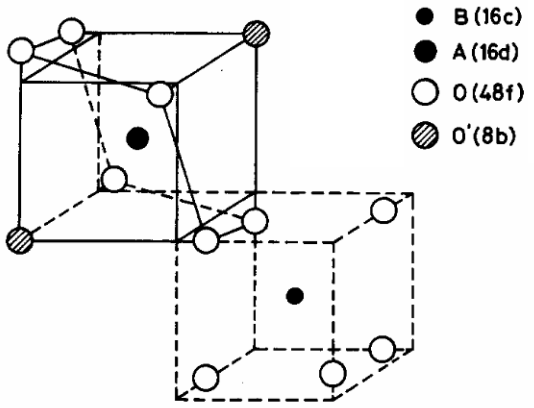

Figure 1.2: Distorted coordination polyhedra for $x = 0.3125$, i.e. an ideal pyrochlore lattice. Figure reproduced from [23].

rochlore the $A_2B_2O_7$ structure still applies but the lack of an eighth O atom is instead compensated for by shifted O(2) ions [27]. In this framework the cations are positioned in a face centred cubic array with the oxygen anions placed interstitially. The cations are ordered such that they lie in alternating rows along the [110] axis in half of the [001] direction and in alternating rows along $[\bar{1}10]$ in the other half of the (001) planes. In this description the O(2) sites have two nearest neighbours with both the A and B cations. In the fluorite formulation of the pyrochlore system (i.e. one with only seven rather than eight ions) there are four B cations that neighbour an oxygen vacancy and each of these is electromagnetically shielded from one another on account of the distortion provided by the high value of the positional parameter x [28]. The B cations form a distorted octahedron with a B-O(2)-B angle that at the fluorite limit takes the value of 132° [23].

The necessity of examining alternative ways of considering the pyrochlore structure arises on account of research linking the increase in disorder of the system to an increase in the positional parameter [29]. At its extreme this can result in a pyrochlore

transitioning into a defect fluorite system when sufficient disorder is introduced although the ionic radius ratio between the A and B sites also plays an important role where the presence of smaller B cations act to stabilise the pyrochlore structure [30].

1.2 Frustrated Magnetism

A system can be thought of as frustrated when the total energy of the system cannot be minimised uniquely by minimising the interaction of each pair of moments in the system [31]. The result of this is a system with a highly degenerate ground state where the degeneracy is of the order of the number of particles in the system [32]. This thesis will focus on the frustration of magnetic systems but frustration can arise in a number of scenarios including liquid crystals [33], colloidal crystals [34], Josephson arrays [35] and inside the dense nuclear matter at the edges of neutron stars [36]. Magnetic frustration has recently been utilised in work towards a new generation skyrmion based magnetic storage and data processing devices [37, 38, 39].

There are two types of frustration: random and geometrical. Random frustration can occur in systems with multiple length scales where the dynamic nature of a given system lends itself to being spatially inhomogeneous with competing interactions. A quenched form of random frustration occurs when the parameters concerned are independent with respect to time i.e. one where the dynamical processes are frozen out [32]. The most notable example of this being physically realised is in the spin glass system where the spins are arranged stochastically with competing antiferromagnetic and ferromagnetic interactions between them [40].

The other form of frustration is geometrical frustration where the ions sit on a regularly spaced lattice in competition with one another, and the local interactions are unable to be satisfied. This form of frustration is the type present in pyrochlores and is best understood by considering it in its simplest form.

1.2.1 The triangular lattice

Consider a single cell of a triangular lattice as in Fig. 1.3. Here we have Ising spins sitting on the vertices of the lattice, interacting antiferromagnetically. For the two labelled spins they are aligned antiparallel to each other which satisfies their need to reduce their mutual correlation. However if we add a third spin to the remaining vertex it is clear to see that this spin cannot be aligned antiferromagnetically with both of the existing spins, hence one third of the spins are frustrated.

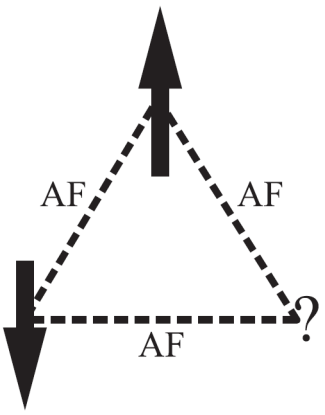

Figure 1.3: Elementary cell of the antiferromagnetic spin-1/2 Ising model on a two-dimensional triangular lattice. It is impossible to satisfy all three antiferromagnetic bonds simultaneously. Figure reproduced from [32].

From this initial description we can see that the Hamiltonian for this system would be given as follows:

$$H = -\mathcal{J} \sum_{i,j} S_i^z S_j^z \tag{1.1}$$

where $\mathcal{J}$ is the strength of the exchange interaction between the spins where a positive $\mathcal{J}$ corresponds to a ferromagnetic exchange and a negative $\mathcal{J}$ corresponds to antiferromagnetic exchange. S_i^z and S_j^z refer to Ising spins of value ± 1. For an antiferromagnet

the pair interaction is minimised when S_i^z and S_j^z take opposite signs. For a triangular system i.e. one with three spins such that i,j = 1,2,3 if we move from site one letting $S_1^z = +1$ and then satisfy the first pairwise interactions site two would be S_2^z = -1. Now S_3^z can either minimise its interaction energy with respect to S_1^z or with S_2^z so that S_3^z will take the value of either S_3^z = -1 or +1 respectively. One of the pairwise interactions will be impossible to be satisfied in this case. Going around the lattice and repeating the process starting with each atom assuming $S_i^z = \pm 1$ we find a sixfold degeneracy.

The kagome lattice is a network of corner sharing triangles that provides a conceptually useful and experimentally realised environment to discuss frustration. The nature of the spin Hamiltonian leads to the possibility of a range of spin interactions depending on the dimensional restriction of the spins. For a long time a physical realisation of the kagome lattice in magnetic solids was particularly scarce with the exception being $SrCr_{8-x}Ga_{4+x}O_{14}$ [41, 42] but there is now an abundance of materials exhibiting this lattice topology allowing for a range of environments ideally suited to investigating geometric magnetic frustration. The most simple form that frustration on the kagome lattice can assume is a one-dimensional restriction leading to Ising spins constrained to point along a single axis.

A recent example of an Ising constrained frustrated system on a kagome lattice is that of $Dy_3Mg_2Sb_3O_{14}$ which has a structure referred to as the tripod kagome lattice [43]. This system crystallises in a variant of the pyrochlore structure [44] where triangular layers of Dy^{3+} are substituted with non-magnetic Mg^{2+} resulting in a lattice where there are alternating layers of kagome planes of Dy^{3+} and triangular layers of Mg^{2+}. This arrangement leads to the kagome layers having spins with an Ising anisotropy directed in or out of the triangular units of the lattice, where the excess spin in a triangle gives it a net magnetic charge that creates an emergent magnetic charge ordering across the lattice as shown in Fig. 1.4 [45], where there are alternating magnetic charges

corresponding to whether a given triangle has an excess of spins pointing either in or out.

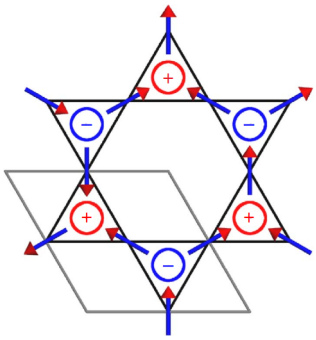

Figure 1.4: Emergent magnetic charge ordering in a triangular lattice with Ising anisotropy indicating this form of anisotropy in a two-dimensional planar system. Figure reproduced from [45].

This description can be extended to kagome systems with planar restricted spins, (i.e. XY triangular antiferromagnetism) by the XY Hamiltonian [46]:

$$H = -\mathcal{J}_{XY} \sum_{\mathbf{i,j}} \mathbf{S_i} \cdot \mathbf{S_j} = -\mathcal{J}_{XY} S^2 \sum_{i,j} \cos(\Delta\theta_{ij}) \tag{1.2}$$

where $\Delta\theta_{ij}$ describes the angle between the two spin vectors (which for the kagome lattice is constrained to 120°) and in this case the spin vectors S=$|\mathbf{S}_i|$=$|\mathbf{S}_j|$. This expression derives from the potential energy being approximated as its first-order component [46]:

$$E = -\mathcal{J} \cos(\Delta\theta_{ij}). \tag{1.3}$$

An example of the nature of the degeneracy afforded by the addition of a rotational degree of freedom is shown in Fig. 1.5.

For two-dimensional kagome antiferromagnets long-range order is impossible on account of the formation of magnetic vortices [48] and it is these excitations that provide

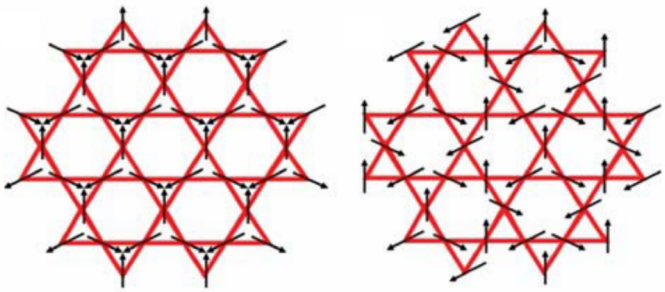

Figure 1.5: Kagome lattice with two spin orientations: Q = 0 (left) and Q = $\sqrt{3}$ x $\sqrt{3}$ (right) indicating an alternative form of ordering arising from the addition of a rotational degree of freedom. Figure reproduced from [47].

the possibility of utilising systems of this type for data storage on account of the topologically protected information inherent to them in the form of their winding number which may equal ± 1 [46, 49]. A novel variation on XY magnetism in kagome lattices is present in crystals of the candidate spin-liquid $Nd_3Ga_5Si_{14}$ [50]. $Nd_3Ga_5Si_{14}$ assumes a distorted corner sharing kagome lattice which is formed by a magnetic sublattice of Nd^{3+} cations illustrated in Fig. 1.6. A further example of alternative kagome geometries exhibiting planar anisotropies can be found in AgCN [46]. AgCN forms ferromagnetically ordered planes of Ag^+ cations but one where each subsequent layer of Ag^+ has its spins aligned with a 120° rotation to the one below it. The result of this is a kagome lattice where each corner of the triangle lattice is offset along the *c*-axis as shown in Fig. 1.7.

We can once again extend our description of spins on the kagome lattice to ones where the full Heisenberg symmetry is retained leading to three-dimensional spin ordering and an infinitely degenerate ground state [51]. One of the most studied manifestations of this is $ZnCu_3(OH)_6Cl_2$ referred to as Herbertsmithite a material which contains contains kagome layers of Cu^{2+} ions separated by Zn sites. [52, 53]. Herbertsmithite is

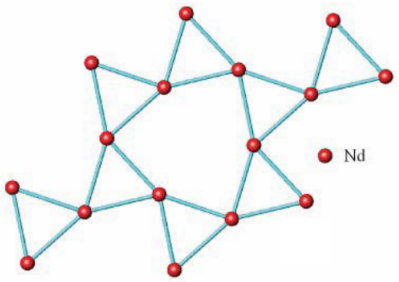

Figure 1.6: The distorted kagome lattice of Nd^{3+} ions in the *ab* plane of $Nd_3Ga_5Si_{14}$, a kagome lattice with an offset along the *c*-axis. Figure reproduced from [50].

notable as it is the first kagome system to be found to have no partial spin freezing at the lowest observed temperature making it a candidate quantum spin liquid [54, 55].

1.2.2 Three dimensional frustration in the pyrochlore lattice

It would seem evident that if we extend the kagome lattice to a three dimensional system, now specifically considering the A cation tetrahedra described previously, the system cannot be both frustrated and have primarily ferromagnetic correlations as the geometry of the lattice alone cannot cause frustration. However neutron scattering experiments by Harris et al. on samples of $Ho_2Ti_2O_7$ [56] showed that the spins sitting on the vertices of the tetrahedra display a strong anisotropy along the $\langle 111 \rangle$ directions so the spins are aligned to point either towards or away from the centre of the tetrahedra as indicated in Fig. 1.8. A spin pointing towards the centre of the tetrahedron wants its neighbours on the same tetrahedron to point outwards and vice versa. Hence, in this geometry half of the spins are frustrated. No long-range ordering was observed using neutron scattering down to T $\sim$ 50 mK and this confirms the frustrated nature of $Ho_2Ti_2O_7$ [56].

The magnetic sublattice of corner-sharing tetrahedra corresponds to the octahedral

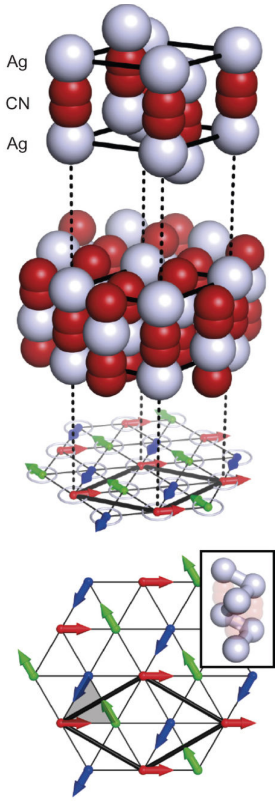

Figure 1.7: The crystal structure of AgCN. One dimensional metal-cyanide chains are arranged across a triangular lattice. The relative height of each plane can be discerned from the colour of the arrow representing its phase angle projected on to the lattice below. Fig. reproduced from [46].

sites of the spinels. In 1956 Anderson pointed out that the Ising model on this lattice is related to the zero-point entropy of ice [57]. It is, therefore, helpful to review the proton arrangement of water ice.

Crystalline water ice was the first frustrated system to be discovered that remains disordered at the lowest measured temperature [58, 59]. Pauling was then able to create a description of the system in terms of its lattice configuration and the arrangement of the protons [60] fulfilling the conditions of the previously postulated 'ice rules' [61].

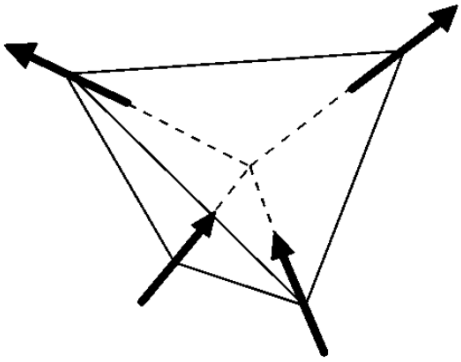

Figure 1.8: Ising anisotropy along the ⟨111⟩ direction of a tetrahedra. This is the type of spin anisotropy found in the spin ice system where the tetrahedra is made up of rare earth ions with an oxygen atom in the center. Figure reproduced from [56].

These state that for each oxygen anion there will be two protons positioned closest to the anion and two further away, illustrated in Fig. 1.9.

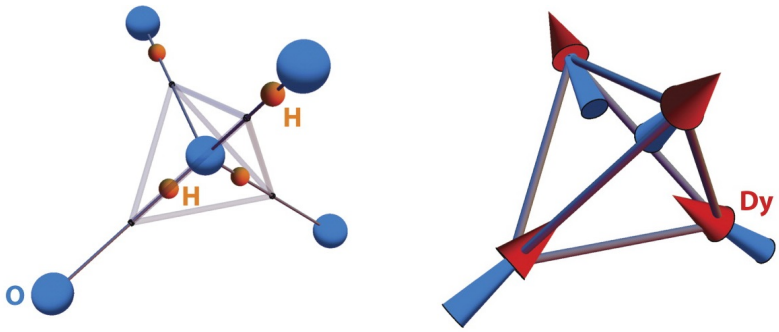

Figure 1.9: A tetrahedron of water ice (left) and a tetrahedron of Dy spins on a tetrahedron (right). The ice system fulfils the ice rules as two protons sit near the centre of the tetrahedron and two sit further away. The dysprosium titanate system also fulfils these conditions with its spin alignment rather than proton arrangement. Here two spins point into the tetrahedron and two point out. Figure reproduced from Ref. [62]

Each oxygen has two possible proton positions so for N oxygen ions there are 2^{2N} allowed proton configurations. Consider a single oxygen ion. It will have four surrounding hydrogen cations each with two possible positions giving a total of sixteen different configurations. Only six of these fulfil the ice rules so the total number of allowed states is:

$$\Omega = 2^{2N}\left(\frac{6}{16}\right)^{N} = \left(\frac{3}{2}\right)^{N}. \tag{1.4}$$

This leads to a highly degenerate ground state predicted by Pauling to have an entropy:

$$S \approx \mathrm{Rln}\frac{3}{2} = 3.35\ \mathrm{JMol^{-1}K^{-1}} \tag{1.5}$$

where R is the molar gas constant. This value was found to be approximately consistent with the experimentally acquired value [58] and the predicted proton arrangement has been observed via neutron diffraction experiments [63, 64]. Giauque et al. [59] calculated the entropy of ice by integrating the specific heat between helium temperature and the temperature of water's gaseous phase and then comparing this value to spectroscopic measurements of the energy level. This approach to calculating the entropy can be extended to the pyrochlore system.

The application of the ice rules to the frustrated magnetism on the pyrochlore lattice is illustrated in Fig. 1.9. For each tetrahedron two spins point in and two spins point out. Ramirez et al. [65] have provided a quantitative comparison with the entropy of ice by studying the heat capacity of $Dy_2Ti_2O_7$, see fig. 1.10. The plot of C(T)/T shows an ordering anomaly which falls rapidly to zero indicating the freezing of the moments in the sample. In the paramagnetic phase the entropy is Rln2 for a two state system. Integration of the heat capacity between T $\sim$ 300 mK to 10 K (the paramagnetic regime) yields the temperature dependence of the entropy, see Fig. 1.10. At high temperatures the entropy tends to S = R(ln2-(1/2)ln(3/2)) so that these pyrochlores have a highly

comparable entropy to water ice. Hence $Ho_2Ti_2O_7$ and $Dy_2Ti_2O_7$ are known as spin ice.

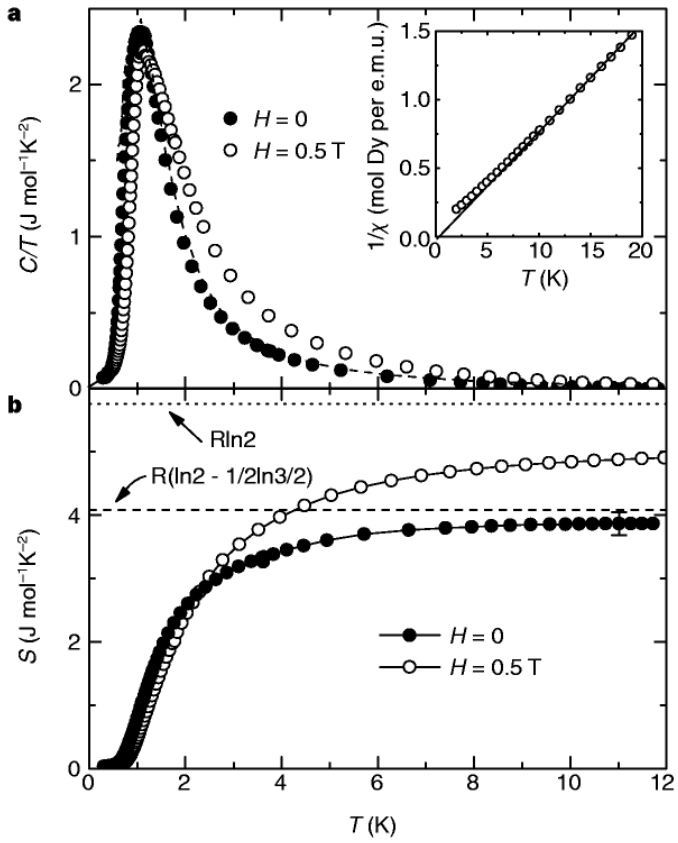

Figure 1.10: (a) Heat capacity divided by temperature of $Dy_2Ti_2O_7$. Dashed line is Monte Carlo simulation of a zero field measurement. (b) The entropy of $Dy_2Ti_2O_7$ from integrating C/T from 0.2 to 14 K. R(ln2-(1/2)ln(3/2)) is the value acquired for ice and Rln2 is the full spin entropy. Figure reproduced from Ref. [65].

One of the most exciting possibilities resulting from the frustration of the pyrochlore system is the potential for observing emergent magnetic monopoles. Dirac predicted the existence of quantised magnetic singularities connected by infinitely narrow solenoidal tubes carrying flux density in 1931 [66] and the pyrochlore lattice seems to promise

the potential for observing a lattice constrained version of this phenomenon. There have been experimental attempts at observing monopoles as cosmic particles [67] but these have been unsuccessful thus far [68]. Castelnovo et al. proposed the emergence of magnetic monopoles in the low-energy excitation of spin ice [69], see Fig. 1.11. The first stage in the argument is the replacement of spins at the vertices of the tetrahedra by magnetic charges on the diamond lattice, the so called dumbbell model. The ice rules result from the need to have magnetic charge compensation. An excited state is obtained by flipping one of the spins in a pair of corner-sharing rare-earth tetrahedra. This leads to a state where there is a three-in one-out spin configuration and the opposite configuration in the tetrahedron connected by the flipped spin. The excited state therefore has two adjacent sites on the diamond lattice with a net magnetic charge, effectively a monopole-antimonopole pair.

Two monopoles separated by a distance r will experience a Coulombic interaction of $-\mu_0 q^2/(4\pi \mathrm{r})$ where q is the net monopolar magnetic charge and μ_0 is the vacuum permeability. If N spins in a chain are flipped the energy cost of breaking bonds is the same as flipping one spin. Only a finite energy is required to separate the monopoles to an infinite distance and, therefore, they are deconfined. These fractionalised excitations are lattice constrained magnetic monopoles [69]. This system of deconfined monopoles is the first in which we can access and manipulate free magnetic charges, as shown in Fig. 1.12.

The spin correlations in the Coulomb phase have been studied using diffuse neutron scattering. Polarised neutron scattering studies of the $Ho_2Ti_2O_7$ reveal the existence of pinch points, see Fig. 1.13 [70]. These features arise from the ice rules and they are reproduced in a model of spin ice with nearest neighbour exchange. High resolution measurements have determined a temperature dependence on the width of the pinch points, and this has been related to the separation between monopoles.

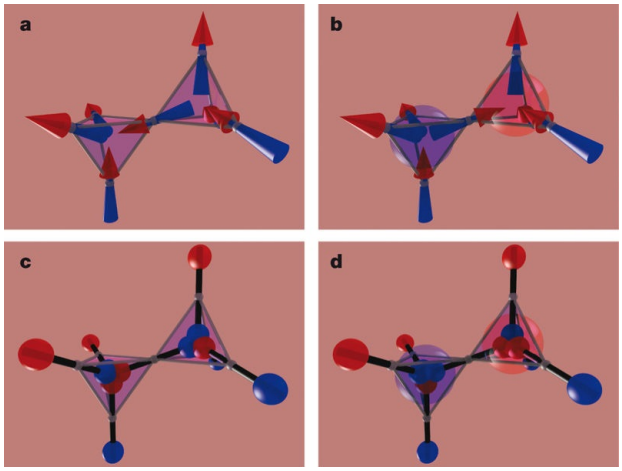

Figure 1.11: (a) A pair of charge neutral tetrahedra which transitions to (b) when a spin is inverted along the $\langle 111 \rangle$ and the tetrahedra become magnetically charged. (c) and (d) show the same systems but with the dumbbell model so that these spins are considered as sets of opposite polarity magnetic charges. Figure reproduced from Ref. [69].

Work by Morris et al. [71] allowed for the experimental observation of emergent magnetic monopoles in a sample of single crystal $Dy_2Ti_2O_7$. It was observed that in a spin ice system with no applied field the system will assume a dense network of interconnecting strings that comprise random walks across the sample, meaning that there is no way of tracing the paths of the monopoles. Morris et al. devised an elegant solution to this problem by applying an external magnetic field along the $\langle 100 \rangle$ direction of the sample. For a relatively high field the ground state will be non-degenerate and free of monopoles as all the spins are arranged as a splayed ferromagnet with spins pointing with a component along the axis of magnetisation constrained only by the need to lie along a $\langle 111 \rangle$ Ising axis. By lowering the field a sparse density of flipped spins will be allowed in the sample terminating at the edges of the sample as demonstrated in Fig. 1.14.

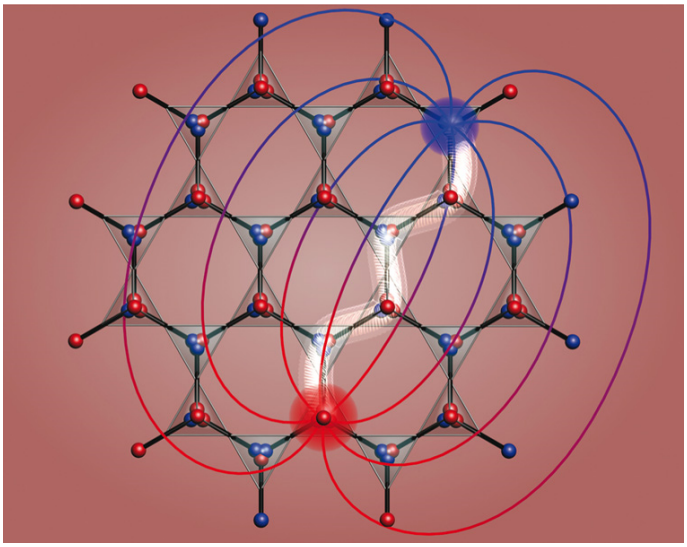

Figure 1.12: A pair of monopoles separated by a Dirac string of inverted dipoles between them. Figure reproduced from Ref. [69].

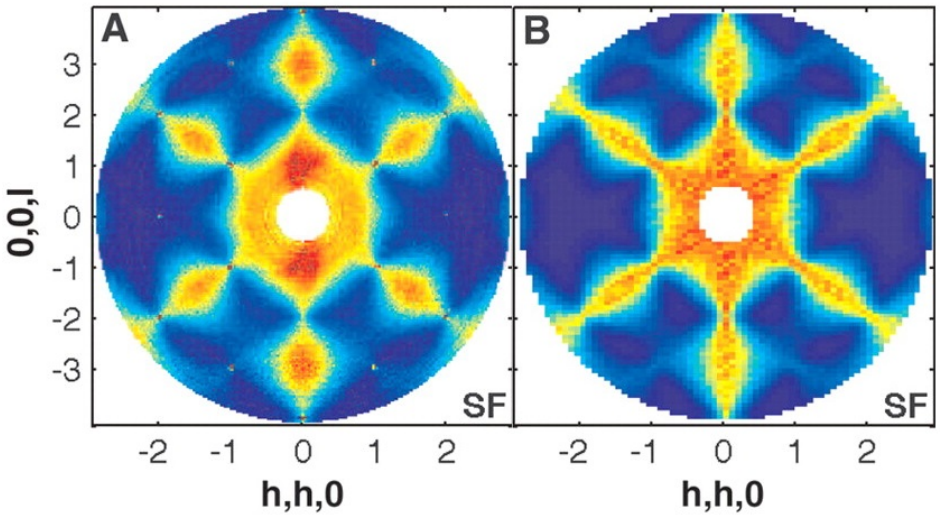

Figure 1.13: Polarised diffuse scattering of $Ho_2Ti_2O_7$ taken on D7 at the ILL. (A) is the experimentally acquired data with (B) the result of Monte Carlo calculations on the same system. Figure reproduced from Ref. [70].

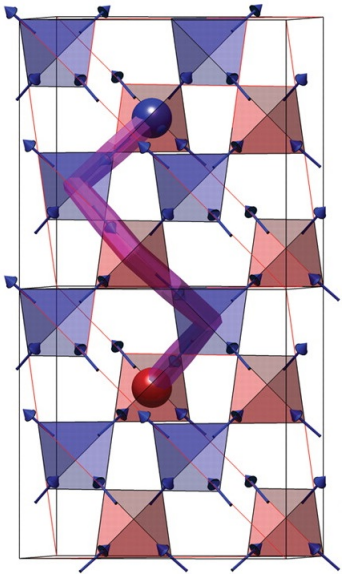

Figure 1.14: Figure showing a network of corner sharing tetrahedra with an axis of magnetisation applied from bottom to top. The Ising spins are constrained to point along the direction of magnetisation while in an excited state depicted here a monopole is allowed to form with a Dirac string connecting them. Figure reproduced from ref. [71].

By measuring near the field value that allows for the spontaneous formation of Dirac strings the experimental signature of the system can be observed via neutron scattering. Figure 1.15 shows the diffuse neutron scattering from $Dy_2Ti_2O_7$ for a field along $[00l]$. The cones of scattering energy around the (020) position are reproduced in a simulation with weakly biased random walks.

Another compelling avenue of investigation afforded by frustrated pyrochlores is that of quantum order by disorder. Order by disorder is a mechanism whereby the continuous degeneracy of frustrated systems can be broken by accessing low energy fluctuations available to the ground states [72]. The available states are those with high densities of low energy modes so that they are selected on account of entropy rather than simply

having favourable energetics [73]. Quantum order by disorder occurs when quantum mechanically driven low energy spin fluctuations allow this phenomena. Quantum order by disorder has been observed previously in a Heisenberg antiferromagnet [74] so the highly frustrated antiferromagnets within the pyrochlore family provide promising territory in which to observe order by disorder.

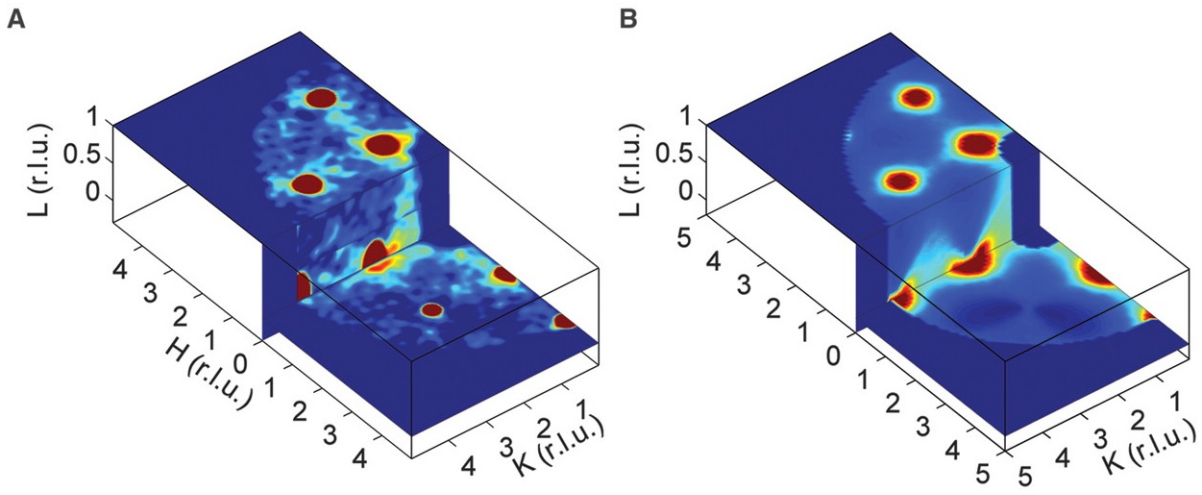

Figure 1.15: (A) Neutron diffraction data taken at 0.7 K and with a field applied along the [00l] direction of $Dy_2Ti_2O_7$ on the flat-cone diffractometer E2 at the Helmholtz-Zentrum Berlin light source. A cone of scattering is observed coming out of the (020) Bragg peak. (B) Caluclation of the diffuse scattering with weakly biased random-walk correlations. Figure reproduced from ref. [71].

Quantum order by disorder has been observed in the frustrated XY pyrochlore $Er_2Ti_2O_7$ [73, 75, 76, 77]. $Tb_2Ti_2O_7$ also has notable unusual low temperature properties. $Tb_2Ti_2O_7$ has been classified as a quantum spin liquid [78, 79]. This is in contrast to a spin ice state in that as the temperature of a sample is cooled one would expect it to be able to explore its degenerate ground states until eventually the spins are frozen into a given configuration [80]. However Anderson proposed a type of interaction whereby

the amplitude for spins to tunnel between degenerate states is sufficiently high that as the temperature tends towards zero the spins in the system are still able to fluctuate [57]. The antiferromagnetic interaction between the A sites in a quantum spin liquid can be considered as valence bond pairs where each pair is a maximally entangled spin-0 singlet state and all the A sites are able to form valence bond pairs. What characterises a quantum spin liquid is that these pairs are not only entangled with those on the neighbouring tetrahedra but also exist in a ground state that is the superposition of all the different combinations of valence bond pairs [81]. Neutron scattering, muon spin resonance and d.c susceptibility studies have found that $Tb_2Ti_2O_7$ retains its paramagnetism down to the lowest measured temperature, a compelling signature of the spin liquid state [82, 83, 84, 85], which is particularly relevant as $Yb_2Ti_2O_7$ has been classed as a potential quantum spin liquid [86].

1.3 Review of defects in pyrochlores

1.3.1 Motivation

Geometric frustration is expected to lead to the absence of long-range order down to very low temperatures where quantum fluctuations are important. This is very attractive from the perspective of an experimental physicist since such systems may be used to test theoretical ideas in model magnetic systems. For example, $Yb_2Ti_2O_7$ has been proposed as a candidate quantum spin liquid [86].

However, geometrical frustration relies on a delicate balance, and other factors intervene to lift the degeneracy and significantly change the physics of the system. The magnetic exchange interactions beyond nearest neighbours can have a significant effect. In the case of the classical spin ice materials $Ho_2Ti_2O_7$ and $Dy_2Ti_2O_7$ the large magnetic moments make magnetic diplolar interactions significant and long-range order has

been predicted down to very low temperatures [87, 88, 89]. The long-range order is not observed experimentally since these systems fall out of equilibrium below $T \sim 600$ mK. Hence the spin ice state is observed down to the lowest temperatures.

The presence of structural disorder is another factor that can potentially lift the degeneracy and affect the physics. In the case of the classical spin ices, the two-in two-out magnetic ground state is robust, and has been observed for all nominally stoichiometric samples. However, in this case, structural defects have an important affect on the physics at low temperature [90], and this was shown to be due to magnetic residual resistance from isolated oxygen vacancies [91]. In the case of $Yb_2Ti_2O_7$ the influence of structural defects appears even more important, since the magnetic ground state is strongly sample dependent [92].

1.3.2 Oxygen deficiency

There are two sites from which oxygen ions can be removed in the pyrochlore system, the 8b sites (O(1)) and the 48f (O(2)).

1.3.2.1 O(1) deficiency

The 8b oxygen site is in a centre of a tetrahedron of A cations so removing one of these anions will expose the A cations across the tetrahedra to one another. This will have the effect of destabilising the structure as the cations interact directly with one another [23]. Nethertheless, powder x-ray diffraction studies show that for $Pb_2Ru_2O_{7-\delta}$, $Pb_2Ir_2O_{7-\delta}$ and $Pb_2Re_2O_6$ the oxygen vacancies are located exclusively on the O(1) sites [28]. Of the pyrochlore systems it is frequently the case that the A cation has a polarisable $6s^2$ pair of electrons which have energy levels comparable to that of the virtual energy levels of the vacancy [28]. The virtual levels represent an effective potential well which cause the valence orbitals of the A cation to spread out into the anion vacancy site where

they overlap with the neighbouring A cation orbitals which allows for the formation of band states. The results in the creating of A-A bonding orbitals in place of the existing non-bonding $6s^2$ level. The electrons in these bonding orbitals have a concentrated charge density on the vacancy site which results in the stabilisation of the valence cation electrons and the formation of the defect pyrochlore structure [28].

1.3.2.2 O(2) deficiency

The second possible site upon which oxygen vacancies can be formed is on the 48f O(2) site. In the case of a powder sample of $Yb_2Ti_2O_7$ reacted with CaH_2, it was found from refinement of neutron data that isolated oxygen vacancies form on the O(2) sites [93]. This also introduced a Yb-Ti anti-site disorder of 3.3%, not present in the starting material. Also by reacting with CaH_2 a powder sample of $Y_2Ti_2O_7$ was found to have isolated vacancies forming on the O(2) sites with a small amount of anti-site disorder. It is postulated that oxygen deficient pyrochlores with lone pair cations have their vacancies forming on the O(1) site as in the case of $Pb_2Ru_2O_{6.5}$ [94] whereas O(2) vacancies will form in response to reduction on the B site centres which have a much shorter B-O(2) bond length than B-O(1) [93].

It is by no means obvious for stoichiometrically prepared samples of $Yb_2Ti_2O_7$ which form of oxygen deficiency will be dominant so it is worth considering yet a further form of disorder.

1.3.3 Stuffing

A possible mechanism for introducing a controlled number of defects into a system is stuffing. Stuffing is the process by which a crystal is grown with an excess of A cations and these substitute ions on the B sublattice. This results in a reduction in the number of oxygen anions by charge compensation. In a pyrochlore system this has the general

formula $A_{2+x}B_{2-x}O_{7-x/2}$ as for every two additional A^{3+} cations that are added there are two B^{4+} cations removed and an O^{2-} anion needs to be removed to retain neutrality. As x tends towards $x = 0.67$ the A and B sites become effectively indistinguishable from one another and the system transitions to the fluorite structure with an enlarged lattice parameter [95]. Stuffing can modulate other properties of the crystals in which it is present. Experiments on a stuffed sample of $Ho_2Ti_2O_7$ found a variation in the heat capacity and magnetisation [95], and measurements on $Pr_2Zr_2O_7$ and $Tb_2Ti_2O_7$ found stuffing modulates the low temperature specific heat of the system [96, 97, 98, 99].

Ross et al. [100] grew nominally stoichiometric samples of $Yb_2Ti_2O_7$; one of which was a powder and the other a single crystal crushed into a powder. Both samples were then studied using powder neutron diffraction. The resulting structural refinement found an extremely small preference for the stuffed model at a level of 2.3% over the stoichiometric one for the sample grown using the floating zone technique. For this sample it was also observed that the lattice parameter increased in a way consistent with previous measurements of stuffed samples [95, 100]. However when measuring a powder sample the stoichiometric model was the best fit. A study by Mostaed et al. measuring floating zone grown crystals by scanning transmission electron microscopy, each with different heat capacity behaviour, found that a sample with no heat capacity anomaly exhibited stuffing [101].

1.3.4 Diffuse scattering study of $Y_2Ti_2O_7$

A study of particular interest to this thesis is Sala et al. [91] as a number of the techniques used therein will be employed. In this study, three single crystal samples of $Y_2Ti_2O_7$ were grown using the floating zone method described in section 2.8.3 and measured using diffuse neutron scattering. One sample was left as-grown, another was annealed in hydrogen with the intention of creating isolated oxygen vacancies and

another was annealed in oxygen with the intention of removing any isolated oxygen vacancies. Diffuse neutron scattering results for the as-grown and the annealed samples are shown in Fig. 1.16. The as-grown sample showed a substantial amount of diffuse scattering whilst the oxygen annealed sample showed almost none. The implication of this result is that the process of annealing in oxygen removes defects from the system and the fact that this works means that these defects must be isolated oxygen vacancies rather than those arising from stuffing. Stuffing is the process where defects are introduced by growing a sample with an excess of A or B atoms and is explained is more detail in section 3.3.2.

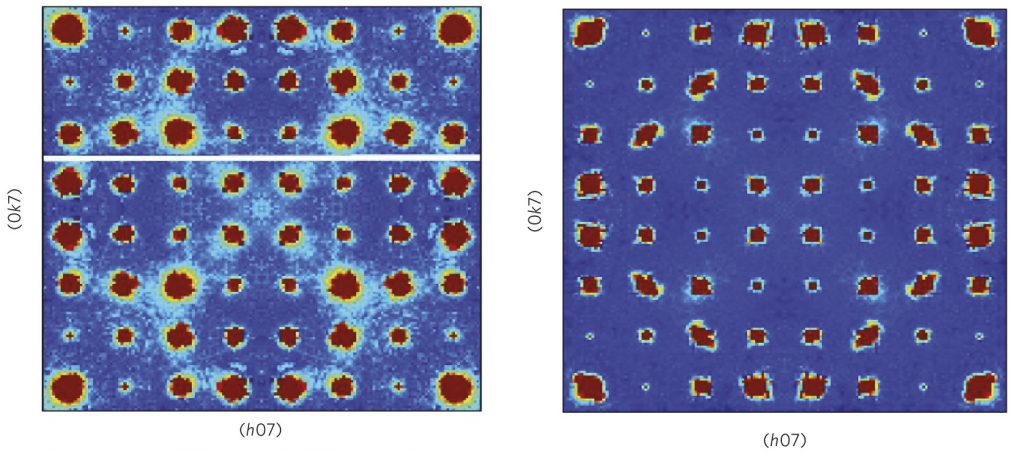

(a) (b)

Figure 1.16: Diffuse neutron scattering results in the $(hk7)$ plane taken on SXD for single crystal samples of (a) as-grown and (b) oxygen annealed $Y_2Ti_2O_7$. The oxygen annealed sample is free of any diffuse scattering suggesting that the defects in the as-grown sample are isolated oxygen vacancies. Reproduced from Ref. [91].

The nature of these isolated vacancies was determined to be on the O(1) sites. This was achieved firstly by structural refinements on single crystal x-ray measurements. The results of which can be seen in table 1.2 and show equal concentrations on the Y

	Depleted	As-Grown	Annealed
Colour	Black	Yellow	Transparent
Space Group	$Fd\bar{3}m$	$Fd\bar{3}m$	$Fd\bar{3}m$
Lattice Parameter	10.1223(3) Å	10.111(3) Å	10.102(2) Å
Y	0.992(9)	1.016(5)	1.01(1)
Ti	1	1	1
O(1)	0.88(2)	1.01(2)	0.97(3)
O(2)	0.96(2)	1.06(1)	1.10(2)
R_w	9.38	6.58	11.71

Table 1.2: Refinement of the average structure of $Y_2Ti_2O_7$ performed on x-ray diffraction data acquired at 300 K. Reproduced from Ref. [91].

and Ti sites to within 2% so that stuffing of Ti on the Y sites is minimal.

Definitive evidence for the vacancies being on the O(1) sites comes from the modelling of the diffuse scattering with a Monte-Carlo balls and springs model. A comparison to the neutron diffraction data with a model with O(1) vacancies almost perfectly reproduced the diffuse scattering as can be seen in Fig. 1.17. The mechanism for recreating this scattering is the movement of Y away from the O(1) vacancy sites and corresponding movement of the O(1) ion in the neighbouring tetrahedron. For charge compensation, for every missing oxygen ion two Ti^{4+} ions are changed to Ti^{3+}, and this is also required to better reproduce the scattering.

This work is discussed in such detail here as a similar approach will be exploited when presenting arguments on the structure of $Yb_2Ti_2O_7$.

There are so many conflicting results for the nature of the defect structure of $Yb_2Ti_2O_7$ it is in no way obvious what to expect for it. On top of the possibilities discussed above it has also been postulated that the defect structure arises on account

of Yb ions swapping with Ti at the 2% level [102] and also that there are Yb vacancies [103]. In order to investigate the properties of $Yb_2Ti_2O_7$ it is necessary to understand its defect structure and also to have a reliable means of determining if a given sample is stoichiometric.

1.4 Review of the magnetic properties of $Yb_2Ti_2O_7$

The geometric frustration experienced by the pyrochlore systems tends to lead to the suppression of long-range magnetic order meaning that even at low temperatures short-range magnetic correlations can typically be expected [104]. The spin ices $Dy_2Ti_2O_7$ and $Ho_2Ti_2O_7$ [105, 106, 107] along with the spin liquid $Tb_2Ti_2O_7$ [82, 84] all exhibit disordered ground states measured at temperatures as low as 30 mK. In the case of $Er_2Ti_2O_7$ order by disorder lifts the degeneracy resulting in unconventional magnetic

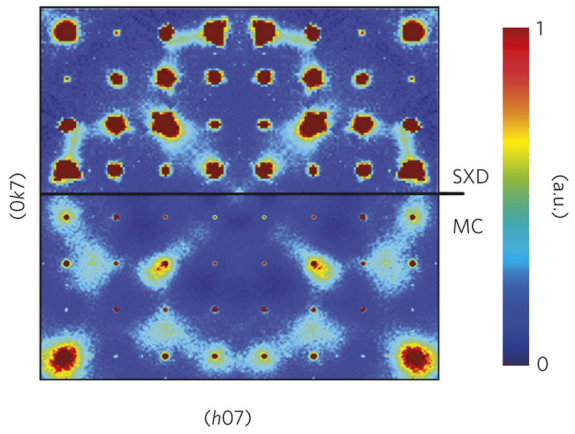

Figure 1.17: As-grown $Y_2Ti_2O_7$ in the $(hk7)$ plane for (a) neutron diffuse scattering on SXD and (b) a Monte Carlo ball's and spring model. The diffuse scattering of the experimental data is almost perfectly reproduced by a model with O(1) vacancies suggesting that this is in fact the dominant mode of disorder in the system. Reproduced from Ref. [91].

order at low temperatures [75].

In $Yb_2Ti_2O_7$, however, the situation is more complicated as it has in some cases been characterised as a quantum spin ice [108, 109, 110, 111, 112, 113, 114, 115], whereas other studies give a ferromagnetic ground state with unsual quantum fluctuations [103].

The earliest relevant investigation of the magnetic properties of $Yb_2Ti_2O_7$ were carried out by Bløte et al. in 1969 [111]. Specific heat measurements were taken on a powdered sample of $Yb_2Ti_2O_7$ which revealed an ordering anomaly at $T = 214$ mK suggesting a first-order phase transition. The same publication also provides a determination of the Curie-Weiss temperature obtained from bulk susceptibility measurements, found to be $\theta_{cw} = 0.4 \pm 0.1$ K. A positive Curie-Weiss temperature is indicative of ferromagnetism being the dominant magnetic interaction in the material.

Subsequent determinations of the Curie-Weiss temperature have also found it to be positive. Bramwell et al. obtained values in the range 0.49-0.7 K depending on the corrections used [105] and Hodges et al. obtained a value of 0.75 K [112]. The discrepancies in the reported values have been attributed to the non-linearity of the inverse susceptibility with temperature which would result in there being a dependence in the Curie-Weiss temperature on the range of measured temperatures [116, 117]. Figure 1.18 shows a summary of heat capacity measurements from various powders and single crystals of $Yb_2Ti_2O_7$.

A study by Arpino et al. [92] obtained Curie-Weiss temperatures in the range $\theta_{CW} \approx$ 0.4-0.8 K for samples of $Yb_{2+x}Ti_{2-x}O_{7-x/2}$ where θ_{CW} decreases with a decreasing value of x with the results shown in Fig. 1.19. Regardless of the specific value of θ_{CW} a small positive value has been found to be reproducible across a number of experiments [92, 100, 103, 104, 105, 114, 117, 119].

In contrast to the spin ice materials $Yb_2Ti_2O_7$ combines ferromagnetic exchange with planar XY anisotropy perpendicular to the $\langle 111 \rangle$ direction [113, 117, 120]. Hodges

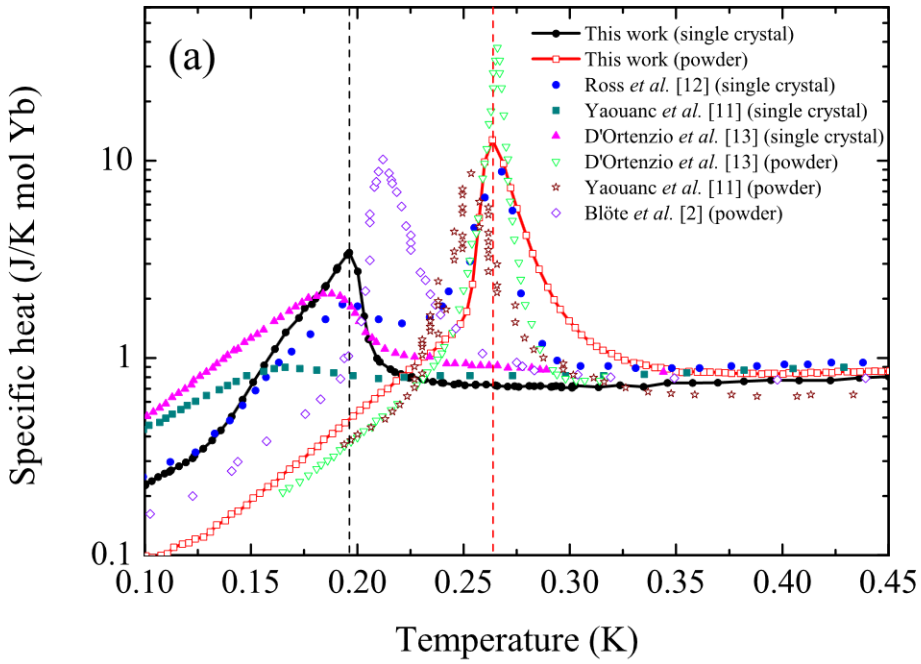

Figure 1.18: Specific heat versus temperature for a range of studies on samples of $Yb_2Ti_2O_7$. There are considerable inconsistencies in the measured values of the specific heat anomaly. Figure reproduced from Ref. [118].

et al. made a determination of the g-tensor finding that $g_{||} = 1.79$ whereas $g_{\perp} = 4.27$ [112]. Cao et al. also found a larger value for $g_{\perp}$ with $g_{||} = 2.25$ and $g_{\perp} = 4.1$ obtained via polarised neutron analysis on a powdered sample [117]. Malkin et al. obtain comparable values to Hodges et al. using optical spectroscopy with $g_{||} = 1.836$ and $g_{\perp} = 4.282$ [120]. The XY anisotropy is further supported by Bramwell et al. [116] who find a temperature dependent magnetic moment which reduces from 4 μ_B at room temperature to 3.3 μ_B at 0.3 K which is smaller than the expected moment of 4.54 μ_B for an L = 3, S = 1/2 ion. This reduction would indicate anisotropy of the moments.

The spin ice system combines ferromagnetic exchange with Ising anisotropy with moments constrained along the (111) axis which is an important factor in it being a

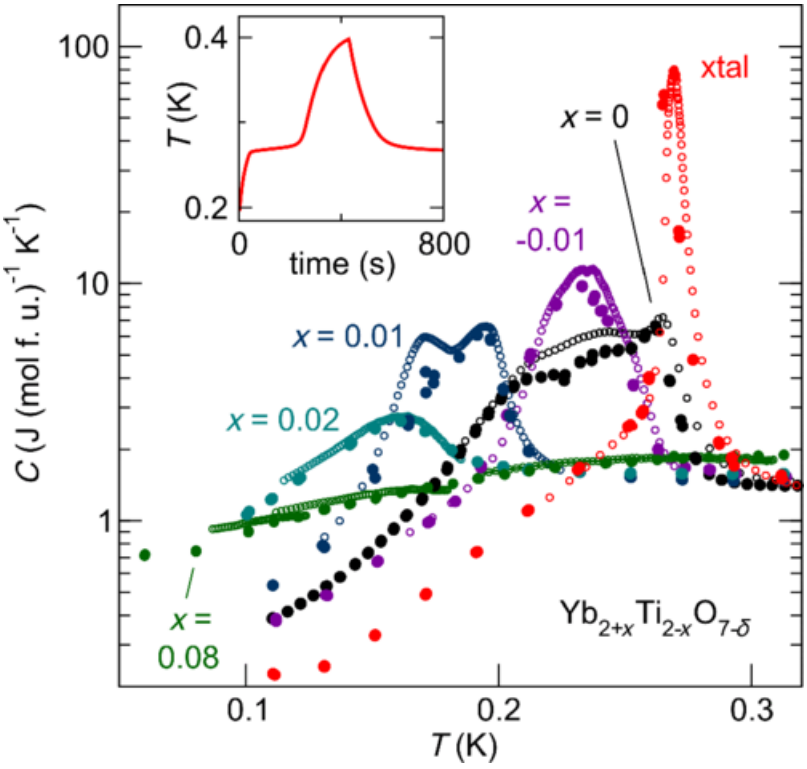

Figure 1.19: Heat capacity for $Yb_{2+x}Ti_{2-x}O_{7-\delta}$ for different values of x. The peak in the specific heat broadens and decreases as x deviates from $x = 0$. Figure reproduced from Ref. [92].

frustrated magnetic system. By having XY anisotropy one might then assume that $Yb_2Ti_2O_7$ would have an unfrustrated ground state. This notion would be further reinforced by the reported ordering anomaly in the specific heat [104, 111, 113, 121, 122, 123, 124]. Yaouanc et al. find this feature to be absent for single crystal samples [121] although this has subsequently been observed [104, 118, 123, 124, 125, 126]. Instead it appears to be the case that powder samples exhibit a peak with a reduced intensity by approximately an order of magnitude [104, 118, 125].

There has been experimental work which supports the notion of ordered long-range ferromagnetic ordering at low temperatures. Yasui et al. [114] find a lack of neutron

scattering intensity away from the Bragg peaks in a single crystal sample of $Yb_2Ti_2O_7$ which is interpreted as indicating a simple ferromagnetic ordering. More recently a polarised neutron scattering experiment on the same sample carried out by Chang et al. demonstrated the presence of ferromagnetic ordering [103]. They were also able to reproduce the diffuse magnetic scattering in the Coulomb liquid phase above T_c, see Fig. 1.20. Further magnetisation measurements [127] also find a ferromagnetic ground state and this conclusion is further supported by mean field calculations [109, 128].

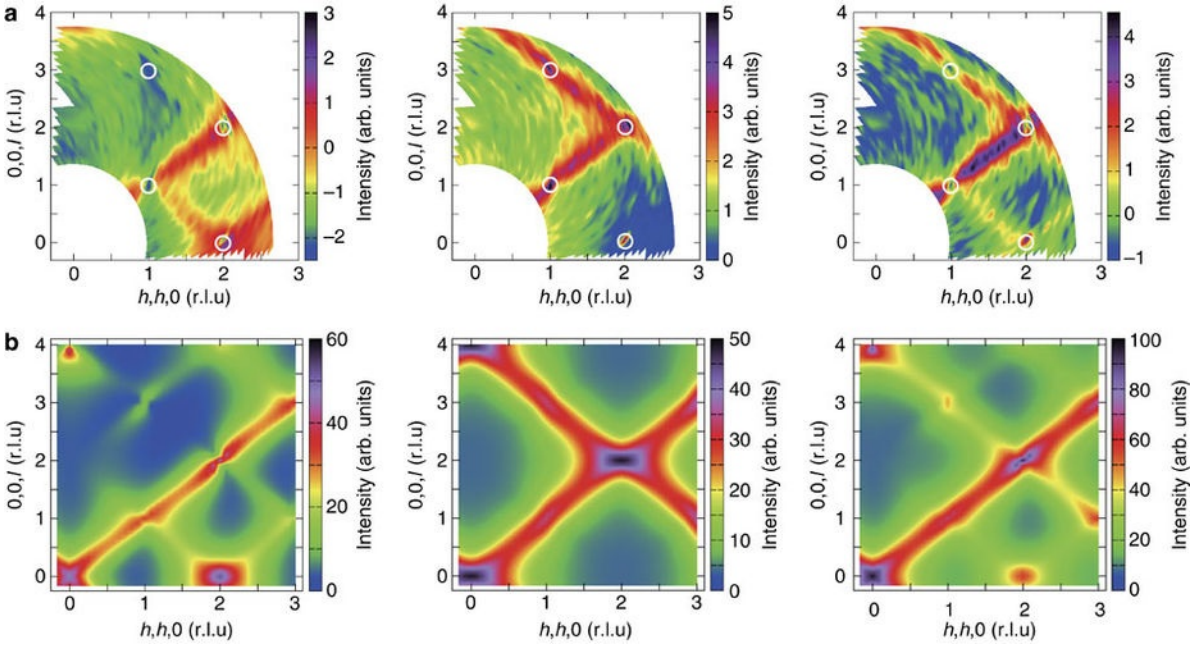

Figure 1.20: (a) Experimentally observed profiles for the spin-flip (left) non spin-flip (middle) and total spin flip (right) scattering for polarised neutron scattering in the (hhl) plane, along with corresponding calculations (b) at $T = 30$ mK. Figure reproduced from Ref. [103].

The Hamiltonian for $Yb_2Ti_2O_7$ has been described by a pseudospin-1/2 quantum spin ice model [110, 129, 130] which has led to a result consistent with a description of the ground state as being that of a splayed ferromagnet [131] which is the state that

has been reported experimentally for $Yb_2Sn_2O_7$ [132].

This result is by no means uncontroversial with alternative magnetic $Yb_2Ti_2O_7$ ground states being proposed. A number of experiments have found evidence of short-range correlations across a comparable temperature range as reported by polarised neutron scattering [104, 108, 133], muon spin resonance [113, 125, 126, 134] and magnetisation measurements [112, 114] which are in direct contradiction to the notion of long-range ferromagnetic ordering.

Of the neutron scattering experiments that observe a dynamic magnetic ground state, above the transition temperature rods of diffuse scattering are reported along the $\langle 111 \rangle$ directions which are interpreted as indicating two-dimensional correlations [104, 108, 135]. Ross et al. [104, 108] observe that below 400 mK the diffuse scattering features are suppressed with an increasing intensity around the (111) nuclear Bragg peak which is interpreted as a transition to short-range three dimensional correlations. A further measurement by Ross et al. [110] is able to reproduce the high field inelastic neutron scattering pattern for $Yb_2Ti_2O_7$ using exchange parameters for a quantum spin liquid as shown in Fig. 1.21.

Robert et al. [119] postulate that the $Yb_2Ti_2O_7$ ground state exists on the edge of a phase boundary between antiferromagnetism and ferromagnetism suggesting that it is governed by strong quantum fluctuations arising from the competition between those phases. This manifested itself in a model with a dynamical response in the excitation spectra that well reproduces the work by Ross et al. [110] and also the work by Chang et al. [103] for the polarised neutron scattering obtained at $T > T_c$. The comparison between model and data are shown in Fig. 1.22.

An investigation of the magnetic excitations by Thompson et al. [136] on the instrument LET found that for a high field that the magnetic excitation spectrum for a single crystal of $Yb_2Ti_2O_7$ at high field can be well reproduced with exchange parameters for

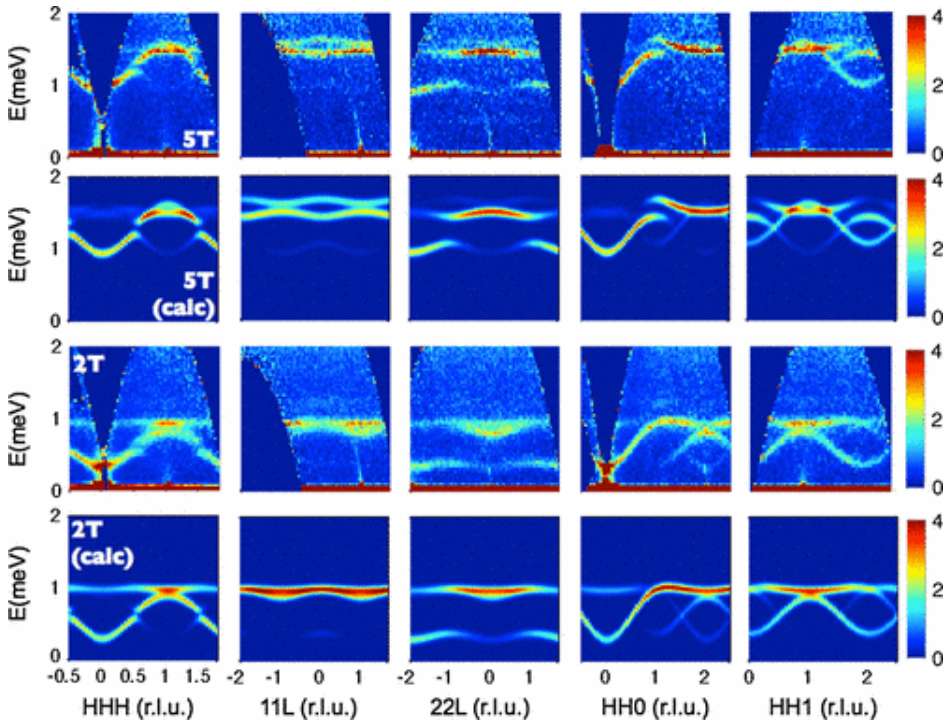

Figure 1.21: Measured S($\mathbf{Q}$,ω) at T = 30 mK with the calculated scattering showing good agreement with the experimental data using exchange parameters corresponding to a quantum spin liquid state. Figure reproduced from Ref. [110].

a system dominated by quantum fluctuation effects. The scattering and corresponding simulation are shown in Fig. 1.23.

A recent study has considered the application of pressure to the system [137]. Neutron diffraction and muon spin resonance measurements show the ground state of the system changing from a disordered ground state to a splayed ferromagnet on application of 112 kPa of pressure. This experiment notes a dependence of the ground state on the sample stoichiometry with a lightly stuffed sample shifting the transition temperature. The authors argue that the application of pressure is similar to the chemical pressure arising from stuffing and that light stuffing is responsible for the observation of ferromagnetic ground states. The corresponding phase diagram is shown in Fig. 1.24. An

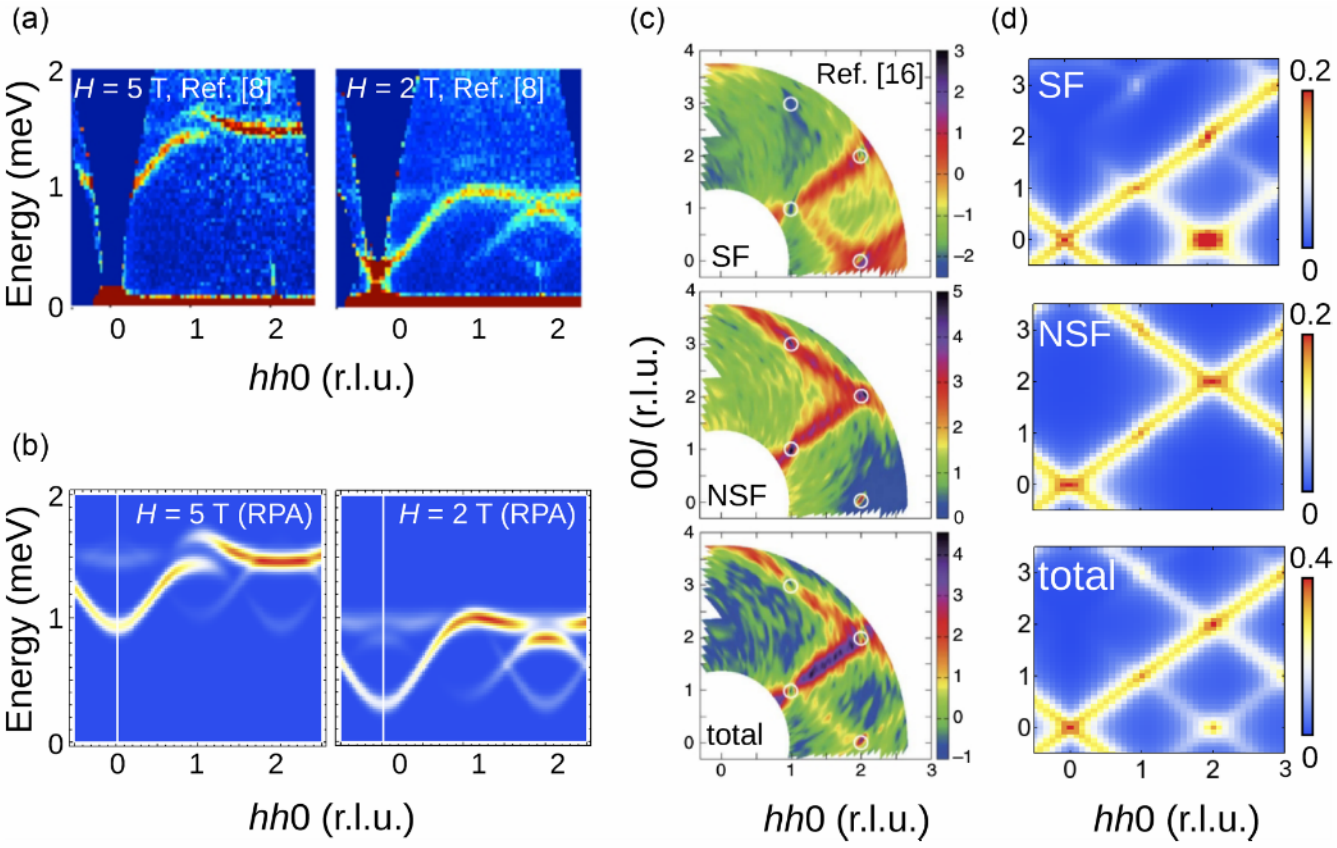

Figure 1.22: Comparison between the measured [110] (a) and calculated (b) spin wave spectra at high field along the [hh0] direction. Also, the comparison between measured [103] (c) and calculated polarised diffuse scattering in the (hhl) plane. Figure reproduced from Ref. [119].

alternative phase diagram in terms of applied field is presented in Fig. [138] that shows a ferromagnetic ground state.

Because of the many contradictory results found in the literature it is natural to consider the possibility that these discrepancies arise on account of the ground state being sensitive to minor variations in the sample composition as is the case with the rare earth pyrochlores $Y_2Ti_2O_7$, $Ho_2Ti_2O_7$, $Tb_2Ti_2O_7$ and $Pr_2Zr_2O_7$ [91, 95, 96, 97, 98].

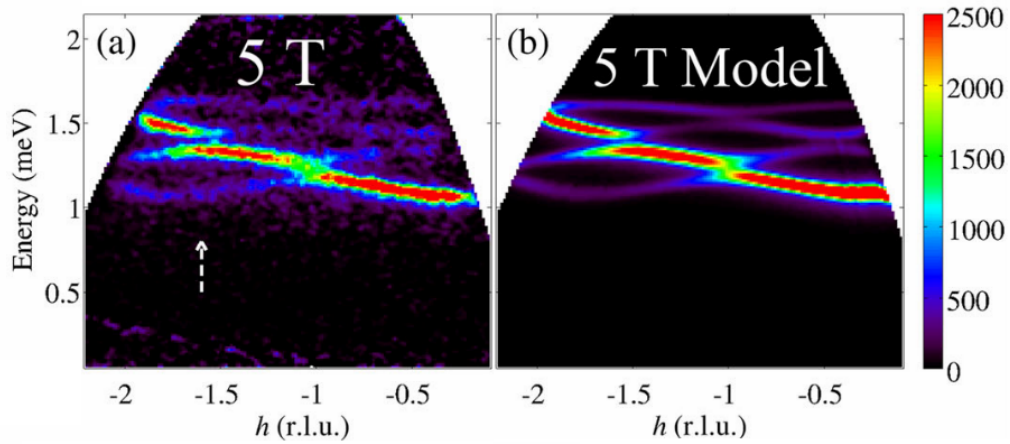

Figure 1.23: For a single crystal of $Yb_2Ti_2O_7$ the sharp magnon modes present at field of 5 T (a), are present in a model with exchange parameters corresponding to strong quantum fluctuations. Figure reproduced from Ref. [136].

In addition to the previously mentioned study by Arpino et al. that found a dependence of stoichiometry on the Curie-Weiss temperature [92], Chang et al. [103] observed reduced intensity of extended x-ray absorption fine structure data for single crystals of $Yb_2Ti_2O_7$ with lower heat capacity peaks leading them to conclude the Yb deficiency is the key factor for the nature of the heat capacity. Other investigations have postulated that that the dominant mode of defects in these samples arise from light stuffing by rare earth atoms on the titanium sites [100, 101, 139].

1.5 Structure of thesis

$Yb_2Ti_2O_7$ is an ideal opportunity to study magnetic frustration in a quantum liquid. These reported differences in the ground state of $Yb_2Ti_2O_7$ suggest a role for intrinsic

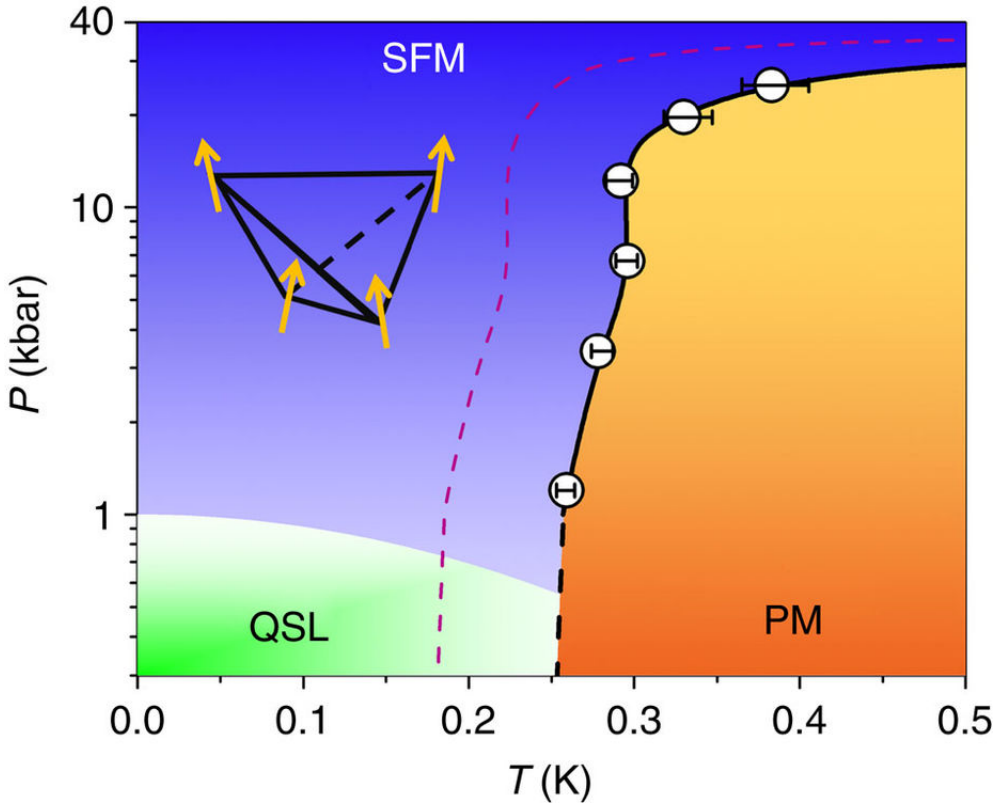

Figure 1.24: Schematic phase diagram as a function of pressure and temperature. Above ambient pressure and at low temperature the system assumes a splayed ferromagnetic ordering and upon increasing temperature $Yb_{2+x}Ti_{2-x}O_{7+\sigma}$ transitions to a collective paramagnetic state. For low and ambient pressures with T below $T_c\sim$ 250 mK a quantum spin liquid state is predicted. Nominally, the diagram corresponds to $x = 0$ but the dashed purple line represents a $x = 0.046$ stuffed sample. Figure reproduced from Ref. [137].

defects in nominally stoichiometric samples. In this thesis the structural defects of $Yb_2Ti_2O_7$ will be investigated and their effect on spin correlations will be explored. In the next chapter the techniques employed will be described, with particular emphasis on diffuse neutron scattering for the determination of defect structures, and polarised

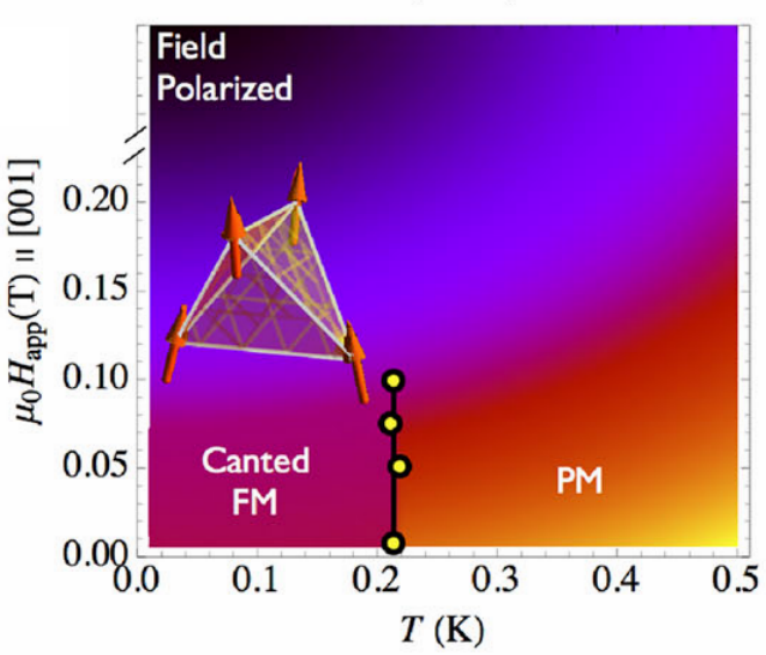

Figure 1.25: Phase diagram for applied field and temperature for $Yb_2Ti_2O_7$ showing the canted ferromagnet, paramagnet and field-polarised regions. Filled circles represent peaks in the heat capacity. Figure reproduced from Ref. [138].

neutron scattering for the study of spin correlations. Chapter 3 presents the results on defect structures and chapter 4 presents the results on magnetic ordering. In chapter 5 conclusions are drawn and the future outlook will be discussed.

Chapter 2

Experimental techniques

2.1 The Crystal Lattice

Crystals consist of a lattice of repeating regular cells of atoms. These cells, a unit cell, can be described by a volume with sides of length a, b, c and angles between these sides of α, β, γ. The content of a unit cell can be of any size providing they repeat throughout the crystal. They can be as small as a single atom or take the form of a biological molecule although convention dictates that it is the smallest volume that displays the highest possible symmetry. The geometric planes within a crystal can be described by its Miller indices given as (hkl). If we take the vectors along each axis of the cell as **a**, **b**, **c** then (100) is a set of planes parallel to the plane containing vectors **b** and **c**. This is because the a plane with a Miller index (hkl) will make an intercept on the axes with a ratio $a/h : b/k : c/l$ so a (222) plane will make an intercept at the halfway point of each axis of the cell.

2.2 The Reciprocal Lattice

The reciprocal lattice is a conceptually useful idea that allows for the description of a parameter space in terms of the momentum change of diffracted neutrons or x-rays. The reciprocal lattice is the Fourier transform of the crystal lattice and vice versa so this construct allow for the determination of the crystal lattice from the diffraction pattern of a crystal.

More concretely this lattice can be derived from the crystal lattice vectors, to obtain the reciprocal lattice vectors [140]:

$$\mathbf{a}^* = \frac{2\pi}{V}(\mathbf{b} \times \mathbf{c}) \tag{2.1}$$

$$\mathbf{b}^* = \frac{2\pi}{V}(\mathbf{c} \times \mathbf{a}) \tag{2.2}$$

$$\mathbf{c}^* = \frac{2\pi}{V}(\mathbf{a} \times \mathbf{b}) \tag{2.3}$$

where V is the unit cell volume which can be obtained as $V = \mathbf{a}\cdot(\mathbf{b} \times \mathbf{c})$. A Bragg peak is typically defined using reciprocal lattice vectors via the wavevector
$\mathbf{Q} = h\mathbf{a}^* + k\mathbf{b}^* + l\mathbf{c}^*$ corresponding to the reflection described as (hkl).

2.3 Scattering

2.3.1 Scattering from a single atom

As this thesis focuses on neutron scattering the following derivations will use a neutron scattering length rather than an atomic form factor for simplicity. Consider a beam of

neutrons with a wavelength λ propagating in the z direction. This can be described using the complex wave equation:

$$\psi_i = \psi_0 e^{ikz} \tag{2.4}$$

where the incident flux is $\Phi = |\psi_0|^2$ and $k = 2\pi/\lambda$. For the sake of simplicity we will assume this beam interacts with a single fixed atom, i.e. one where we assume there is no transfer of momentum between atom and beam so the interaction is elastic. More formally this means that the incident wavevector is equal to the outgoing wavevector: $k_i = k_f$. After interacting with the atom the neutrons are scattered radially from the atom, which we will define as the origin of the system. We will also define a displacement vector $\mathbf{r}$ parallel to the scattered wavevector k_f giving us the expression $\mathrm{e}^{ik_f \cdot \mathbf{r}} = \mathrm{e}^{ikr}$ as $r = |\mathbf{r}|$. It can be assumed that the incident beam is collimated and therefore the number of particles in the beam is independent of distance propagated but the outgoing particles will have a density with an inverse square dependence. The scattered wave will therefore take the form:

$$\psi_f = -\psi_0 b \frac{e^{ikr}}{r} \tag{2.5}$$

where b refers to the neutron scattering length and the minus sign is simply a matter of convention. This value varies by atom and isotope and is an experimentally realised number that determines the scattering intensity.

2.3.2 Scattering cross-section

It will be useful to understand the relationship between the scattering length and the scattering cross section, σ. The scattering rate over all directions, R, has dimension s^{-1}

and the incident flux has dimension $s^{-1}m^{-2}$ which leads to the scattering cross-section to be expressed as [141]:

$$\sigma = R/\Phi. \tag{2.6}$$

What this in effect means is that the cross-section has units m^2 and is equivalent to the hit-rate of a target of unit area perpendicular to the incoming beam.

The number of particles of a given wavelength deflected in a direction (2θ, ϕ) per unit time and unit area can be expressed as the modulus of the scattered wavefunction:

$$|\psi_f|^2 = \psi_f \psi_f^* = \frac{\Phi}{r^2}|b|^2 \tag{2.7}$$

and integrating over all angles gives:

$$R = \int_{2\theta=0}^{\pi} \int_{\phi=0}^{2\pi} |\psi_f|^2 d\mathrm{A}. \tag{2.8}$$

In a spherical polar system $\mathrm{dA} = r^2 \sin 2\theta d\phi d2\theta$ so this allows for the cross-section to be expressed as:

$$\sigma = 2\pi \int_{2\theta=0}^{\pi} |b|^2 \sin 2\theta d2\theta \tag{2.9}$$

which reduces to

$$\sigma = 4\pi |b|^2. \tag{2.10}$$

The scattering-cross section is an important quantity as it relates to the basic quantity that is measured in a scattering experiment, the differential cross-section. This is the

ratio of the number of neutrons deflected by a given angle per unit solid angle to the number of particles per unit area of beam. This can be expressed as:

$$\frac{d\sigma}{d\Omega} = \frac{R(2\theta, \phi)/\Delta\Omega}{N\Phi} \tag{2.11}$$

where $\Delta\Omega$ is the solid angle subtended by the deflected beam and the differential cross-section is the quantity $d\sigma/d\Omega$.

2.3.3 Scattering from multiple atoms

While the case of a single atom is a useful example to examine the basic principles of neutron scattering, in reality neutrons will be scattering from a large assembly of atoms. The contribution to the scattered wave by a single atom j is expressed as [141]:

$$[\delta\psi_f]_j = -b\psi_0 e^{i\mathbf{k}_i\cdot\mathbf{R}_j}\frac{e^{i\mathbf{k}_f\cdot(\mathbf{r}-\mathbf{R}_j)}}{|\mathbf{r}-\mathbf{R}_j|} \tag{2.12}$$

the use of $|\mathbf{r}-\mathbf{R}_j|$ is on account of the fact that the atom cannot be assumed to be at the origin so $\mathbf{R}_j$ describes the position of the atom relative to an arbitrary origin and $\mathbf{r}$ is a vector determining the point relative to the origin at which the wave is measured.

The scattered wavefunction can be obtained by summing over each atom in a scattering system of N particles.

$$\psi_f = -\psi_0 e^{i\mathbf{k}_f\cdot\mathbf{r}}\sum_{j=1}^{N} b_j\frac{e^{i\mathbf{Q}\cdot(\mathbf{r}-\mathbf{R}_j)}}{|\mathbf{r}-\mathbf{R}_j|}. \tag{2.13}$$

Here, $\mathbf{Q}$ represents the scattering vector defined as $\mathbf{Q} = \mathbf{k}_i$-$\mathbf{k}_f$. Eqn. 2.13 is essentially a formalisation of the superposition principle with there being an effective sum over a number of scattered waves. This equation also relies on the Born approximation which assumes that the scattering process is sufficiently weak that the scattered wave does not

interfere with the incident wave. There is also an assumption that there is no multiple scattering so after being scattered a wave does not go on to be scattered by another nucleus. In reality multiple scattering events are an important factor in calculating the scattered wavefunction, especially when scattering from large samples.

Typically, and in the case of all the experiments included in this thesis, the distance from the sample to the detector is much larger than the dimensions of the sample so setting the origin to be inside the sample and taking $\mathbf{r}$ to be at the detector of interest then: $\mathbf{r} \gg \mathbf{R}_j$ such that:

$$|\mathbf{r} - \mathbf{R}_j| = |\mathbf{r}| = r \tag{2.14}$$

as r can now be expressed as a scalar quantity as it is only a useful to consider as a vector relative to $\mathbf{R}_j$. This allows us to obtain a much simplified version of the scattered wavevector that can be used to obtain an expression for the differential cross-section in terms of the specific system of interest. First the rate at which neutrons are scattered into a detector at a given angle can now be calculated for an ensemble of atoms. As $\delta\Omega = \delta A/r^2$ on account of the fact that the area swept out by a solid angle will increase with the square of the radius, we can express the rate per unit time as:

$$R(2\theta, \phi) = |\psi_f|^2 \delta A = \Phi \delta\Omega \sum_m \sum_n b_m b_n e^{i\mathbf{Q}\cdot(\mathbf{R}_m - \mathbf{R}_n)} \tag{2.15}$$

substituting back into Eqn. 2.11 we finally obtain:

$$\frac{d\sigma}{d\Omega} = \frac{1}{N} \sum_m \sum_n b_m b_n e^{i\mathbf{Q}\cdot(\mathbf{R}_m - \mathbf{R}_n)}. \tag{2.16}$$

2.4 Bragg's Law

Having derived an expression for the differential cross-section it will be useful to consider the conditions under which scattering will occur in the first place. We can define atomic planes using any three non-collinear vectors so we can construct a set of planes using integer multiples of **a**, **b** and **c**. Scattering can be detected when the incident neutrons are scattered coherently so for a given value of 2θ the path difference must be an integer multiple of the wavelength. From considering the a regularly spaced plane of atoms we can see that there is path difference of:

$$\Delta L = 2d\sin\theta \tag{2.17}$$

and given the required conditions for diffraction:

$$N\lambda = 2d\sin\theta. \tag{2.18}$$

This is referred to as Bragg's law. We can relate this expression back to that of the wavevector **Q**. Recalling that $\mathbf{Q} = \mathbf{k}_i\text{-}\mathbf{k}_f$, and knowing that **Q** is perpendicular to the scattering plane illustrated in Fig. 2.1, then clearly:

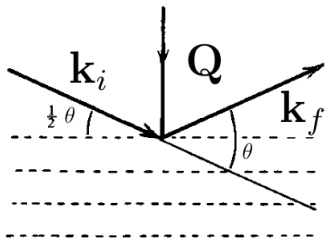

Figure 2.1: Schematic illustrating Bragg's law, relating $\mathbf{k}_i$ and $\mathbf{k}_f$ to the planes of atoms.

$$\frac{\mathbf{Q}}{2} = |\mathbf{k}_i|\sin\theta = \frac{2\pi}{\lambda}\sin\theta \tag{2.19}$$

which can be reduced to

$$\mathbf{Q} = \frac{4\pi\sin\theta}{\lambda}, \tag{2.20}$$

and finally

$$\mathbf{Q} = \frac{2\pi}{d}. \tag{2.21}$$

What this tells us is that the integer values of hkl are directly related the interplanar spacing.

2.5 Polarised Neutron Scattering

Atoms with unpaired electrons will have a magnetic moment that interacts with the moment of the incident neutrons (which are spin 1/2 particles) giving scattering effects that happen in addition to the previously discussed nuclear scattering. Elastic scattering of this kind gives information about the density distribution of unpaired electrons and when combined with a spin-polarised beam of neutrons information about the spin distribution of a crystal allowing for determination of its magnetic behaviour. Along some axis of quantisation such as a magnetic field neutrons can either lie parallel or anti-parallel to the field referred to as spin-up and spin-down states. A beam of neutrons can be described by its polarisation which is defined as [140]:

$$P = \frac{n_- - n_+}{n_+ + n-}. \tag{2.22}$$

This is only valid for uniaxial polarisation which is sufficient for this thesis as no other form of polarisation analysis will be used. For P = ±1 the beam is completely polarised along a given axis while P = 0 describes a completely unpolarised beam. The strength of the magnetic interaction will be determined by the magnetic interaction vector given for an atom j as:

$$\mathbf{q_i} = \mathbf{Q}(\mathbf{Q} \cdot \boldsymbol{\mu_j}) - \boldsymbol{\mu_j} \tag{2.23}$$

where $\boldsymbol{\mu}_j$ is the magnetic moment of the atom being scattered from and $\mathbf{Q}$ is the wavevector of the incident neutron. What Eqn. 2.23 effectively means is that for an atom to contribute to the magnetic scattering intensity it must have a component of its magnetic moment perpendicular to $\mathbf{Q}$. For a crystal where the magnetic moments are uniaxially aligned such as a ferromagnetic sample, there will be no magnetic scattering when the the magnetic moments are aligned parallel to the wavevector.

2.6 Diffuse Scattering

Diffuse scattering arises from a breakdown of the space group symmetry in crystalline materials. There are a number of different ways in which diffuse scattering can arise and can be elastic, quasi-elastic or inelastic in nature. For the purposes of this thesis it will be sufficient to consider only elastic diffuse scattering and diffuse scattering arising from static disorder and magnetic disorder. While there will certainly be diffuse scattering arising from thermal effects which is not possible to completely decouple from other forms of scattering, in the experiments to be discussed the highly defective nature of the crystals used means that static disorder will give a particularly large scattering signature.

Static disorder considers disorder arising from positional defects that do not have

a significant time dependence, excluding thermal effects. This predominantly involves substitutional disorder which is when the same site in different unit cells is occupied by a different species of atom or vacancies. Since diffuse scattering studies look at deviations from the average crystal structure, it is the case that the strength of diffuse scattering intensity is typically far less than that at the Bragg peaks and unlike Bragg peaks will not sit exclusively on reciprocal lattice points. A consequence of this weaker signal means that much larger count times are required to get a statistically significant result. Since for the experiments featured in this study the most common type of defect arises from the static disorder of oxygen atoms, neutrons, rather than x-rays, are used on account of their scattering length in order to have a sufficient cross section relative to the larger rare earth atoms commonly present in the pyrochlore systems. A consequence of this is that very large count times are required so an experiment on a single crystal sample would typically take between three days and a week.

The expression given for the derivative of the scattering cross section in Eqn. 2.16 can be extended to account for static disorder by the following equation [142]:

$$\frac{d\sigma}{d\Omega} = \frac{1}{N}\sum_{m}\sum_{n} b_m b_n e^{i\mathbf{Q}\cdot(\mathbf{R}_m-\mathbf{R}_n)} e^{i\mathbf{Q}\cdot(\boldsymbol{\delta}_m-\boldsymbol{\delta}_n)} \tag{2.24}$$

where $\boldsymbol{\delta}$ is the deviation from the average position $\mathbf{R}$ such that the actual static position for an atom m is $\mathbf{r}_m$=$\mathbf{R}_m$+$\boldsymbol{\delta}_m$.

2.7 Production of Neutrons

There are many different ways of creating a source of neutrons so this section will limit the discussion to those that are used in the following chapters. These are production via spallation which is used at ISIS and production via nuclear fission used at the ILL.

2.7.1 The ISIS Pulsed Spallation Source

Neutrons are created at ISIS by a technique called spallation in which a high energy proton interacts with a heavy nucleus whereby between 20-40 neutrons are evaporated and used for the scattering process [140].

A linear accelerator accelerates H^- ions to 70 MeV creating a 50 Hz pulsed beam. This beam is incident on thin film of aluminium which strips the electrons from the H^- ion. These protons are then fed into the beamline of a synchrotron. The synchrotron itself consists of 10 sections of magnets for accelerating and then bending the beam into the following section. The RF cavities of these sections increase in frequency with the acceleration of the protons causing the beam to accelerated to 800 MeV within a period of 10 ms. Each bunch of protons is 90 ns wide and is separated from the next bunch by 210 ns. Each bunch being fed into the extracted proton beamline which uses quadrupole magnets contains around 2.5×10^{13} protons giving an average current of 200 μA. The beam is directed into a target station consisting of a series of tantalum plates. The target is surrounded by three layers of moderators: 300 K water, 105 K liquid methane and 25 K liquid hydrogen. The target has a number of beam holes allowing neutrons to escape which are then able to reach the instruments used in the scattering experiments.

2.7.2 The ILL Reactor Source

The ILL uses a ^{235}U fission isotope which has many potential decay products but on average the decay of a ^{235}U isotope will produce 2.7 fast neutrons [140]. The disintegration nuclei are often unstable and will decay further producing even more neutrons. These neutrons will interact with additional ^{235}U atoms causing a chain reaction of disintegrations. To prevent the rate of decay from increasing exponentially, on average all but one of the neutrons produced from a disintegration will either be absorbed or

escape the reactor. It is the these escaping neutrons that are utilised for scattering.

The beam itself has a flux of 1.5 $\times$ 10^{15} $cm^{-2}s^{-1}$ with a wavelength distribution peaking at 1.2 Å. A D_2O moderator kept at 300 K is used although for thermal beamlines, a 2,400 K graphite source is used to enhance the flux at the low wavelength end of the spectrum and a deuterium source at 20 K is used for long wavelength neutrons. The ^{235}U fuel element is cooled with water pumped in at 15.5 ms^{-1} that removes 58 MW of power generated by the fission process. The coolant also serves to moderate the neutrons and along with the D_2O moderator reflects neutrons back into the core to continue the chain reaction. Tubes penetrating the exterior wall of the reactor allow for the neutrons to escape forming a continuous beam of neutrons that are fed down into the instruments populating the facility's two guide halls.

2.8 Neutron Instruments

There are two different neutrons instruments featured in this thesis. Chapter 3 will focus on data acquired on SXD at ISIS and and chapter 4 will discuss the results of experiments conducted on D7 at ILL.

2.8.1 SXD

The SXD single crystal diffractometer at ISIS has a large sample space allowing for the addition of cryostats and furnaces and is surrounded by 11 large area detectors [143]. The large area of detector banks makes it ideal for studying diffuse scattering due to broad coverage of reciprocal space. Combining the large region of reciprocal space available from the wide detector banks with data symmetrisation allows for the determination of the scattering from defect structures within only a few days of counting.

SXD is a time of flight instrument so the energy of the incident neutrons is calculated from their velocity by knowing the time difference between spallation and detection. This however assumes elastic scattering although the advantage of this is that the full spectrum of neutron wavelengths are used maintaining a higher count rate.

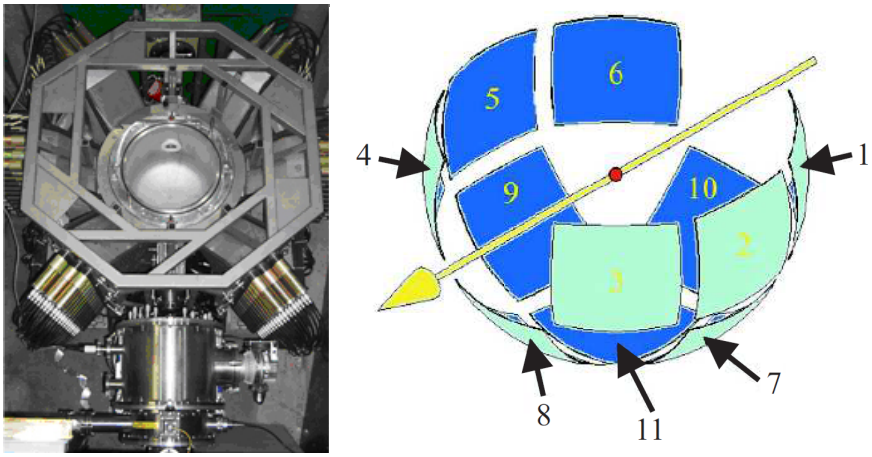

(a) (b)

Figure 2.2: (a) A photograph of the SXD instrument and (b) an illustration of the 11 detector banks relative to the incident beam and sample. Figures reproduced from [143], and [144] respectively.

2.8.2 D7

The D7 diffuse scattering spectrometer is a cold neutron instrument that is designed for polarisation analysis [145]. D7 features wide detector banks which allows for three dimensional polarisation analysis although only uniaxial polarisation experiments are discussed in this thesis. Since polarisation analysis allows for the isolation of magnetic scattering this instrument enables the study of weak magnetic scattering features over a wide range of $\mathbf{Q}$. This is useful for our purposes as the determination of defect structures

and short-range order will typically only give a weak scattering signal requiring large banks of detectors to give meaningful scattering intensity over a sufficient **Q** range. The flux of polarised neutrons on D7 is approximately 10^6 neutrons $cm^{-2}s^{-1}$. A Fermi chopper can also be employed in D7 experiments allowing for analysis of energy transfer, but this results in a large decrease in intensity, and this technique is not used in this thesis.

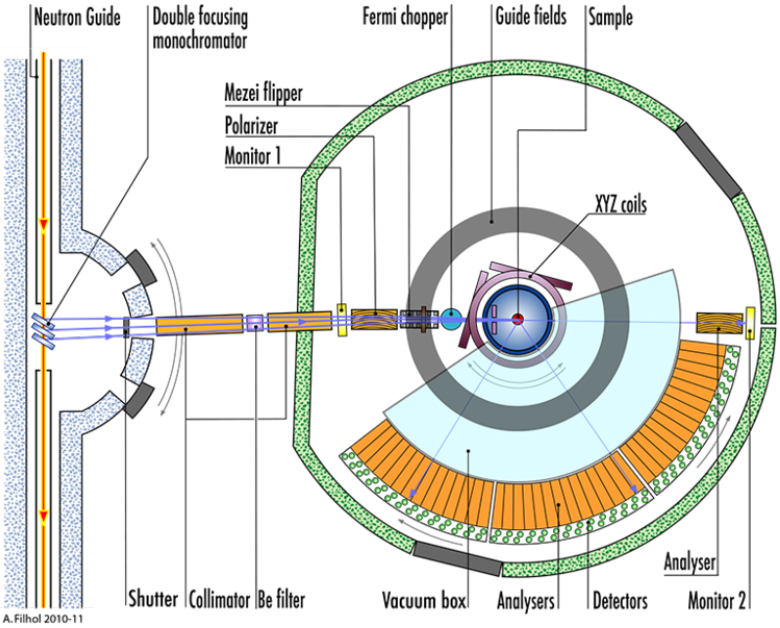

Figure 2.3: Schematic showing the layout of the D7 instrument at the ILL. Figure reproduced from [145].

Figure 2.3 shows a schematic of the instrument. Neutrons are first monochromated to a given wavelength and higher orders of the incident wavelength are removed using a beryllium filter. The neutrons are polarised into a spin-up state using a supermirror and then pass through a Mezei π spin flipper if reversing the spin state is required. A guide field of approximately 0.01 T is applied to sustain the polarisation, and orthogonal magnetic coils surround that sample space allowing for the axis of polarisation to be

selected. The neutrons then interact with the sample after which they are analysed by supermirrors which allow only those neutrons of a certain spin to pass through. The polarisation of the scattered neutrons can be rotated by $\pi/2$ in order to detect both spin-flip and non-spin-flip channels of neutrons. The analysed neutrons are then detected by banks of ^{3}He tubes.

The detectors are calibrated for their varying efficiencies by scattering from a vanadium standard sample which has an extremely small coherent cross-section and isotropic incoherent scattering allowing for the differential cross-section in each detector to be normalised.

The flipping ratio of each supermirror can be determined to ensure a sufficiently high degree of separation between the non-spin-flip and spin-flip channels. This is measured by scattering from a sample of amorphous SiO_2 which has an almost perfectly non-spin-flip cross-section. The background can be calculated by scattering from an empty sample holder and from cadmium, an element with excellent neutron absorption characteristics.

2.8.3 Crystal growth

The growth of single crystals of $Yb_2Ti_2O_7$ is a non-trivial process so all of the crystals measured in this thesis were grown by Dr D. Prabhakaran at the Clarendon Laboratory, University of Oxford. They were grown from a compressed boule of powder with the appropriate constituent compounds and formed using an image furnace whereby the growth environment can be controlled so the heat, atmosphere and the speed of the movement of the boule can be precisely determined. High powered arc lamps are focused onto a portion of the growth material causing it to form a molten state which then solidifies into a crystalline structure upon cooling. This boule is moved such that its entirety is exposed to the heat region during the growth process so the boule is

turned into a single crystal.

2.8.4 Crystal refinement

Given a set of reflections from a crystal an attempt can be made to determine the composition and position of the atoms in the crystal using structural refinement which is performed using the JANA2006 software [146]. A virtual crystal is created and the virtual reflections from this are calculated and compared to the experimentally acquired values. The virtual crystal is refined using a least square fit with respect to the two sets of reflections. Different crystallographic parameters can be fixed or freed on a more or less ad hoc basis to reduce the size of the parameter space being minimised until a satisfactory fit is found. This fit is given by a weighted R factor defined as:

$$R_w = \sqrt{\frac{\sum \left|\omega \left|\mathrm{I}_{exp} - \mathrm{I}_{calc}\right|^2\right|}{\sum \left|\omega \, {\mathrm{I}_{exp}}^2\right|}} \tag{2.25}$$

where the weighting factor, ω is usually $1/\Delta {\mathrm{I}_{exp}}^2$ [147]. This parameter gives a percentage fit to the experimental data, where a value $< 20\%$ would be a good fit and $>70\%$ has no connection to the experiment.

2.9 Magnetism

2.9.1 The spin Hamiltonian

In general, the interaction between magnetic moments depends upon both the dipolar interactions and the exchange interactions. From an understanding of these interactions a derivation of the spin Hamiltonian can be obtained. The exchange interaction stems from the Pauli exclusion principle which states that two or more identical fermions (particles with half-integer spin) cannot occupy the same quantum state within a quantum system simultaneously [148]. For the classical spin ices the dipolar interactions are considered to be particularly important as the strong dipole moment of the rare earth ions means a dipolar model gives an approximate description [149]. Nevertheless, the dipolar interactions can be mapped onto an effective nearest neighbour exchange model, in contrast in $Yb_2Ti_2O_7$ the relatively small magnetic moment of Yb of approximately 4 μ_B is less than half that of Ho at approximately 10 μ_B [105], and in this case the exchange interaction is expected to be dominant. The following derivation will follow those given in Refs. [150, 151].

For a quantum mechanical system the spin interaction between two electrons is proportional to

$$\hat{\mathbf{s}}_1 \cdot \hat{\mathbf{s}}_2 \tag{2.26}$$

where $\hat{\mathbf{s}}_i = (\hat{\mathbf{s}}_i^x, \hat{\mathbf{s}}_i^y, \hat{\mathbf{s}}_i^x)$ is the spin operator for a given electron. The total spin operator for a system of two spins is given as the sum of those spins such that

$$(\hat{\mathbf{S}})^2 = (\hat{\mathbf{s}}_1)^2 + (\hat{\mathbf{s}}_2)^2 + 2\hat{\mathbf{s}}_1 \cdot \hat{\mathbf{s}}_2. \tag{2.27}$$

Eqn. 2.26 then becomes

$$\hat{\mathbf{s}}_1 \cdot \hat{\mathbf{s}}_2 = \frac{(\hat{\mathbf{S}})^2 - [(\hat{\mathbf{s}}_1)^2 + (\hat{\mathbf{s}}_2)^2]}{2}. \tag{2.28}$$

for a fermion system with $\mathbf{s}_1 = \mathbf{s}_2 = 1/2$ so the squared single spin operators take the value $(\hat{\mathbf{s}}_i)^2 = \mathbf{s}_i(\mathbf{s}_i{+}1) = 3/4$, thus

$$\frac{S(S+1) - [3/2]}{2} = \begin{cases} \frac{1}{4}, & \text{if S} = 1 \\ -\frac{3}{4}, & \text{if S} = 0. \end{cases} \tag{2.29}$$

This gives two possible eignenvalues for the spin interaction for either a triplet or singlet eigenstate. For a system of electrons the the overall wavefunction must be antisymmetric which leads to different wavefunctions for singlet χ_S and triplet χ_T spin states for two electron wavefunctions ψ_a and ψ_b:

$$\Psi_S = \frac{1}{\sqrt{2}}[\psi_a(\mathbf{r}_1)\psi_b(\mathbf{r}_2) + \psi_a(\mathbf{r}_2)\psi_b(\mathbf{r}_1)]\chi_S \tag{2.30}$$

$$\Psi_T = \frac{1}{\sqrt{2}}[\psi_a(\mathbf{r}_1)\psi_b(\mathbf{r}_2) - \psi_a(\mathbf{r}_2)\psi_b(\mathbf{r}_1)]\chi_T \tag{2.31}$$

where $\psi_a(\mathbf{r}_i)$ is the spatial component for a single electron wavefunction. The non-normalised energies for the singlet and triplet states are given as

$$E_S = \int \Psi_S^* \hat{H} \Psi_S d\mathbf{r}_1 d\mathbf{r}_2 \tag{2.32}$$

$$E_T = \int \Psi_T^* \hat{H} \Psi_T d\mathbf{r}_1 d\mathbf{r}_2. \tag{2.33}$$

From the eigenvalues obtained above an effective Hamiltonian can be given as

$$\hat{\mathcal{H}} = \frac{1}{4}(E_S + 3E_T) - (E_S - E_T)\hat{\mathbf{s}}_1 \cdot \hat{\mathbf{s}}_2. \tag{2.34}$$

The two components in the above equation are a constant term and one with a spin component. The exchange constant is related to this as

$$\mathrm{J} = \frac{E_S - E_T}{2} = \int \psi_a^*(\mathbf{r}_1)\psi_b^*(\mathbf{r}_2)\hat{\mathcal{H}}\psi_a^*(\mathbf{r}_2)\psi_b^*(\mathbf{r}_1)d\mathbf{r}_1 d\mathbf{r}_2. \tag{2.35}$$

Hence the spin component of the Hamiltonian can be expressed as

$$\hat{\mathcal{H}}^{spin} = -\mathrm{J}\mathbf{s}_1 \cdot \mathbf{s}_2. \tag{2.36}$$

Clearly J expresses the relative values of E_S and E_T such that for $\mathrm{J} > 0$ the $\mathrm{S} = 1$ triplet state is favoured and for $\mathrm{J} < 0$ the singlet state is.

2.9.2 The Weiss Model

If this Hamiltonian is extended to include a sum over all the moments and an external field, **B** is introduced the Hamiltonian will now take the form

$$\hat{\mathcal{H}}^{spin} = -\sum_{ij} \mathrm{J}_{ij}\mathbf{S}_i \cdot \mathbf{S}_j + g\mu_B \sum_j \mathbf{S}_j \cdot \mathbf{B}. \tag{2.37}$$

The new term is the Zeeman energy which corresponds to the potential energy of a system in an applied magnetic field. This model is simplified in making the assumption that there is no orbital angular momentum such that the total angular momentum, **J** = **S**. An effective molecular field on the i^{th} site can be defined as

$$\mathbf{B}_{mf} = -\frac{2}{g\mu_B}\sum_j \mathrm{J}_{ij}\mathbf{S}_j \tag{2.38}$$

and this in effect describes the ordering of the system so can alternatively be considered as

$$\mathbf{B}_{mf} = \lambda\mathbf{M}. \tag{2.39}$$

Considering the exchange component of the Hamitonian given in Eqn. 2.37 if one considers the interaction between the i^{th} spin and the neighbouring spins this term can be expressed alternatively as

$$-2\mathbf{S}_i \cdot \sum_j \mathrm{J}_{ij}\mathbf{S}_j = -g\mu_B \mathbf{S}_i \cdot \mathbf{B}_{\mathrm{mf}} \tag{2.40}$$

where the 2 accounts for double counting of the spins. This leads to a Hamiltonian described by a system of spins producing an effective molecular field as

$$\hat{\mathcal{H}}^{spin} = g\mu_B \sum_i \mathbf{S} \cdot (\mathbf{B} + \mathbf{B}_{\mathrm{mf}}). \tag{2.41}$$

What this indicates is that the moments of a system can order without the need for the application of an external magnetic field as the Hamiltonian will take a non-zero value even when $\mathbf{B} = 0$. The order arising from this will then contribute to the internal molecular field reinforcing the magnetic ordering across the system. This is only true in the case that thermal fluctuations are sufficiently low that they do not cause a break down in the ordering of the moments. The transition temperature whereby spontaneous magnetism arising from the internal moments of a system is refereed to as the Curie temperature, Θ_C and is defined as

$$\Theta_C = \frac{g_j \mu_B (\mathrm{J}+1)\lambda M_s}{3k_B} = \frac{n\lambda\mu_{\mathrm{eff}}^2}{3k_B} \tag{2.42}$$

where M_s is the saturation magnetisation and μ_{eff} is the effective magnetic moment per formula unit. This quantity is related to the magnetic susceptibility as

$$\chi = \lim_{B\to 0} \frac{\mu_0 M}{B} \propto \frac{1}{T - \Theta_C} \tag{2.43}$$

which is referred to as the Curie-Weiss law.

The sign and magnitude of the Curie temperature describes the nature of the magnetic interactions whereby a negative Θ_C would describe an antiferromagnetic material. Magnetic ordering is expected at the temperature Θ_C. The ordering temperature is called the Curie temperature for a ferromagnet and the Néel temperature T_N for an antiferromagnet.

2.9.3 Frustration factor

Competing interactions in low dimensionality can lead to ordering temperatures significantly lower than the Curie-Weiss temperature. Spin ice systems are prototypical examples of geometrical frustration in three dimensions, where it is difficult to satisfy all of the bonds on the pyrochlore lattice simultaneously. The relationship between T_N and Θ_C can be used to quantify the degree of frustration for a given system, $f \equiv \mid \Theta_C \mid /T_N$. A large value of f would be a strong signature of frustration [152].

2.9.4 Heat capacity

The heat capacity of a system at constant volume is defined as

$$c_V = \left(\frac{\delta E}{\delta T}\right)_V \tag{2.44}$$

that is to say that the heat capacity determines the energy needed to be put into a system to change its temperature. The dominant factor contributing to the heat capacity of a material are its thermal fluctuations meaning that a description in terms of the phonon frequency is useful [153]. At low temperature there is typically an additional non-negligible magnetic contribution. As the temperature of a system tends towards zero so too does the heat capacity which means that it is possible to measure the magnetic contribution accurately. The heat capacity is of particular relevance to those interested in phase transitions as an anomaly in a plot of heat capacity versus

temperature indicates such a transition. This technique is frequently used in studies of $Yb_2Ti_2O_7$ to determine the transition temperature between its magnetic states [104, 118, 123, 124, 125, 126]. Not all peaks in the heat capacity indicate a phase transition however. If one considers a system with two energy levels, for a spin = 1/2 paramagnet the heat capacity is given as

$$C = Nk_B\left(\frac{\Theta}{T}\right)^2 \frac{e^{\Theta/T}}{(e^{\Theta/T}+1)^2} \tag{2.45}$$

where $\Theta = \frac{2\mu B}{k_B}$. At a low energy only the lowest energy states will be occupied, not having enough energy to be promoted to the higher energy level. As the temperature and therefore thermal energy increases towards the energy representing the energy difference between the two states, thermal excitations will allow for the population of the higher energy state. At high temperature, it is hard to change the energy of the system because both states are equally occupied. In between there is a maximum. This type of specific heat anomaly is referred to as a Schottky anomaly [150]. It is a broad maximum in contrast to the sharp peaks associated with phase transitions.

2.9.5 Crystal electric field

The 4f electrons determining the magnetism of the system are in an inhomogeneous electrostatic field arising from the surrounding ions which has a symmetry determined by that of the crystal lattice and is referred to as the crystal electric field. For an electron with charge -e, this makes a contribution to the potential energy as

$$\mathrm{v}_{cf}(r) = -\int \frac{\mathrm{e}\rho(R)}{|r-R|} dR \tag{2.46}$$

where $\rho(R)$ is a function of the charge density of the surrounding environment. If this function is considered to have no overlap with the 4f charge cloud this function

is a solution of the Laplace equation and can subsequently be exapnded as a spherical harmonic function as

$$\mathrm{v}_{cf}(r) = \sum_{l,m} A_l^m r^l Y_l^m(r_i). \tag{2.47}$$

Summing over the 4f shell yields a Hamiltonian

$$\hat{\mathcal{H}}_{cf} = \sum_i \sum_{l,m} A_l^m r^l Y_l^m(r_i) \tag{2.48}$$

which by replacing the spherical harmonics by operators acting in place of angular momentum operators [154] can be given as

$$\hat{\mathcal{H}}_{cf} = \sum_{l,m} A_l^m \langle r^l \rangle \langle J||\Theta_l||J\rangle \hat{\mathrm{O}}_l^m(J). \tag{2.49}$$

This is the Stevens crystal field Hamiltonian where $A_{lm}\langle\ r^l\rangle$ is the crystal field parameter, $r^l\rangle$ is the expectation value of the radial wavefunction. $\langle J||\Theta_l||J\rangle$ are the Stevens factors for l=0,2,4,6 corresponding to the number of electrons in the unfilled shell.

Chapter 3

Structural Diffuse Scattering

3.1 Introduction

Structural disorder in $Yb_2Ti_2O_7$ could potentially lift the degeneracy of the system which would have the consequence of affecting its magnetic properties. For this reason an understanding of the defect structure is essential in being able to confidently determine the magnetism of $Yb_2Ti_2O_7$. In this chapter I will use single crystal diffuse neutron scattering combined with a balls and springs Monte Carlo model in order to determine the nature of the structural disorder in samples of $Yb_2Ti_2O_7$ grown with different types of defects. In doing so, this will allow for the relationship between the defect structure and the magnetism to be determined in the following chapter.

3.2 Results

Three single crystal samples of $Yb_{2+x}Ti_{2-x}O_{7-x/2}$ were grown by Dr D. Prabhakaran using the floating zone method at the Clarendon Laboratory, Oxford University. One sample was measured without further treatment which will thus be referred to as 'as-

grown'. Another was annealed in a mix of hydrogen and argon gas to reduce the concentration of oxygen and led to a black crystal, which will be referred to as oxygen-depleted and a third was grown with an excess of Yb with a nominal growth stoichiometry of $Yb_{2.5}Ti_{1.5}O_{6.75}$ and this sample will be referred to as 'stuffed'. This crystal was orange/brown. Finally after the measurements were completed on the as-grown sample it was annealed in oxygen at a flow rate of 50 ml min^{-1} at a temperature of 1200 °C for 2 days with the aim of removing any isolated oxygen vacancies and will be referred to as 'oxygen-annealed'. This produced a transparent crystal. The samples were measured on a single crystal x-ray diffractometer at room temperature and the subsequent data were used in refinements of the structures, with the results presented in table 3.1. The as-grown sample is absent from these refinements as the x-ray measurements were carried out after the as-grown sample was annealed in oxygen. All of the single-crystal x-ray diffraction data for oxygen-depleted $Yb_2Ti_2O_7$ and stuffed $Yb_{2.5}Ti_{1.5}O_{6.75}$ refine in the cubic pyrochlore structure, space group $Fd\bar{3}m$, with weighted R-factors $R_w \sim$ 3-4. The presence of high atomic number elements means that the sensitivity to oxygen ions is limited, and it is not possible to distinguish between O(1) and O(2) vacancies. However, we note that oxygen depletion does not lead to an increase in lattice parameter, and this is the first difference between $Yb_2Ti_2O_7$ and $Y_2Ti_2O_7$ [91]. In the case of $Y_2Ti_2O_7$ the increase in the lattice parameter was associated with the expansion of the Y tetrahedra around O(1) vacancies, and this is the first indication that the defect structure of $Yb_2Ti_2O_7$ is different. In contrast, for the stuffed sample there is a substantial increase in the lattice parameter, as expected when replacing titanium ions by larger ytterbium ions. This increase in lattice parameter with stuffing is observed for all the titanium pyrochlores, including $Yb_{2+x}Ti_{2-x}O_{7-x/2}$ [155].

The fitted excess ytterbium concentration $x = 0.40(14)$ is close to but slightly lower than the target concentration, $x = 0.5$. All of the following measurements were taken at

$T = 30$ K. A low temperature was chosen in order to suppress the inelastic contributions to the scattering from phonons, while minimising the background signal from the sample environment.

The samples were measured on the single crystal diffractometer (SXD) at ISIS allowing for measurement of a large volume of reciprocal space and to allow for a sufficiently high count as to be able to easily observe diffuse scattering, which naturally has a weaker experimental signature than that of the Bragg peaks.

The diffuse scattering data was treated in the following way using the SXD2001 software: the sample, the background and the vanadium runs were normalised to the count in μAs of the measurement. The background was subtracted from the sample run which was then divided by the vanadium measurement. The sample was measured at several different angles which were then recombined. The volume was symmetrised using the $Fd\bar{3}m$ symmetry and the resultant volume was normalised by the number of data points contributing to each pixel.

For the following figures the $(hk7)$ plane will be used as the main plane of comparison in order to be consistent and for comparison with previous similar work on other systems [70, 91].

Figure 3.1 shows each of the four single crystal scattering patterns all plotted on the same scale to demonstrate the relative strength of the diffuse scattering features with the as-grown and oxygen annealed samples exhibiting relatively similar levels of scattering, the oxygen-depleted having more and the stuffed sample having extremely strong diffuse scattering features. One source of the difference in intensity is the nature of the defect structure. The intensity depends upon the scattering lengths of the defective species, the amplitudes of the displacements of defective ions, and the number of ions included in the extended defect cluster. However, according to the modelling described in this chapter, it is not possible to account for the difference in intensities by the defect

	Stuffed	Depleted	Annealed
Colour	Yellow/Brown	Black	Transparent
Space group	$Fd\bar{3}m$	$Fd\bar{3}m$	$Fd\bar{3}m$
Lattice parameter	10.0838(5) Å	10.0219(4) Å	10.031(1) Å
Yb	1	1	1
Yb2	0.20(7)	0	0
Ti	0.79(3)	1	1
O(1)	1	1	1
O(2)	0.96	0.96	1
x	0.7146(11)	0.716(7)	0.716(3)
Rw	4.24	3.16	3.62

Table 3.1: Refinement results for single crystal x-ray diffraction data for different $Yb_2Ti_2O_7$ compositions carried out in JANA2006. Errors are not provided for the O(2) concentration as these values were set manually and fixed which was required to prevent the values from taking on a value larger than unity. Yb2 refers to Yb atoms on the 16c sites in place of Ti. The small form factor for oxygen means that the oxygen atoms have a very small contribution to the refinement relative to the other atoms. The measurements were taken at T $\sim$ 90 K. The values refer to fractional occupation so Yb2=0.2(7) should be multiplied by two for the x in $Yb_{2+x}Ti_{2-x}O_{7-x/2}$ to equal 0.4(14).

structural model alone. It appears that the stuffed sample has a higher overall defect concentration. Uniform stuffing of ytterbium ions throughout the sample maybe a more effective way of introducing oxygen vacancies across the sample than reduction by hydrogen, which may be less effective deep below the surface of a large crystal.

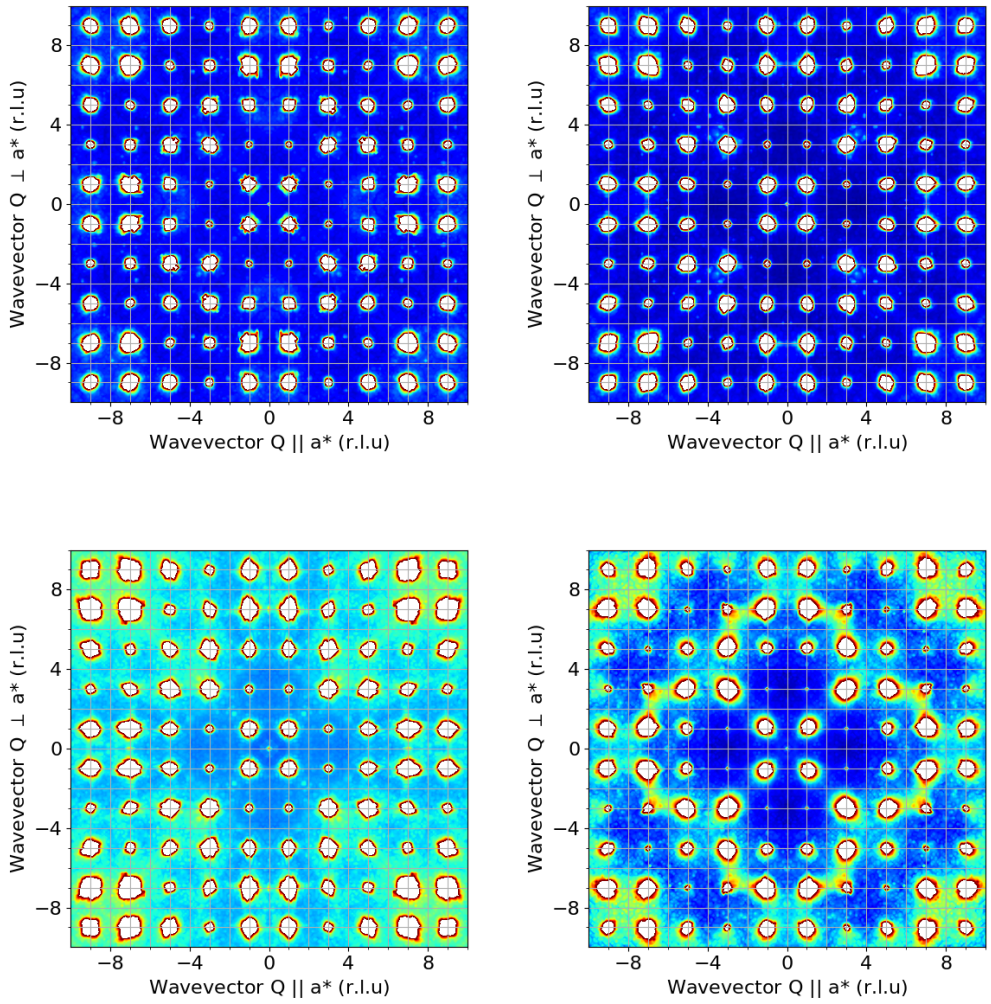

Figure 3.1: Diffuse neutron scattering acquired on SXD for in the ($hk7$) plane for (a) as-grown, (b) oxygen-annealed, (c) oxygen-depleted and (d) stuffed $Yb_2Ti_2O_{7-\delta}$, all plotted on the same scale.

The panels of Fig. 3.1 are also plotted on the same scale for comparison with one another, with the exception being the stuffed sample on account of the higher intensity diffuse scattering features which required a larger maximum contour level. The scattering pattern produced by the as-grown sample shown in Fig. 3.2 clearly exhibits regions of diffuse scattering indicating structural disorder in the system. The lack of diffuse scattering in the oxygen-annealed sample in Fig. 3.3 indicates that annealing in oxygen removes the disorder in the system which proves that for this sample the dominant mode of defects are isolated oxygen vacancies. Both data sets are plotted on the same scale to accurately reflect the reduction in diffuse scattering intensity. This suggests that the nature of the defects are distinct too, although understanding the nature of these defects will require a comprehensive modelling of the defect structure. Figs. 3.4 and 3.5 show the scattering of the oxygen-depleted and stuffed samples respectively. The nature of the scattering is qualitatively different with arc-like features observed in the stuffed sample which are absent in the oxygen-depleted sample.

Whilst this qualitative assessment is largely adequate in seeing the reduction in the disorder of the system, Fig. 3.6 shows a one dimensional cut across the (h 4 6.8) direction. Clearly the oxygen-annealed system has the lowest intensity across the region of diffuse scattering with the as-grown having slightly more. The oxygen-depleted sample however has considerable intensity as would be expected for a system with greater disorder. The stuffed sample is excluded from this comparison on account of the intensity being much higher, making a comparison between the other samples more difficult.

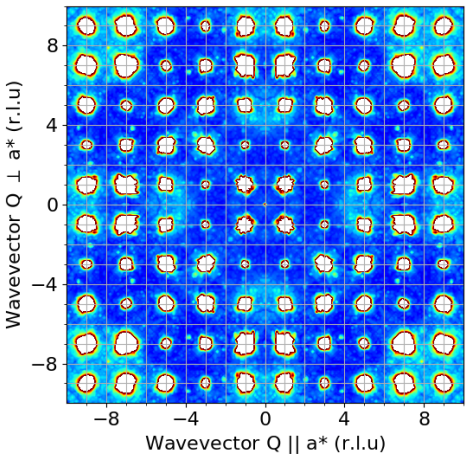

Figure 3.2: As-grown $Yb_2Ti_2O_{7-\delta}$ in the $(hk7)$ plane. The strong diffuse scattering features around (0 5 7) and (8 8 7) are indicative of structural disorder in the sample.

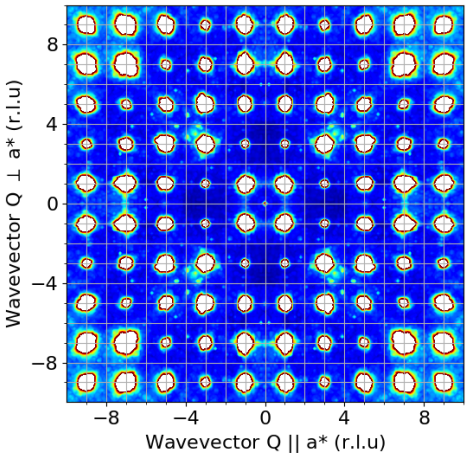

Figure 3.3: Oxygen-annealed $Yb_2Ti_2O_7$ in the $(hk7)$ plane. The diffuse scattering features shown in the as-grown sample are largely suppresed suggesting the removal of disorder in the sample. The remaining weak features could potentially be on account of thermal excitations on account of the relatively high measurment temperature.

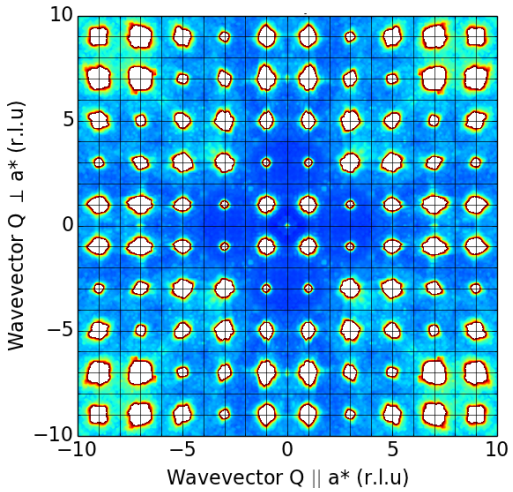

Figure 3.4: Oxygen-depleted $Yb_2Ti_2O_{7-\delta}$ in the $(hk7)$ plane. This sample exhibits qualitatively comparable diffuse scattering features to the as-grown sample indicating that they contain the same mode of disorder.

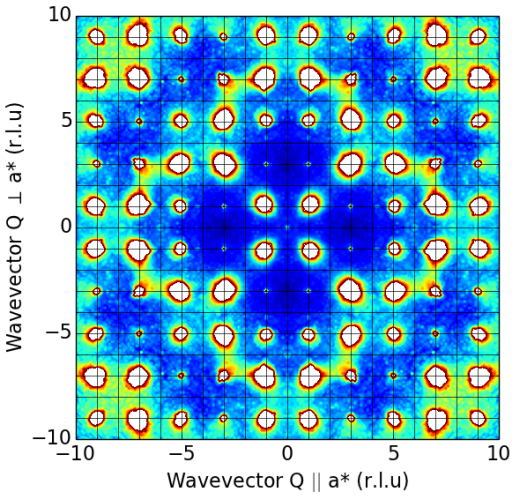

Figure 3.5: Stuffed $Yb_{2.5}Ti_{1.5}O_{6.75}$ in the $(hk7)$ plane. The presence of addtional diffuse scattering features around (5 5 7) relative to the other disordered sample indicates an alternative mode of disorder.

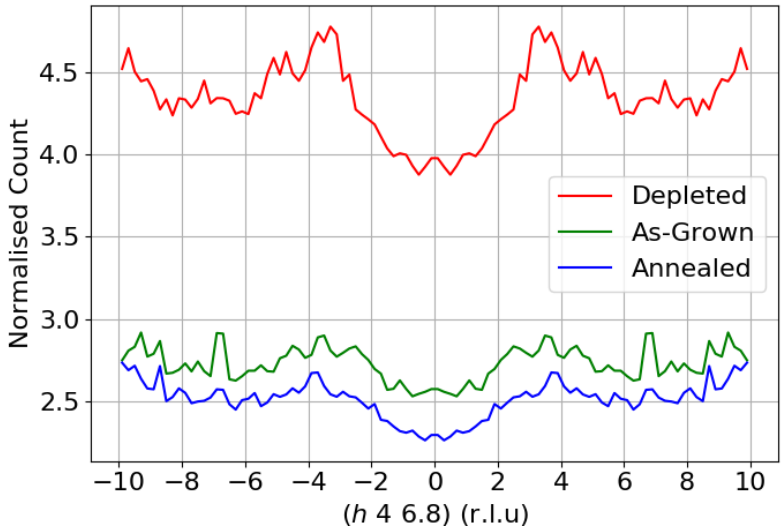

Figure 3.6: A cut across the (h 4 6.8) direction of annealed $Yb_2Ti_2O_7$. Evidently the broad features associated with diffuse scattering are reduced in the annealed sample suggesting that annealing in oxygen creates a largely defect free sample.

The concentration of excess Yb ions in the stuffed sample is quite high, $x \sim 0.4$, and it is worth considering whether the defects order to form superstructures. There is no evidence for the presence of sharp superlattice reflections at positions away from the pyrochlore reciprocal lattice. Lau et al. found that for a single crystal of stuffed $Ho_2(Ti_{1.33}Ho_{0.67})O_{6.67}$ grown by the floating zone method, superstructure peaks formed along both the $\langle 662 \rangle$ direction and the $\langle 111 \rangle$ direction as indicated in Fig. 3.7 (a) [156]. Figure 3.7 (b) shows the $Yb_{2+x}Ti_{2-x}O_{7-x/2}$ sample in the equivalent plane, (hhl), and shows the absence of any superstructure peaks. Furthermore all of the pyrochlore Bragg reflections are sharp, indicating long-range ordering of the pyrochlore structure, in contrast to quenched $Ho_2(Ti_{1.33}Ho_{0.67})O_{6.67}$ [156].

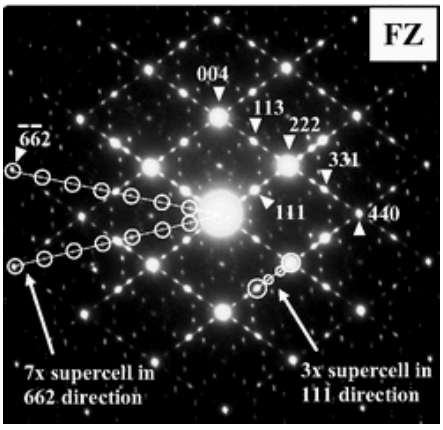

(a)

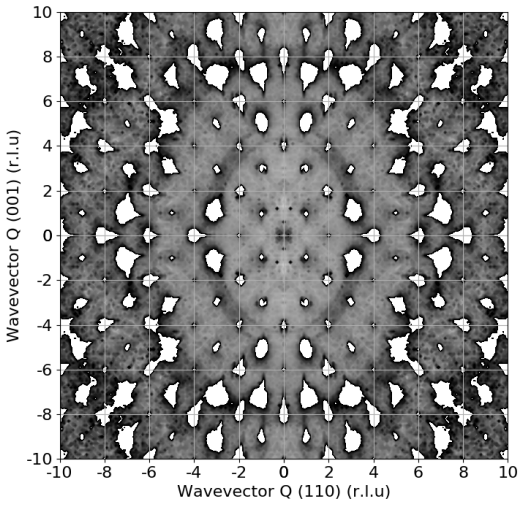

(b)

Figure 3.7: (a) Electron diffraction pattern of floating zone grown stuffed $Ho_2(Ti_{1.33}Ho_{0.67})O_{6.67}$ and (b) neutron diffraction pattern of $Yb_{2+x}Ti_{2-x}O_{7-x/2}$ shown in the (hhl) plane. $Ho_2(Ti_{1.33}Ho_{0.67})O_{6.67}$ shows superstructure peaks have formed along the $\langle 111 \rangle$ and $\langle 662 \rangle$ directions corresponding to a sevenfold enlargement of the unit cell which are absent in the $Yb_{2+x}Ti_{2-x}O_{7-x/2}$ sample. (a) is reproduced from Ref. [156].

3.3 Modelling of the diffuse scattering

The code used for the following work is a substantially extended version of the program written by G. Sala and M. Guttmann used in Ref. [91]. The program uses the Metropolis Monte Carlo algorithm [157] implemented for a system with point-like particles each with a charge and position connected by springs with an associated spring constant. The initial choice of spring constants and which types of atomic pairings were given springs were taken from Ref. [91] although additional spring constants were added for the stuffed sites with the relative strength of these chosen by seeing which had best agreement with the experimental data [158, 159] through a purely visual comparison. The spring pairings used were nearest neighbour Yb-O(1), Yb-O(2), Ti-O(2), O(2)-O(2), O(1)-O(2), Yb(Stuffed)-O(2). Springs were also included for those pairings listed previously but with an oxygen vacancy substituted for an oxygen ion where required.

Initially a stoichiometric system of 64×64×64 unit cells of $Yb_2Ti_2O_7$ is formed. For a system with isolated oxygen vacancies, Marsaglia random numbers are generated [160] which are used to select oxygen sites to vacate and then two nearest neighbour titanium sites have their charge changed from 4+ to 3+ for charge compensation. For a stuffed system the randomly selected nearest neighbour titanium ions are instead changed to Yb^{3+} ions. The vacancy sites are only different to an occupied oxygen site in that their associated scattering for calculating the resultant scattering length is set to zero and a different spring constant is associated with the site. Removing the associated spring constant may seem like an intuitive step but it leads to lattice instabilities and prevents the system from converging on a stable state. While the ions in the system are considered as point charges this is not an entirely successful approximation as this does not allow for distortions to the lattice arising from the introduction of vacancies. To account for this, a size effect is introduced [159]. What this means in practice is that in the function calculating the energy of each nearest neighbour pairing in the system,

a value is added that biases the calculated energy towards a state where the ions near vacancy sites move along the vector formed by the ion and the nearest vacancy. The numerical value of the size effect is obtained by manually varying it until the scattering features observed in the data are reproduced [161, 162, 163]. The system is then relaxed, with the size effect and thermal fluctuations perturbing the system via the Monte Carlo algorithm whereby the shift in each atom's placement is determined by a vector taken from a Gaussian distribution [158]. The new energy of the system is calculated as Hook energies which are summed and the new system is accepted or rejected using the Metropolis algorithm [157]. The main differences in the types of models used here are whether or not stuffing is included and if the vacancies in a system form on the O(1) or O(2) sites, which also results in different size effects being used.

For an O(1) vacancy model there are two size effects considered. One is the movement along the vector of O(2) ions and Ti^{4+} ions. The second is between Yb ions and O(1) ions. The Yb size effect is used when there is a vacancy site adjacent to a Yb ion. In this case the energy of the system is biased such that Yb ions shift along the $\langle 111 \rangle$ vector connecting the two ions. This additionally results in a shift in the next O(1) ion sitting along this vector. The direction of this shift is manually selected by the sign of the size effect which is adjusted according to its agreement with the data. These size effects are illustrated in Fig. 3.8.

For an O(2) vacancy the fact that Ti^{3+} ions are still present means that the size effect associated with the movement of O(2) from Ti^{3+} to Ti^{4+} is still considered, but the Yb-O(1) size effect is no longer relevant. Instead a size effect between the O(2) vacancy site and its nearest neighbour titanium is introduced. In this model the Ti^{3+} ions are located on the two nearest neighbour titanium sites. This biases the system such that a shift along the vector connecting these two sites is more favourable. This has the additional effect of moving the O(2) ion that is beyond the Ti site along this direction

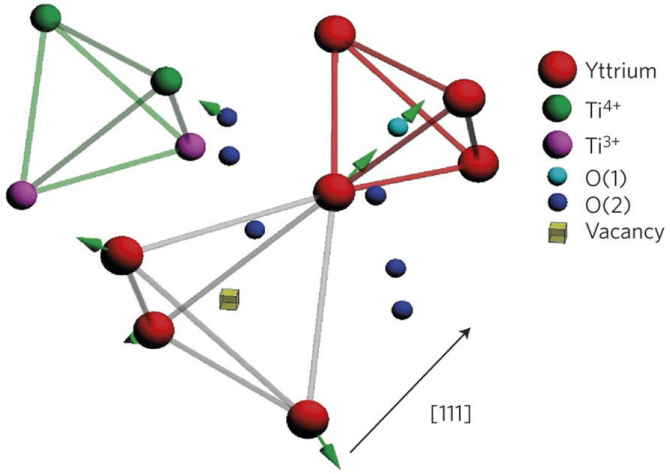

Figure 3.8: Schematic of the ionic displacements resulting from the size effects associated with an O(1) vacancy. Removing an O(1) atom causes the nearest neighbour rare earth cation to move with a corresponding move from the nearest neighbour O(1) anion along the ⟨111⟩ direction. There is also movement by the O(2) ions towards the adjacent Ti^{4+} ions. Figure reproduced from Ref. [91].

as illustrated in Fig. 3.9. As in the case of the size effects used in the O(1) vacancy system the sign (towards or away from a vacancy) and magnitude of these displacements is altered by changing the sign and magnitude of the size effect parameter.

3.3.1 Isolated Vacancies

In Fig. 3.10 the diffuse neutron scattering from oxygen-depleted $Yb_2Ti_2O_{7-\delta}$ measured in the $(hk7)$ plane is compared with Monte Carlo calculations. The model with oxygen vacancies on the O(2) sites (b) has better agreement with the data (a) than the model with vacancies on the O(1) site shown in panels (c) and (d). The experimental data for the $Yb_2Ti_2O_{7-\delta}$ shown in panel (a) looks very different to the corresponding experimental data set for $Y_2Ti_2O_{7-\delta}$. The characteristic arcs and crosses are replaced by diffuse

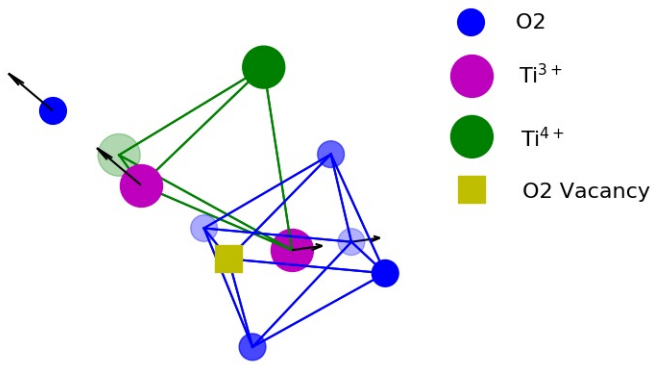

Figure 3.9: Schematic of displacements resulting from the size effects associated with O(2) vacancies. Ti^{4+} are shifted along the vector connecting them to O(2) vacancies. The O(2)-Ti^{4+} size effect shown in Fig. 3.8 is still active in this model.

scattering beyond (337). Fig. 3.10 (c) shows the scattering calculated with exactly the same O(1) vacancy model as for $Y_2Ti_2O_7$ [91] (i.e. the same displacements) but with the neutron scattering length of ytterbium rather than yttrium. This model retains arcs and crosses in disagreement with the data. Fig. 3.10 (d) shows the best agreement obtained with an O(1) vacancy model with different displacements, but the agreement with the data is still poor. It is only possible to reproduce the diffuse scattering beyond (337) when O(2) vacancies are introduced, and Fig. 9 (b) shows the calculated scattering from the optimal model. The model does not reproduce the weak feature between (557) and (777) but, given the simplicity of the model, the overall agreement with the data is very good.

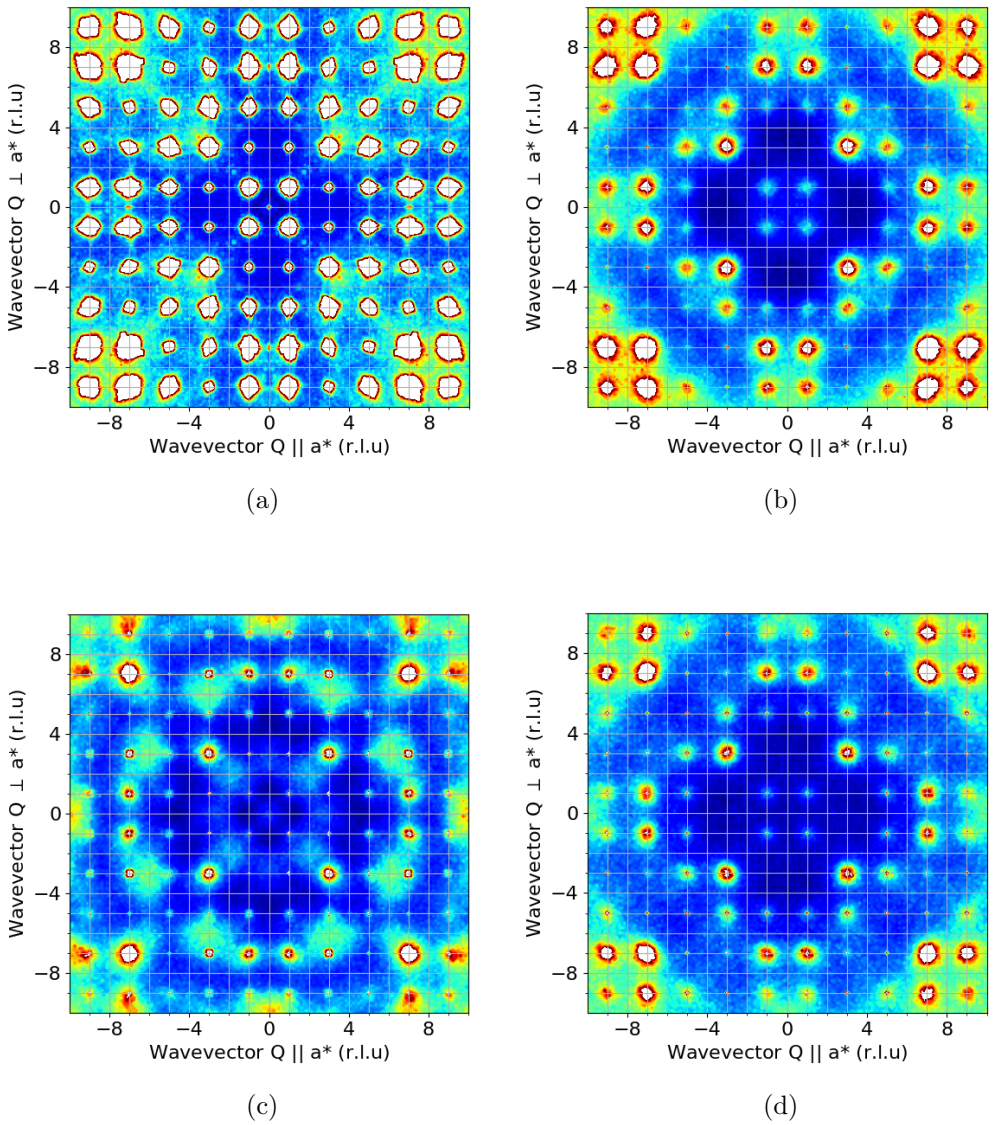

Figure 3.10: A comparison of (a) experimentally measured $Yb_2Ti_2O_7$ taken at $T = 30$ K, (b) a calculation with O(2) vacancies, (c) a calculation with the parameters used in Sala et al. [91] but with the Yb scattering length used in place of Y, and (d) a calculation with O(1) vacancies. All plots show the $(hk7)$ plane.

In the O(2) vacancy model the largest displacements are of the nearest neighbour Ti^{3+} ions and the O(2) ion along the same vector, see Fig. 3.9. The distribution of distances of these ions from the O(2) vacancy site shown in Fig. 3.15, and the centres are shifted by 0.003 and 0.012 l.u respectively from the stoichiometric values.

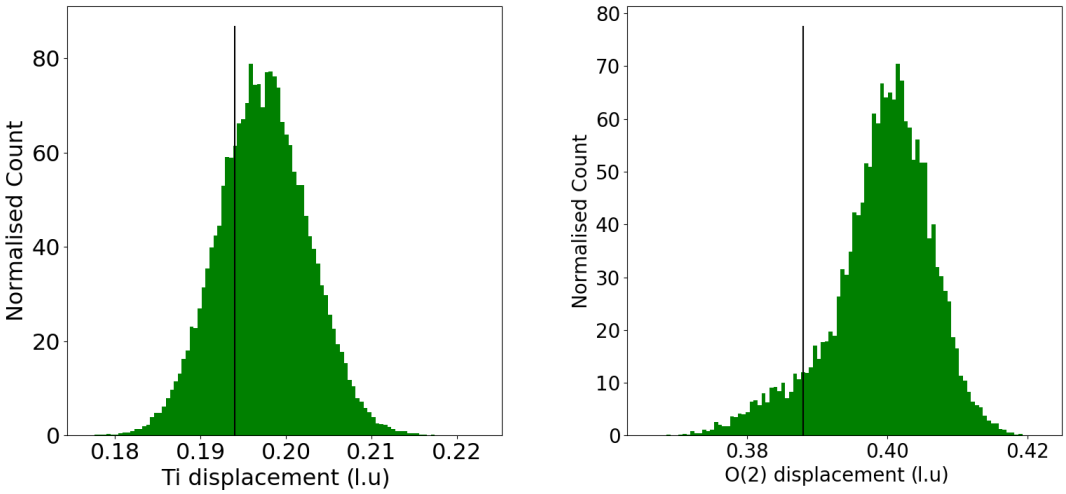

(a) (b)

Figure 3.11: Ionic displacements in depleted $Yb_2Ti_2O_7$. Ti^{3+} ions are displaced away from the vacancy site with a corresponding second order displacement of O(2) ions. (a) The distribution of displacements of Ti^{3+} from vacancy sites with a displacement distribution centred on a shift of 0.003 l.u. (b) The distribution of displacements of O(2) ions from vacancy sites with a displacement distribution centred on a shift of 0.012 l.u. The black lines represent the stoichiometric ionic separation.

The O(2) vacancy model was found to be robust in reproducing the majority of major diffuse scattering features across reciprocal space. Additional reciprocal space planes are shown in Fig. 3.12. Fig. 3.13 shows the result of varying the Ti size effect for the same values of the spring constants and the same oxygen size effect. Whilst

there are small differences between the calculations throughout reciprocal space the main differences in the ($hk7$) plane are beyond the (337) position where the diffuse scattering in the experimental data is especially strong. Increasing the Ti size effect causes this intensity to increase up to a certain value as shown in panel (d) where the system becomes unstable and anomalous shaped scattering features appear, and the distribution of Ti-vacancies distances shows a double peak in the distribution. A negative size effect does not give scattering immediately beyond (337).

Hence, the presence of diffuse scattering beyond (337) and the absence of the characteristic arcs and crosses in the ($hk7$) plane favours O(2) over O(1) vacancies. Further evidence that the defects in $Yb_2Ti_2O_{7-\delta}$ are different to $Y_2Ti_2O_{7-\delta}$ is the fact that oxygen depletion does not lead to an increase in lattice parameter, see table 3.1. In the case of $Y_2Ti_2O_7$ the increase in the lattice parameter was associated with the expansion of the Y tetrahedra around O(1) vacancies, and this is a clear indication than the defect structure of $Yb_2Ti_2O_{7-\delta}$ is different. Furthermore, the displacements in the proposed O(2) defect model are physically reasonable. The displacements from Fig. 3.15 give an average bond length between Ti^{3+}-O(2) $\approx$ 2.03 Å for $Yb_2Ti_2O_{7-\delta}$ which is very similar to the corresponding values reported for $Y_2Ti_2O_{7-\delta}$ (2.03 Å) [91] and for Ti_2O_3 (2.04 Å) [164]. Finally, a powder neutron diffraction study of $Yb_2Ti_2O_7$ reduced at low temperatures in a topotactic reaction with CaH_2 also finds O(2) vacancies [93].

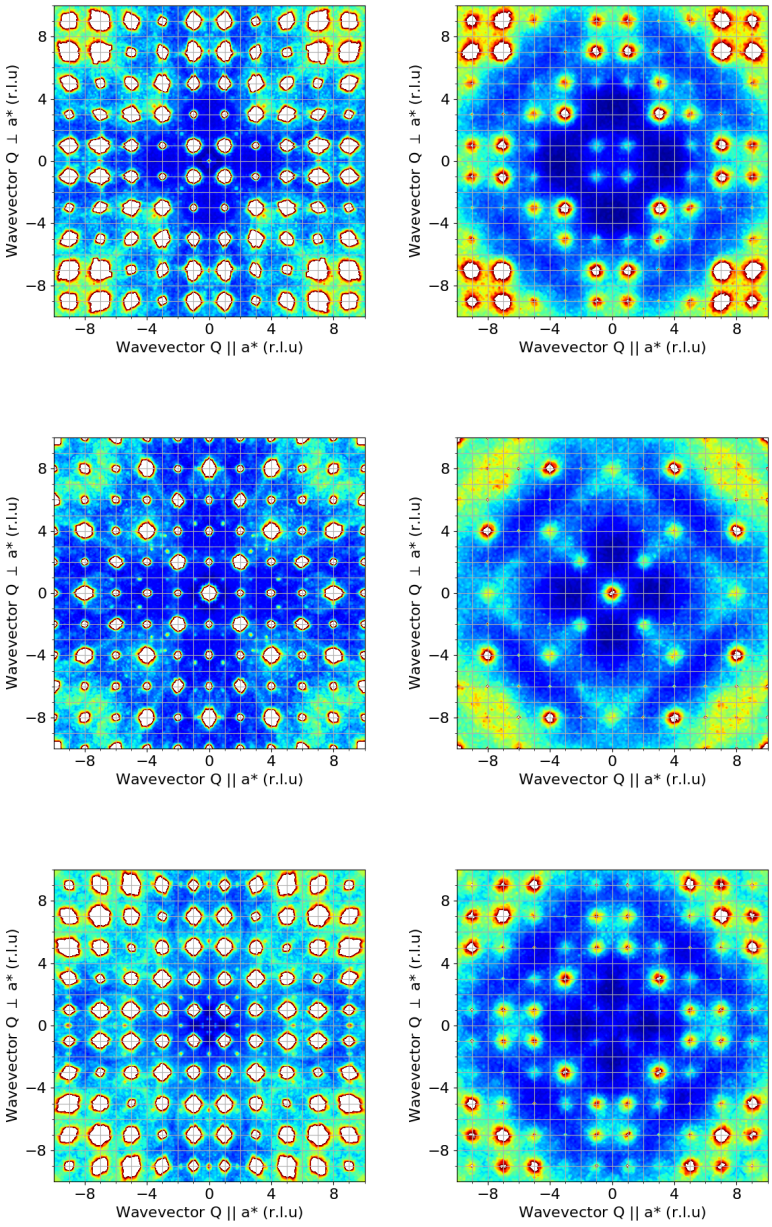

Figure 3.12: A comparison of experimentally acquired scattering pattern (left) with calculation with O(2) vacancies (right). Planes shown, from top to bottom: ($hk7$), ($hk8$) and ($hk9$). Diffuse scattering is shown in the same positions for both experimental data and model indicating the validity of the calculation.

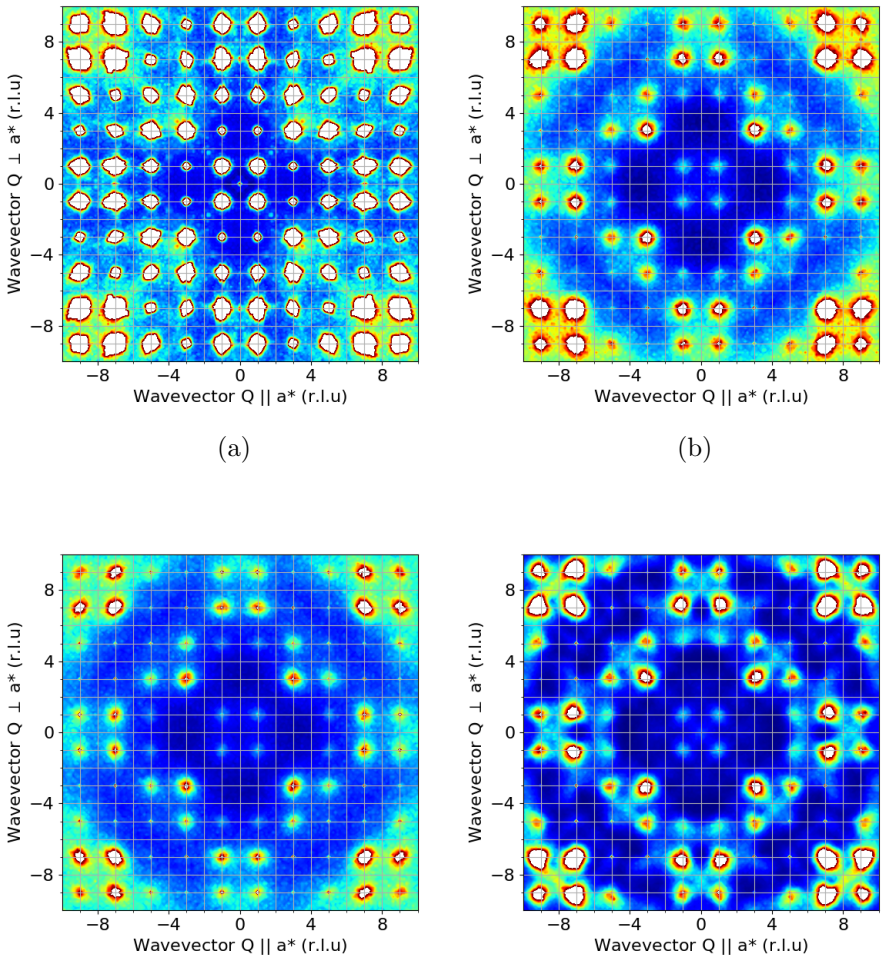

Figure 3.13: A comparison of (a) experimentally measured $Yb_2Ti_2O_7$, (b) a calculation with the value that gives the best agreement across reciprocal space, (c) a calculation with a negative size effect (d) a calculation with a large positive size effect. All plots show the $(hk7)$ plane.

3.3.2 Stuffing

The diffuse scattering in the $(hk7)$ plane for the stuffed $Yb_{2+x}Ti_{2-x}O_{7-x/2}$ sample is compared with calculations using the balls and springs model in Fig. 3.14. The presence of Yb^{3+} ions on titanium sites might be expected to result in charge-compensating vacancies on the neighbouring O(2) sites. A comparison of the data in Fig. 3.14 (a) with the data in in Fig. 3.10 (a) suggests that the details of the model must be different, since the diffuse scattering intensity beyond (337) is replaced by arcs of scattering reminiscent of $Y_2Ti_2O_7$. Replacing Ti^{3+} by Yb^{3+} is not enough to overcome this problem. However, if the sign of the Ti^{3+}-Yb^{3+} size effect is reversed, the agreement between the calculation in (b) and the data in (a) is much better. The only significant discrepancy between the model and the data is the scattering near (397). In this calculation it is assumed that the two nearest neighbours sites next to the O(2) vacancy are occupied by Yb^{3+} ions and, given the simplicity of the model, the agreement between the calculations and the data is remarkable. Taking the O(1) vacancy model applied to $Y_2Ti_2O_7$ and modified to include stuffing, the calculated scattering in Fig. 3.14 (c) still includes crosses that are absent in the data. Allowing the ions to relax to their optimum positions for an O(1) vacancy model (d) removes the crosses and gives much better agreement with the data. However, the O(1) model has additional features that are not present in the experimental data. Most notably the diffuse scattering beyond the (337) and between the (917) and $(9\bar{1}7)$ peaks is entirely absent in the experimental data.

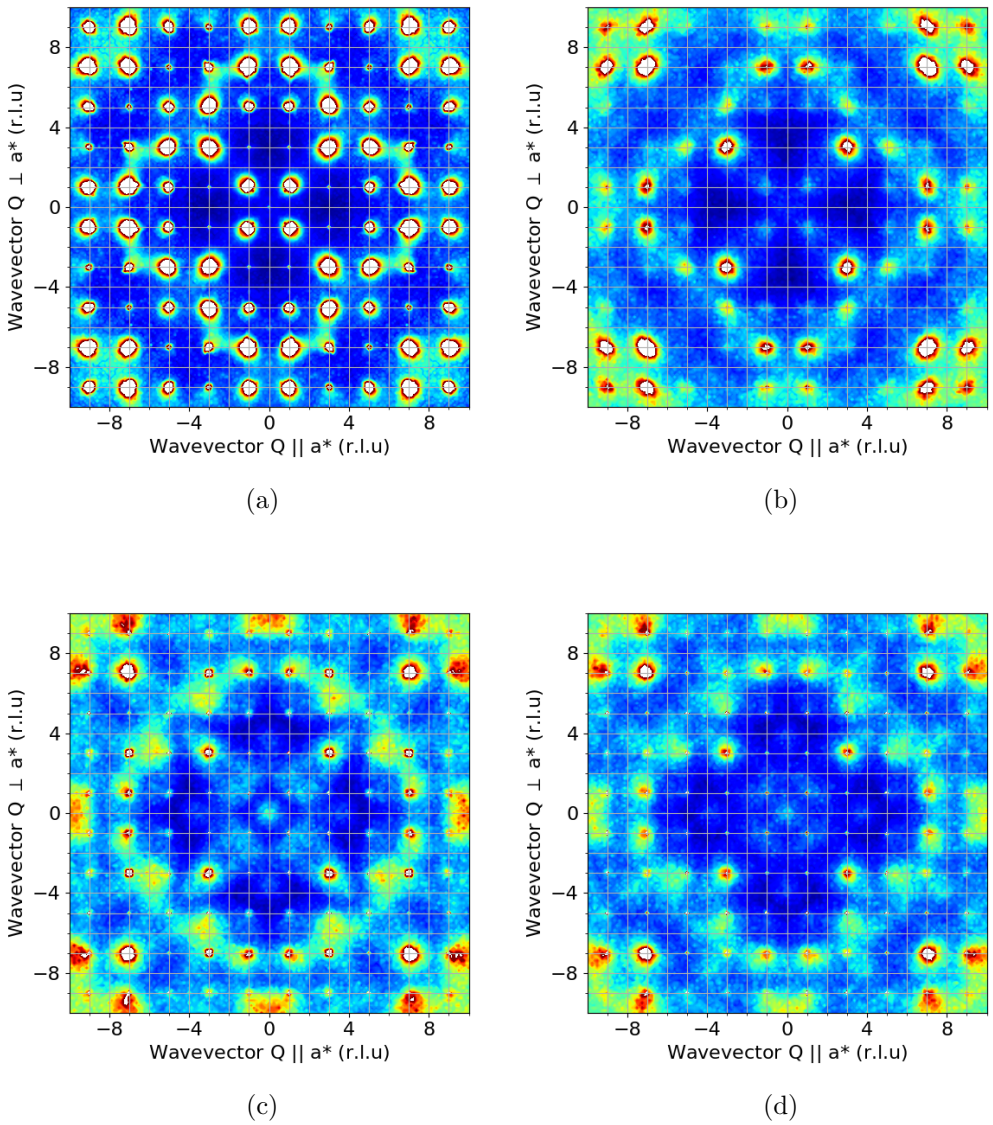

Figure 3.14: A comparison of (a) experimentally measured $Yb_{2.5}Ti_{1.5}O_{6.75}$, (b) a calculation with O(2) vacancies, (c) a calculation with the parameters used in [91] but with the Yb scattering length used and (d) a calculation with O(1) vacancies. All plots show the $(hk7)$ plane.

As with the oxygen-depleted sample the parameter that had the biggest impact on the resulting scattering was the Ti^{3+} size effect but unlike the depleted sample the resulting ionic displacement was a contraction of the environment around the vacancy with a negative size effect used. For this value the average shift by the Yb ions towards the vacancy was 0.0133 l.u with a corresponding average movement by the O ions beyond the Ti sites towards the vacancy of 0.002 l.u. The fact that the Yb^{3+} ions are displaced away from the neighbouring ions towards the vacancy is reasonable, since Yb^{3+} has a larger ionic radius than Ti^{3+}. The O(2) model for the stuffed system showed excellent agreement throughout reciprocal space. A number of comparisons between the model and the experimentally acquired data are presented in Fig. 3.16 showing good agreement between the two. The stuffed model is particularly sensitive to changes in the Yb size effect. Fig. 3.17 shows plots for variations in the Yb size effect which exhibits major changes in the qualitative features of the diffuse scattering. For this system there is an unambiguous decrease in agreement between data and model for positive values of the Yb size effect. A zero value still shows some agreement but with some additional diffuse scattering which transitions to having almost no similarity for a positive value. Increasing the magnitude of the negative size effect much beyond the value used in the model with best agreement with the data gives additional scattering at low Q along with much broader features than those present in the experimental data.

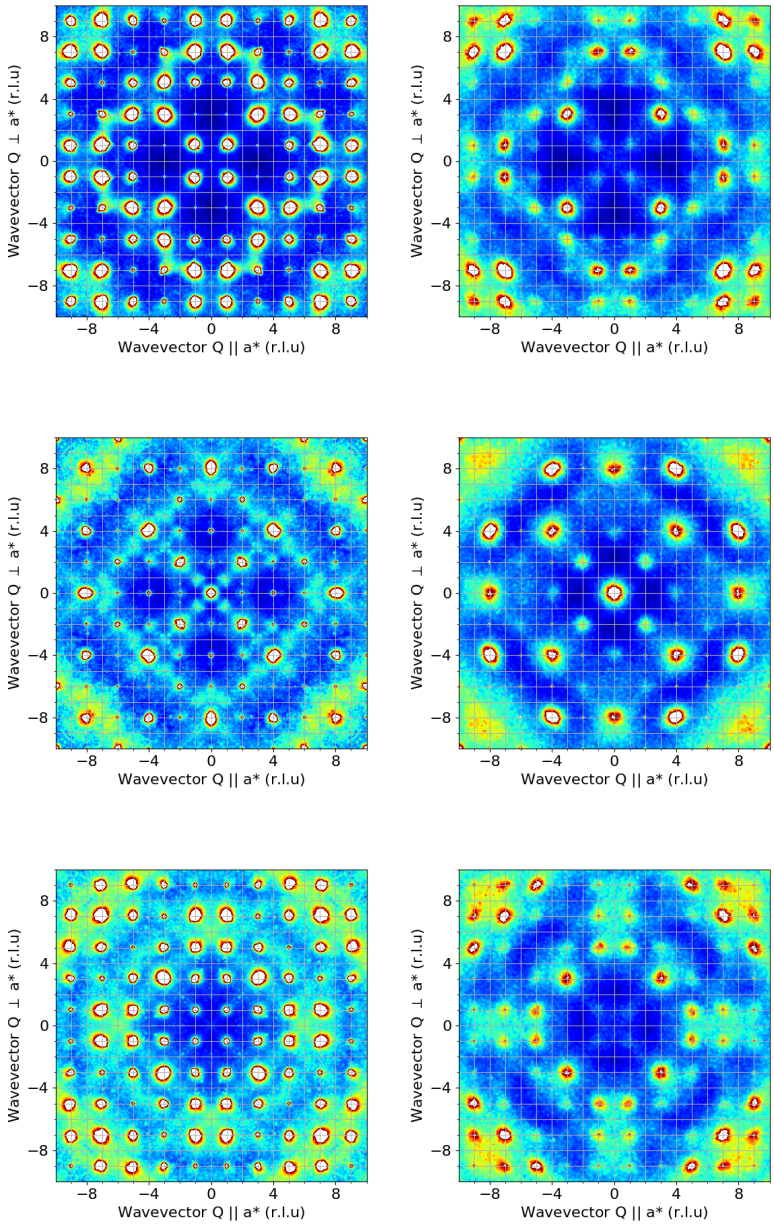

Figure 3.16: A comparison of the experimentally acquired scattering pattern of $Yb_{2+x}Ti_{2-x}O_{7-x/2}$ (left) with calculation with O(2) vacancies (right). Planes shown, from top to bottom: ($hk7$), ($hk8$) and ($hk9$). Diffuse scattering is shown in the same positions for both experimental data and model indicating the validity of the calculation.

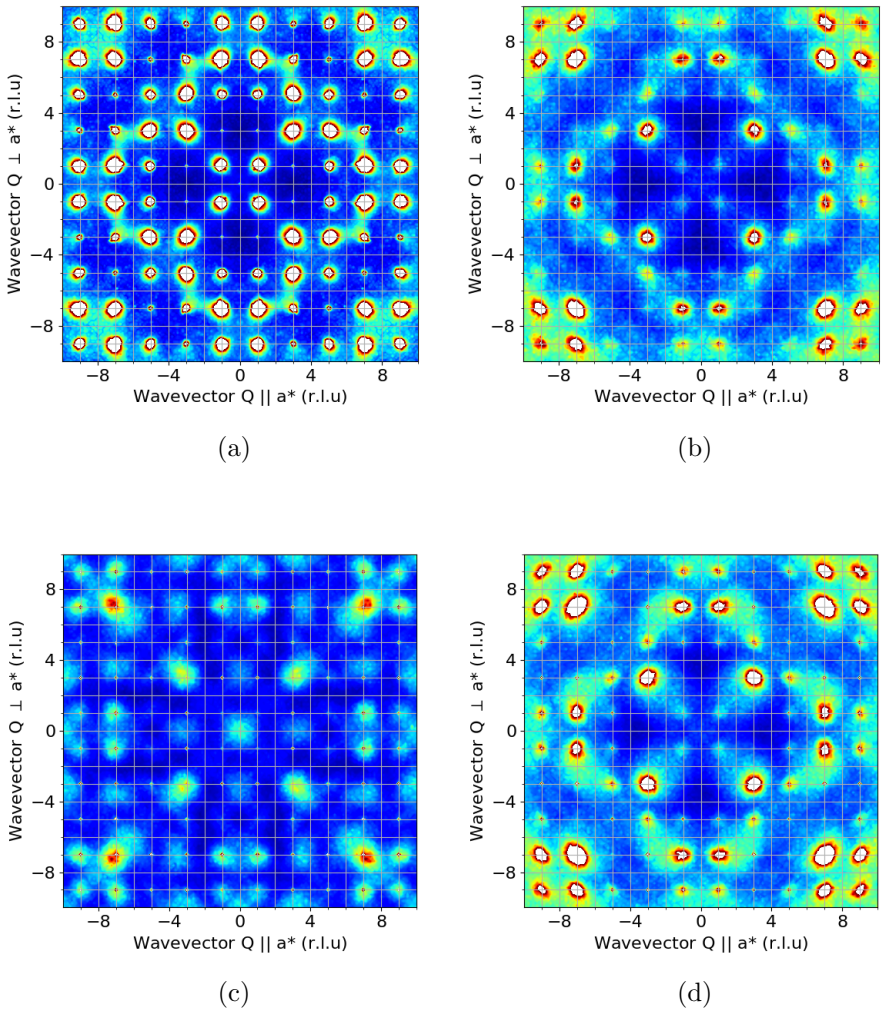

Figure 3.17: A comparison of (a) experimentally measured $Yb_{2+x}Ti_{2-x}O_{7-x/2}$, (b) a calculation with a small negative value that gives the best agreement across reciprocal space, (c) a calculation with a positive size effect (d) a calculation with a large negative size effect. All plots show the $(hk7)$ plane. Clearly deviating from a small negative value causes the agreement with the experimental data to diminish.

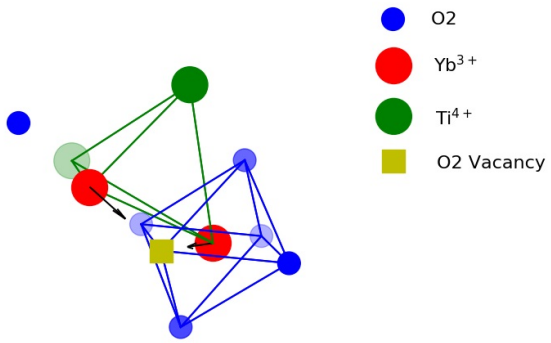

(a)

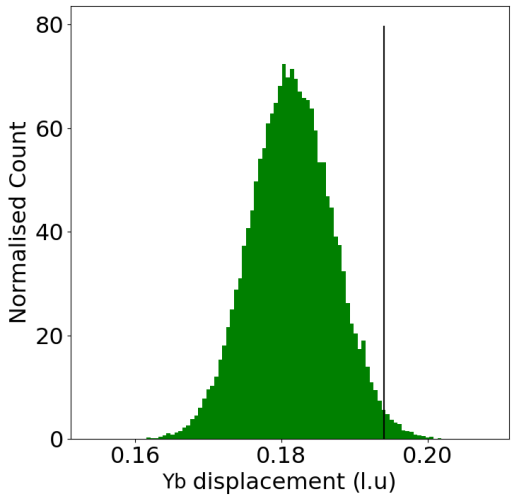

(b)

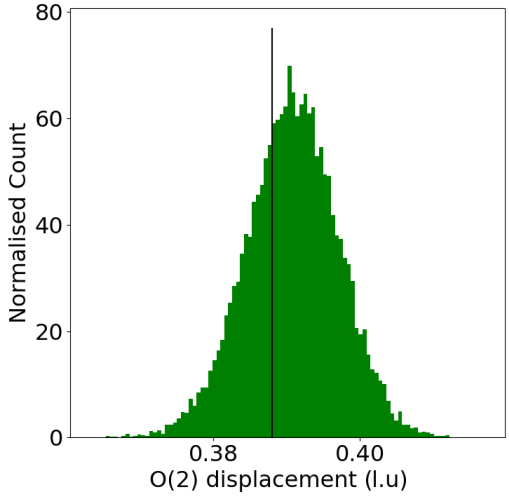

(c)

Figure 3.15: Ionic displacements in $Yb_{2+x}Ti_{2-x}O_{7-x/2}$. (a) Schematic of Yb^{3+} ions displaced towards the vacancy site. (b) The distribution of displacements of Yb^{3+} from vacancy sites with a displacement distribution centred on a shift of 0.0133 l.u. (c) The distribution of displacements of O(2) from vacancy sites with a displacement distribution centred on a shift of 0.002 l.u. The black lines represent the stoichiometric ionic separation.

Chapter 4

Magnetic Ordering in $Yb_2Ti_2O_7$

4.1 Introduction

Early studies suggested that magnetic ordering is completely suppressed in $Yb_2Ti_2O_7$ down to the lowest attainable temperatures [108]. Recent studies continue to report that the quantum spin liquid state persists in stoichiometric samples [98]. However, there is now a substantial body of work that shows that ferromagnetic ordering occurs below T $\sim$ 400 mK. Yasui et al. reported single crystal neutron scattering data that could be explained by a collinear ferromagnet [114]. Gaudet et al proposed a 2-in 2-out splayed ferromagnetic model [133], and this is supported in a recent study be Scheie et al. [165]. Finally, Yaouanc et al. have concluded from powder neutron diffraction studies of another sample that the ground state is an all-in all-out splayed ferromagnet [121].

4.2 Experimental Method

The structures of the samples studied here were previously determined by neutron diffuse scattering on SXD and the results of the structural characterisation as described in Chapter 3. In this chapter the experiments were carried out on the D7 diffuse scattering diffractometer at the Institut Laue-Langevin in Grenoble with the objective being to measure the magnetic diffuse scattering from the samples and use this information to make inferences about the magnetic correlations present in varying stoichiometric configurations of $Yb_2Ti_2O_7$. The measurement protocol was as follows. The samples were attached to a copper plate using copper wires in order to maximise thermal conductivity at millikelvin temperatures. The single crystals were mounted so that the $(00l)$ surface plane was perpendicular to the plane of the copper plate. The orientation of the single crystal and the mounting plate were then adjusted on Orient Express so that the (hhl) crystallographic plane coincided with the horizontal scattering plane. The sample was then mounted in a dilution refrigerator with a cryomagnet with a maximum vertical magnetic field of B = 2.5 T. The detector bank comprised 132 detectors covering the range of scattering angles from 0 to 132°. In each case an additional set of measurements were performed with each detector bank offset by 4.5° in order to fill the gaps between the detectors. The sample was rotated about a vertical axis in steps of 1° over a range of 360°. In this way it was possible to map out the scattering throughout the (hhl) plane up to a maximum $|Q| \sim 1.3$ Å^{-1}. The samples were measured for 40 s in each the spin-flip and non spin-flip channel unless explicitly stated otherwise.

A pyrolytic graphite monochromator was used to select cold neutrons at a wavelength of $\lambda \sim 4.8$ Å^{-1} with a beryllium filter employed to suppress higher harmonics. The sample was mounted on a copper plate such that the $(00l)$ axis was perpendicular to the plate with the $(hh0)$ axis also in the scattering plane. Uniaxial polarisation was used to separate the magnetic and structural correlations. This plane of polarisation

was orthogonal to the scattering plane, corresponding to the [1-10] direction. A polarising super mirror and a Mezei flipper were employed to create the spin polarised beam of neutrons. The scattered neutrons were analysed using polarising benders in front of the helium detectors.

The data presented in this chapter were obtained in two separate visits to the ILL. In the first experiment the stuffed sample and the as-grown sample were measured. Between experiments the as-grown sample was annealed in oxygen and the changes to its structure are described in Chapter 3. In the second visit to the ILL the magnetic correlations were measured on the oxygen-annealed and oxygen-depleted single crystal sample.

During the second visit the copper plate used to mount the sample was sufficiently thick ($\sim$2 mm) to leave a clearly visible absorption signature in the data. This leads to a characteristic zig-zag pattern of dark regions in a plot of 2θ against ω in Fig. 4.1.

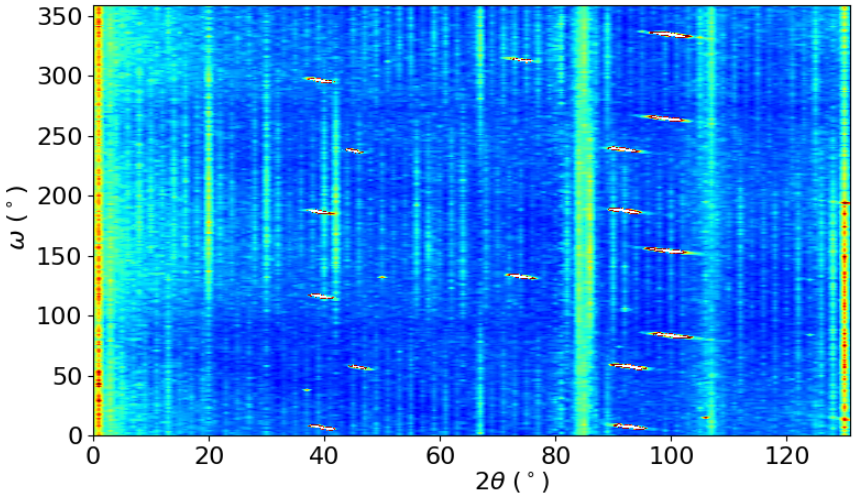

Figure 4.1: Figure showing scattering intensity as a function of scattering angle (2θ) and sample rotation (ω) for the oxygen-annealed sample at $T \sim 60$ mK. Sharp single-crystal Bragg reflections and powder lines (the vertical lines) are visible in the data. In addition a characteristic zig-zag pattern of lower intensity (dark blue lines) is apparent in the data and this is a signature of absorption from the flat plate.

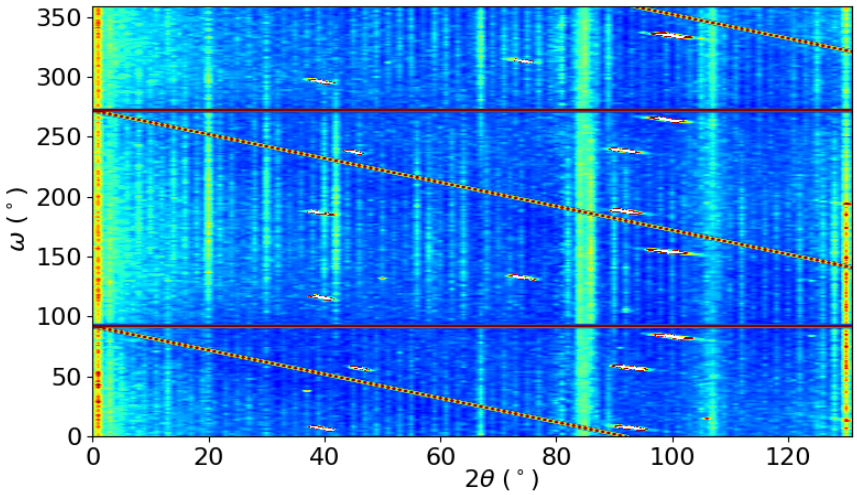

Figure 4.2: Same plot as Fig. 4.1 but with lines of grazing incidence (red) and grazing exit (orange) overlaid.

At values of omega close to grazing incidence the copper plate absorbs incident neutrons and reduces the scattering in all of the detectors. This results in two horizontal regions of low intensity separated by $\omega = 180°$. The copper plate only absorbs a substantial fraction of neutrons in the scattered beam when the plane of the plate is pointing towards the detector. This is known as grazing exit, and it results in regions of low intensity when omega is equal to two-theta. These are visible in the dark blue regions in figure 4.1 and the overlaid lines in figure 4.2.

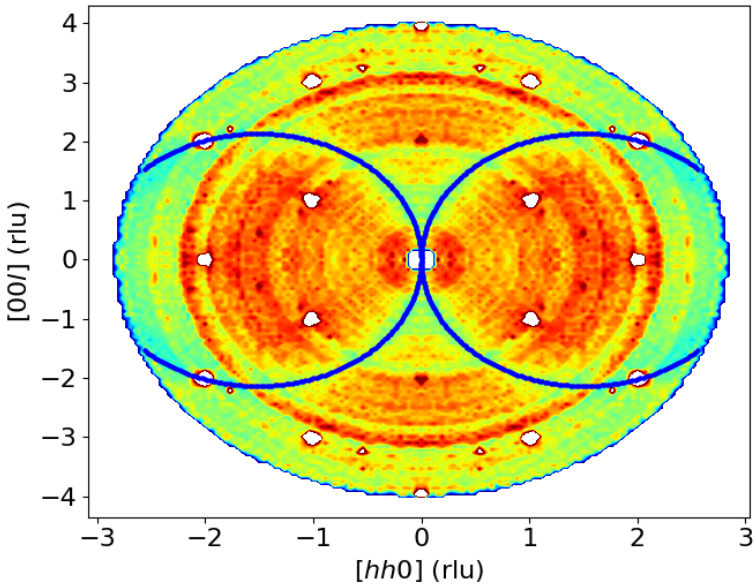

Figure 4.3: Figure showing the total scattering of oxygen annealed $Yb_2Ti_2O_7$ with an overlay indicating the absorption. The blue lines correspond to the lines of grazing incidence and grazing exit. As is the case in all subsequent plots of the scattering in the (hhl) plane, the data have been symmetrised with respect to the space group in order to improve counting statistics.

Mapping these points onto a reciprocal space plot corresponding to the sample geometry shows the effect of this absorption on the resultant scattering pattern. Figure 4.3 shows these points overlaid onto a plot of the total scattering of oxygen annealed $Yb_2Ti_2O_7$. Fortunately it can be seen that the absorption features are far away from the magnetic scattering features of interest in this study and do little to impede interpretation of the data.

4.3 Experimental Results

4.3.1 As-Grown $Yb_2Ti_2O_7$

A sample of as-grown $Yb_2Ti_2O_7$ previously characterised on SXD was mounted on D7 at ILL having being aligned such that the scattering plane was across the (hhl) plane following alignment on Orient Express also at ILL. The sample was initially cooled to $T \sim 60$ mK, well below the previously measured transition temperature of the $Yb_2Ti_2O_7$ ground state [104, 111, 113, 118, 121, 122, 123, 124, 125, 126] and a guide field of 0.01 T was applied. Figure 4.4 shows rods of scattering along [111] in the spin-flip channel indicating the presence of two-dimensional correlations along with a broad area of scattering centred on (220). While it appears near the edge of the intensity there is a small but clear region of diffuse scattering around (004). The non spin-flip channel also shows scattering along [111] but also with rods connecting the (113) peaks and the (222) peaks.

A 2.5 T field was applied perpendicular to the scattering plane at base temperature with the intention of creating a single domain ferromagnet to allow for a comparison with the low field scattering. Measurements were taken for 54 s in both spin-flip and non spin-flip channels. Unfortunately the strong force from the high magnetic field resulted in the misalignment of the sample. There was insufficient time before the end of the beam time to remount the sample in the dilution refrigerator. In order to complete the experiment the sample was cooled to $T \sim 1.5$ K and a field was applied perpendicular to the scattering plane.

Figure 4.5 shows the scattering in a field in the (hhl) plane. The scattering in the spin-flip channel is almost entirely removed with some small remnant of the original scattering still visible along [111] and at (220) indicating the near total suppression of short-range correlations in the sample. The non spin-flip channel shows a near complete

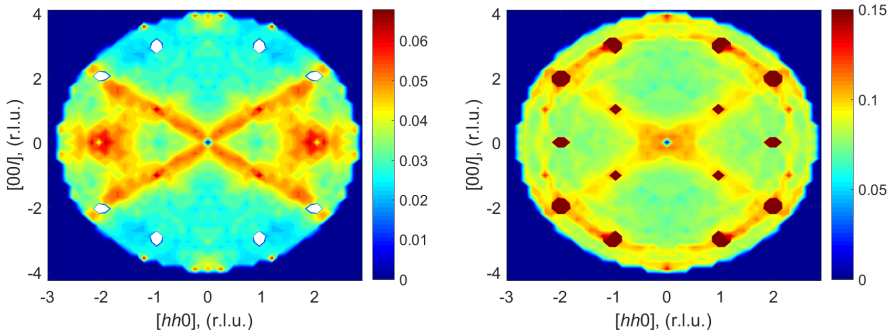

(a) (b)

Figure 4.4: Diffuse scattering of polarised neutrons from as-grown $Yb_2Ti_2O_7$ in the (hhl) plane measured at base temperature, $T\sim$ 60 mK. (a) Spin-flip channel and (b) the non spin-flip channel. All of the features visible in the spin-flip channel of the subsequent figures are magnetic whereas for the non spin-flip channel, in addition to magnetic scattering, structural Bragg peaks and powder rings are also visible. The spin flip channel clearly shows rod-like scattering along the [111] directions and also broad scattering near the (220) position. The non spin-flip channel exhibits [111] rods but also intensity connecting the (113) peaks to the (222) peaks.

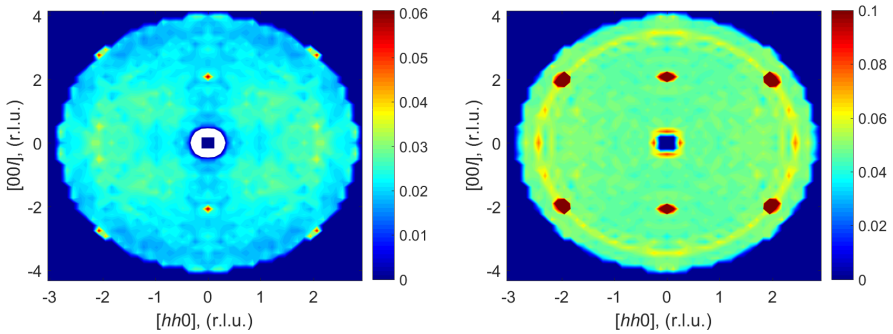

(a) (b)

Figure 4.5: Polarised diffuse neutron scattering of as-grown $Yb_2Ti_2O_7$ taken at $T \sim 1.5$ K with an applied field of 2.5 T on D7 (a) in the spin-flip channel and (b) in the non spin-flip channel. The scattering exhibited at zero field is almost entirely suppressed in both channels.

removal of diffuse scattering.

The field was removed with measurements taken again at $T \sim 1.5$ K (Fig. 4.6) and then at $T \sim 5$ K (Fig. 4.7) with 40 s counts in both channels in each instance and a guide field of 0.01 T applied. The same features seen at base temperature persist at each temperature albeit with a substantial reduction in intensity. This indicates that even as high as $T \sim 5$ K there is a persistent if reduced presence of the short range correlations in the system. Fig. 4.8 shows a one-dimensional cut across the spin flip channel. There is a dramatic decrease in scattering intensity across both diffuse features found at (111) and (220) with increasing temperature indicating the suppression of short range ordering.

Figure 4.9 shows a cut across [hh 3-1.5h] which goes across both the [111] diffuse scattering and into the diffuse scattering around (220) while avoiding the (111) Bragg peak. The base temperature measurement clearly shows the greatest levels of diffuse scattering while all the other measurements show substantial suppression of the diffuse

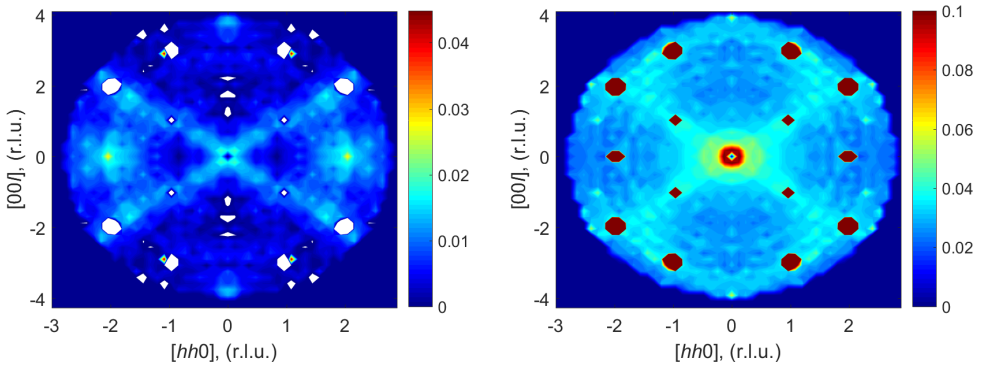

(a) (b)

Figure 4.6: Polarised diffuse neutron scattering of as-grown $Yb_2Ti_2O_7$ taken at $T \sim 1.5$ K. The scattering present at base temperature is substantially weakened in both (a) in the spin-flip channel and (b) in the non spin-flip channel.

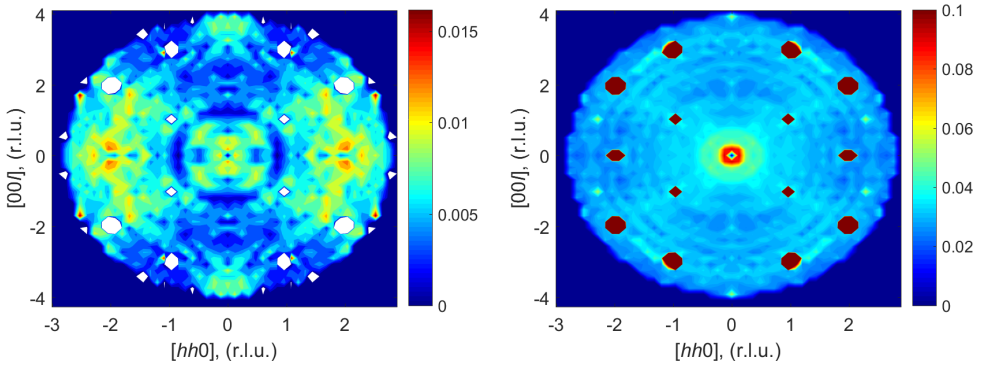

(a) (b)

Figure 4.7: Polarised diffuse neutron scattering of as-grown $Yb_2Ti_2O_7$ taken at $T \sim 5$ K. The scattering present at base temperature is nearly eliminated in both (a) in the spin-flip channel and (b) in the non spin-flip channel.

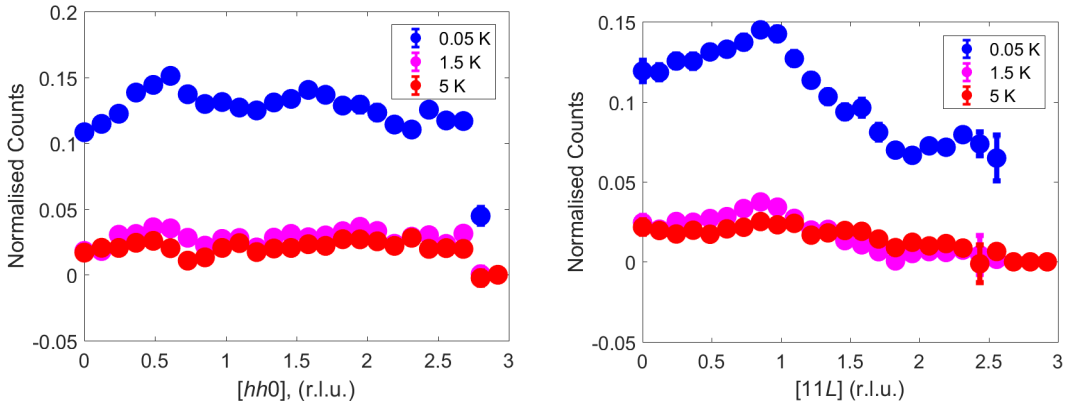

(a) (b)

Figure 4.8: Measurements at a range of temperatures across the (a) $[hh0]$ and (b) $[11l]$ direction in as-grown $Yb_2Ti_2O_7$ in the spin-flip channel. There is a substantial reduction in scattering intensity with increasing temperature across both the rod feature at (111) and the region around (220).

scattering. The measurements at intermediate temperatures show significantly reduced intensity, but with small increases above background when crossing the [111] ridge at h = 1.2, and in the broad region near h = 2. The measurements in a B = 2.5 T field have a reduced intensity compared to measurements are $T \sim 59$ mK, but higher than at 1.5 K. The increase is probably a background correction error due to the lack of background data specific to this particular field. However the fact that this scattering is flat shows that there is no diffuse scattering in the field.

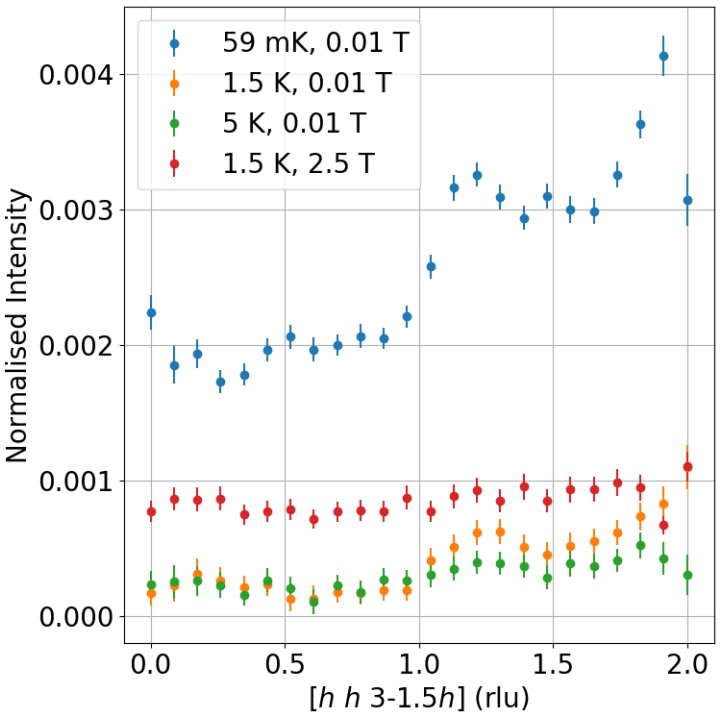

Figure 4.9: As-grown $Yb_2Ti_2O_7$ measurements at a range of temperatures and fields taken across [h h 3-1.5h]. At $T \sim 59$ mK the strongest diffuse scattering features are observed.

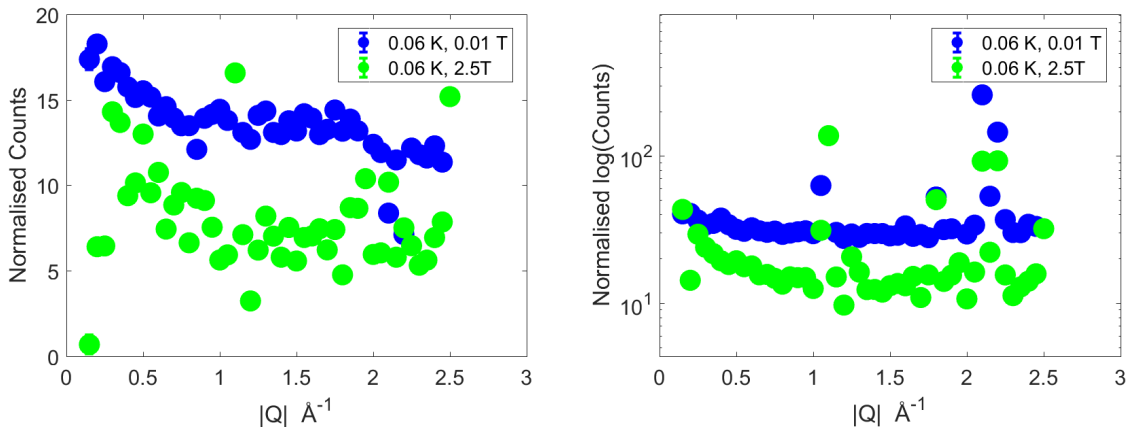

(a) (b)

Figure 4.10: As-grown $Yb_2Ti_2O_7$ $|\mathbf{Q}|$ dependence with field in (a) the spin-flip channel and (b) the non spin-flip channel. The application of a field leads to the reduction in diffuse magnetic scattering intensity indicating the suppression of short-range order in the system. One would not expect the presence of Bragg peak like features in (b) suggesting the potential for a small degree of misalignment.

Figure 4.10 (a) shows the variation of the count with $|\mathbf{Q}|$ in the spin-flip channel for both high and low field measurements. It is evident that the $T \sim 59$ mK and low field measurement have an intensity that decreases with $|\mathbf{Q}|$ that is consistent with what may be expected from a magnetic form factor. The decrease in intensity at 2.5 T suggests the removal of diffuse magnetic scattering by the field. In the high field measurement there are anomalous points resembling Bragg peaks. These peaks are also present in the non spin-flip channel shown in Fig. 4.10 (b) which means that there was likely a small amount of misalignment introduced upon application of field which introduced structural Bragg peaks.

4.3.2 Oxygen-Annealed $Yb_2Ti_2O_7$

The same as-grown sample used previously was annealed in oxygen which, as shown in Chapter 3, removed the isolated oxygen vacancies that make up the dominant form of disorder in the sample yielding a clear single crystal. As before, the sample was mounted in a dilution refrigerator on D7 and its temperature reduced to $T \sim 40$ mK with a guide field of 0.01 T applied. The sample was mounted on a copper plate that led to absorption with an angular dependence which accounts for the anomalous arc-like features in the data, see Section 4.1 and Fig. 4.2.

Figure 4.11 shows the complete depolarisation of the beam at low temperature indicating the transition to a ferromagnetic state. A single data point from the as-grown sample is included for comparison. On account of the beam depolarisation it does not make sense to consider the spin-flip and non spin-flip separately so Fig. 4.12 shows the combined channels in one figure. The depolarisation arises from the formation of a ferromagnetic phase with a magnetic domain with moments in different directions. Hence the guide field direction is lost as the neutron passes through the sample. When the field direction changes the neutron precesses about the field direction in the next domain. Eventually the neutron emerges from the sample with an effectively random magnetic moment direction.

Figure 4.13 shows the application of a 2.5 T field perpendicular to the plane of scattering with 40 s count times in both the spin-flip and non spin-flip channels. The sample remains ferromagnetic in both cases with negligible diffuse scattering observed. Note, the polarisation analysis does work in this case since the application of the field results in a single ferromagnetic domain.

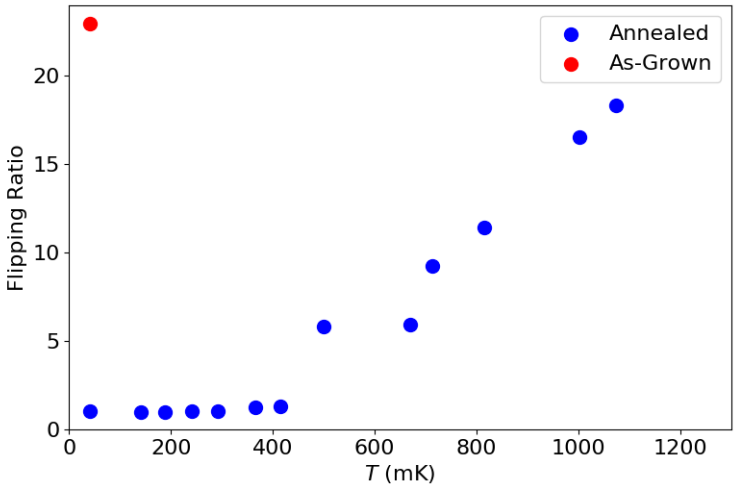

Figure 4.11: Flipping ratio for both oxygen-annealed and as-grown $Yb_2Ti_2O_7$. The oxygen-annealed sample transitions to a ferromagnetic state below $T \sim 400$ mK.

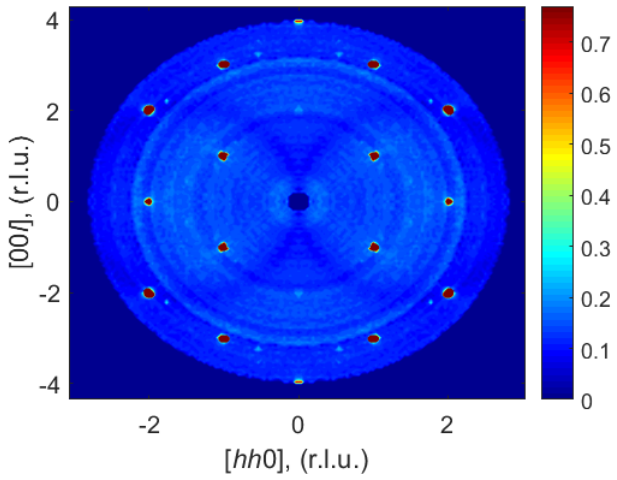

Figure 4.12: Oxygen-annealed $Yb_2Ti_2O_7$ total scattering in the (hhl) plane. The lack of diffuse scattering features is indicative of the depolarisation of the beam on account of the sample assuming a multi-domain ferromagnetic phase.

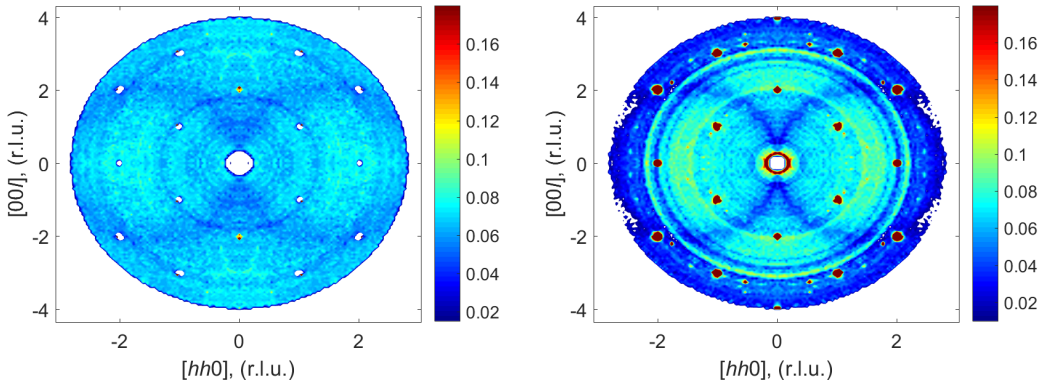

(a) (b)

Figure 4.13: Polarised diffuse neutron scattering of oxygen-annealed $Yb_2Ti_2O_7$ taken at $T \sim 59$ mK with an applied field of 2.5 T in (a) the spin-flip channel and (b) the non spin-flip channel of the (hhl) plane. The lack of diffuse scattering indicates the persistence of ferromagnetism relative to the low field measurement.

The sample was warmed to $T \sim 1200$ mK and measured and then cooled to $T \sim 500$ mK and measured again with results shown in Figs. 4.14 and 4.15 respectively. A count time of 40 s was used in each channel throughout. There is evidently a transition to a phase with short-range correlations on account of the emergence of the rods of scattering along [111] and the intensity at (220) as seen in the as-grown sample at base temperature. Above $T_c \sim 400$ mK the sample re-enters the Coulomb phase observed in the as-grown sample. The scattering at $T \sim 1200$ mK resembles the scattering from the as-grown sample at a comparable temperature, $T \sim 1500$ mK.

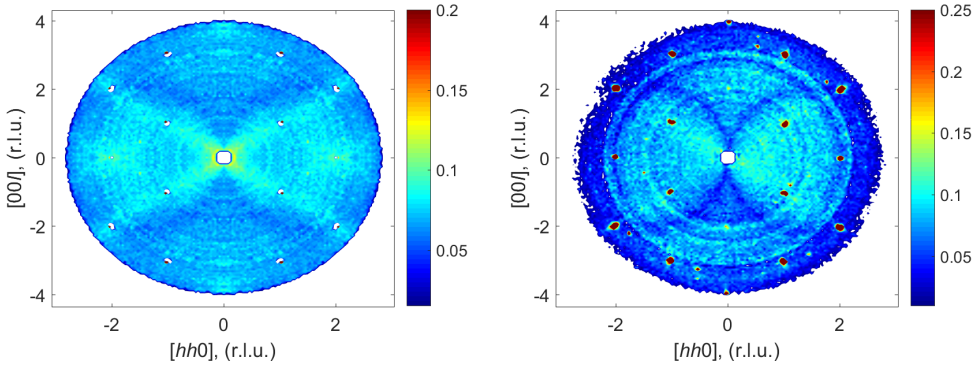

(a) (b)

Figure 4.14: Polarised diffuse neutron scattering of oxygen-annealed $Yb_2Ti_2O_7$ taken at $T \sim 1200$ mK in (a) the spin-flip channel and (b) the non spin-flip channel of the (hhl) plane. The presence of diffuse scattering features indicates the emergence of short-range order in the system.

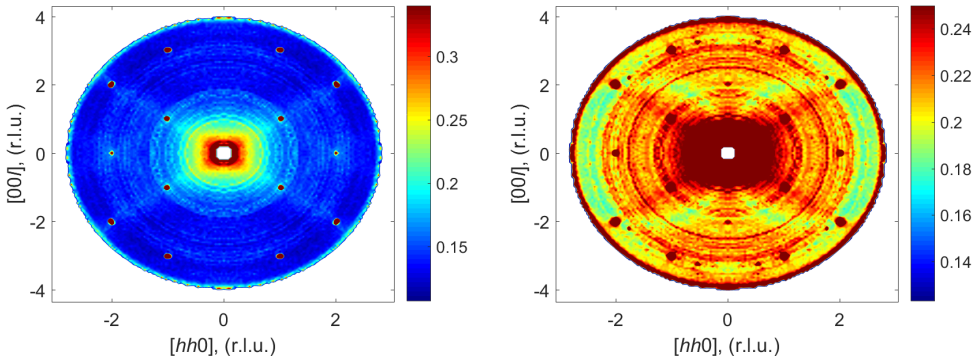

(a) (b)

Figure 4.15: Polarised diffuse neutron scattering of oxygen-annealed $Yb_2Ti_2O_7$ taken at $T \sim 500$ mK in (a) the spin-flip channel and (b) the non spin-flip channel of the (hhl) plane. The presence of diffuse scattering features indicates the emergence of short-range order in the system and to a slightly stronger degree than in Fig. 4.14.

Having established that the ground state of $Yb_2Ti_2O_7$ is ferromagnetic, this begs the question, what sort of ferromagnetism is exhibited? As discussed in Section 4.1 the proposed candidates are a two-in two-out model [119, 133, 165], an all-in all-out model [121] and a collinear model [114]. Taking the magnetic peak intensities from Gaudet et al. [133] for the two-in two-out model, Yaouanc et al. [121] for the all-in all-out model and Yasui et al. [114] for the collinear model and comparing them to our single crystal data for the base temperature ($T \sim 40$ mK) and guide field (0.01 T) measurement of the total scattering of stoichiometric $Yb_2Ti_2O_7$ using a least squares fit resulted in table 4.1. Plotting this in Fig. 4.16 illustrates that the experimental data show best agreement with the all-in all-out model. The collinear model is ruled out due to the intensity at the (220) peak and the two-in two-out is ruled out due to the absence of intensity at the (002) peak. The error bars on the (220) and (002) peaks are extremely small on account of the small contribution from structural reflections. From this it can be concluded that the true ground state of stoichiometric $Yb_2Ti_2O_7$ is an all-in all-out ferromagnetic state.

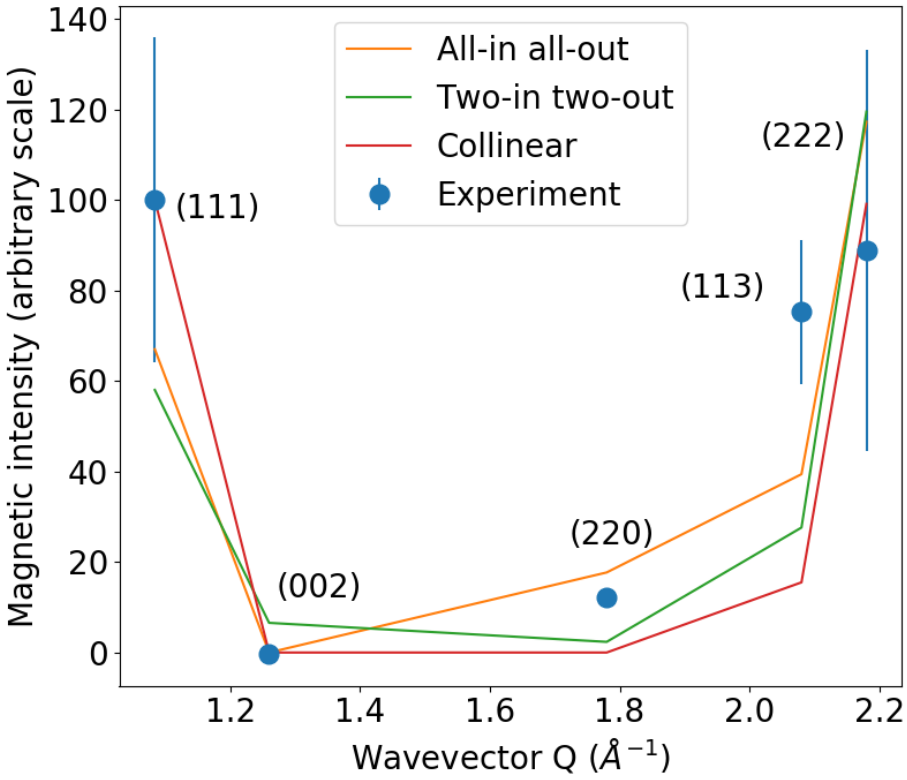

Figure 4.16: Comparison of annealed $Yb_2Ti_2O_7$ total scattering taken at base temperature and 0.01T to Gaudet et al. [133] for the two-in two-out model, Yaouanc et al. [121] for the all-in all-out model and Yasui et al. [114] for the collinear model. The experimental data shows the best agreement with the all-in all-out model. The collinear model is ruled out due to the intensity at the (220) peak and the two-in two-out is ruled out due to the absence of intensity at the (002) peak.

Reflection	D7 intensity	All-in all-out	Two-in two-out	Collinear
(111)	100(36)	67	58	100
(002)	-0.18(36)	0	6.6	0
(220)	12.1(9)	17.7	2.4	0
(113)	75(15)	39.3	27.6	15.5
(222)	88(44)	117.3	119.5	99.1

Table 4.1: Comparison of annealed $Yb_2Ti_2O_7$ total scattering taken at base temperature ($T \sim 40$ mK) to Gaudet et al. [133] for the two-in two-out model, Yaouanc et al. [121] for the all-in all-out model and Yasui et al. [114] for the collinear model. The values taken from the literature were minimised with repsect to the experimental data using a least squares fit. The resulting figure is shown in Fig. 4.16.

4.3.3 Oxygen-Depleted $Yb_2Ti_2O_7$

A sample of $Yb_2Ti_2O_7$ was annealed in hydrogen in order to create a sample with isolated oxygen vacancies as the dominant mode of disorder. This was mounted in a dilution refrigerator on D7 with the scattering plane along the (hhl) crystal plane. The sample was cooled to $T \sim 40$ mK with a guide field of 0.01 T applied and exposed for a 40 s count time in both the spin-flip and non spin-flip channels. Figure 4.17 shows the resulting scattering pattern. The rods along the [111] direction and the scattering at (220) indicates the presence of short-range correlations in the system. As with the sample of annealed $Yb_2Ti_2O_7$ there arc-like features observed on account of absorption from the copper mounting plate. These two experiments used the same overly thick mount.

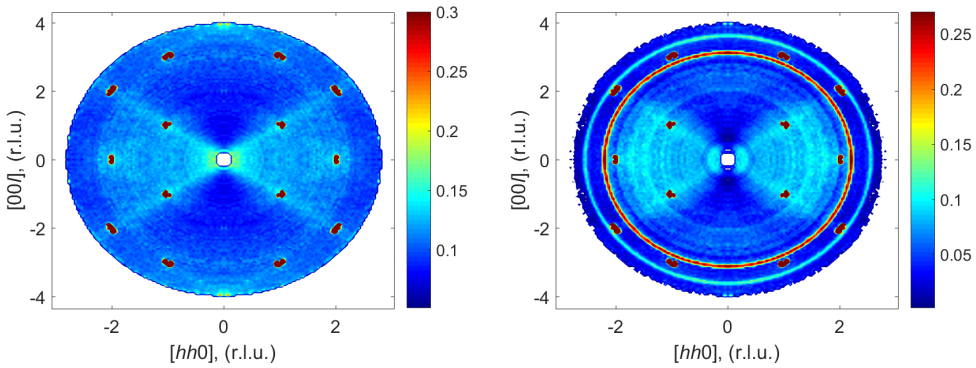

Figure 4.17: Polarised diffuse neutron scattering of oxygen-depleted $Yb_2Ti_2O_{7-\delta}$ taken at $T \sim 40$ mK in (a) the spin-flip channel and (b) the non spin-flip channel of the (hhl) plane. Short-range correlations in the system are indicated by the rods of scattering along [111] and the intensity at (220).

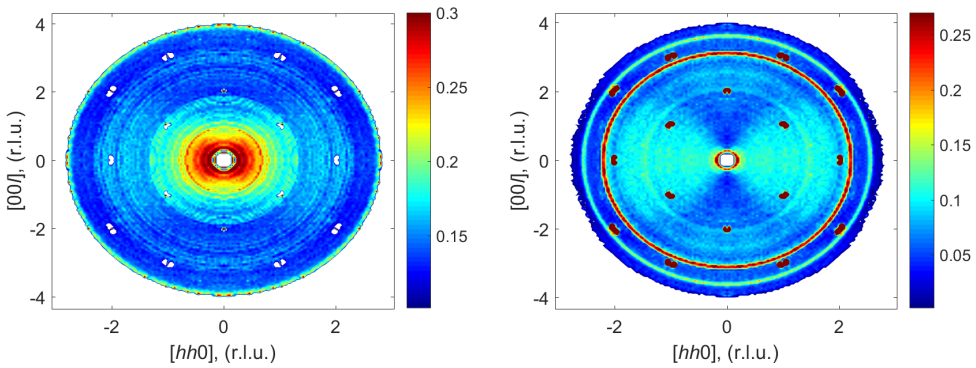

Figure 4.18: Polarised diffuse neutron scattering of oxygen-depleted $Yb_2Ti_2O_{7-\delta}$ taken at 40 mK with an applied field of 2.5 T in (a) the spin-flip channel and (b) the non spin-flip channel of the (hhl) plane. There are still weak diffuse scattering features although they are now much weaker as the application of a field pushes the sample towards single domain ferromagnetism.

A field of 2.5 T was applied perpendicular to the scattering plane with a count time of 31 s in each channel with the scattering shown in Fig. 4.18. The field was removed and the sample was warmed to $T \sim 1200$ mK with the resulting scattering shown in Fig. 4.20 and then cooled to $T \sim 500$ mK shown in Fig. 4.21. The scattering features seen at base temperature are still present but substantially weaker.

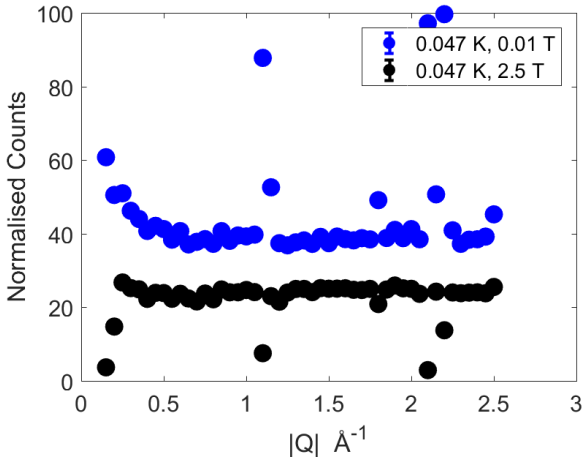

Figure 4.19: Depleted $Yb_2Ti_2O_7$ dependence with field. The application of a 2.5 T field causes a reduction in the magnetic diffuse scattering as the sample transitions away from a ferromagnetic state.

Figure 4.19 shows the variation of $|\mathbf{Q}|$ upon application of a 2.5 T field. At this saturation field of 2.5 T there is a marked reduction in the magnetic diffuse scattering observed in the sample. This is on account of the short range correlations being replaced by a single ferromagnetic domain leading to a reduction in the diffuse magnetic scattering.

The sample was heated to $T \sim 1200$ mK and measured with an exposure time of 40 s in each channel with the results shown in Fig. 4.20. The sample was cooled and measured again at $T \sim 500$ mK also with 40 s exposure times with the results shown in Fig. 4.21.

As can be clearly observed in the spin-flip channel in both measurements there is a significant reduction in the diffuse scattering features, both along [111] and around (220). This is on account of disorder being introduced in the sample on heating which suppresses these features, arising from magnetic correlations, as the sample tends towards being more paramagnetic.

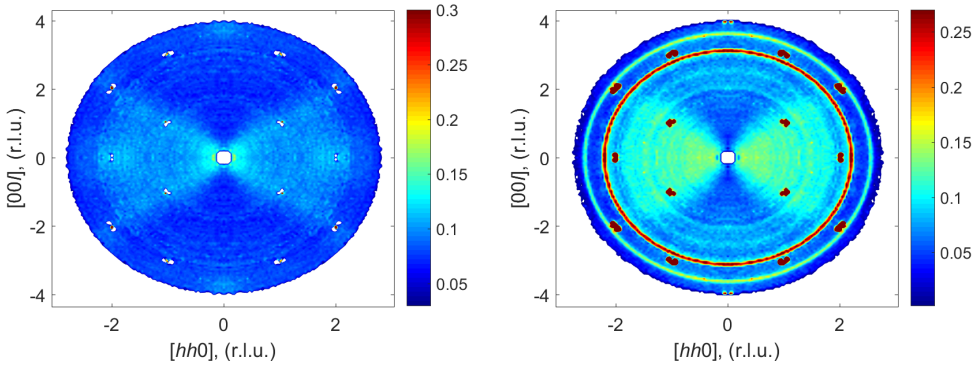

(a) (b)

Figure 4.20: Polarised diffuse neutron scattering of oxygen-depleted $Yb_2Ti_2O_{7-\delta}$ taken at $T \sim 1200$ mK in (a) the spin-flip channel and (b) the non spin-flip channel of the (hhl) plane. The diffuse scattering features present at base temperature are still present but are of a decreased intensity indicating the persistence of short range order.

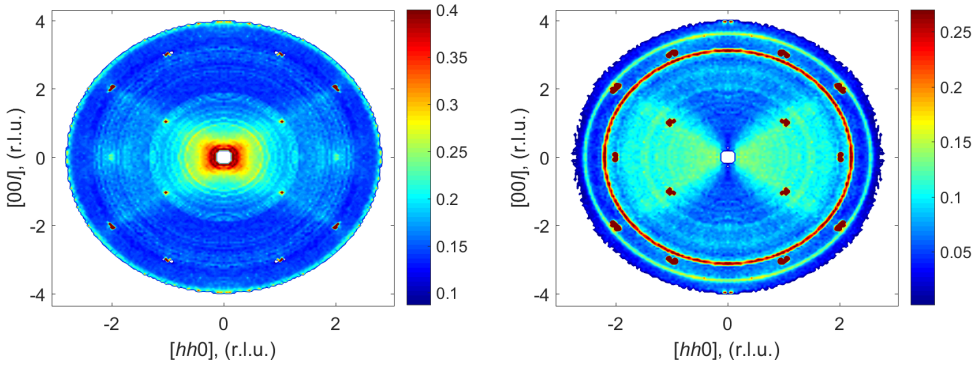

(a) (b)

Figure 4.21: Polarised diffuse neutron scattering of oxygen-depleted $Yb_2Ti_2O_{7-\delta}$ taken at $T \sim 500$ mK in (a) the spin-flip channel and (b) the non spin-flip channel of the (hhl) plane. The diffuse scattering features present at base temperature are still present but are of a decreased intensity indicating the persistance of short range order.

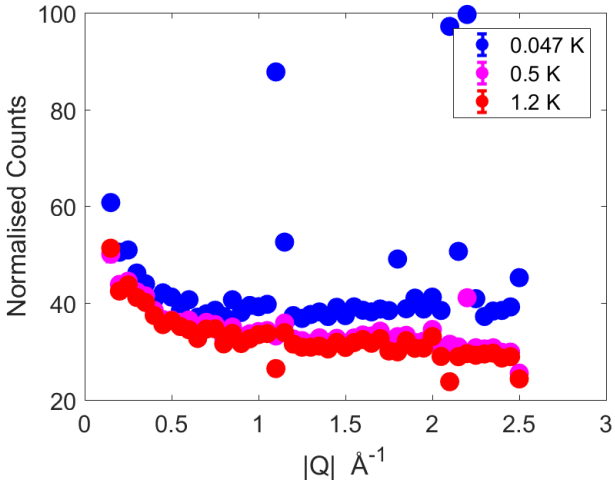

Figure 4.22: Depleted $Yb_2Ti_2O_{7-\delta}$ $|\mathbf{Q}|$ dependence with temperature in the spin-flip channel. Increasing the temperature leads to a reduction in the magnetic diffuse scattering as the samples magnetism becomes disordered.

Increasing temperature leads to a reduction in the intensity in $|\mathbf{Q}|$ across reciprocal space as shown in Fig. 4.22. As suggested previously, this is on account of a reduction in the magnetic correlations in the system as it attains a greater degree of magnetic disorder on increasing temperature.

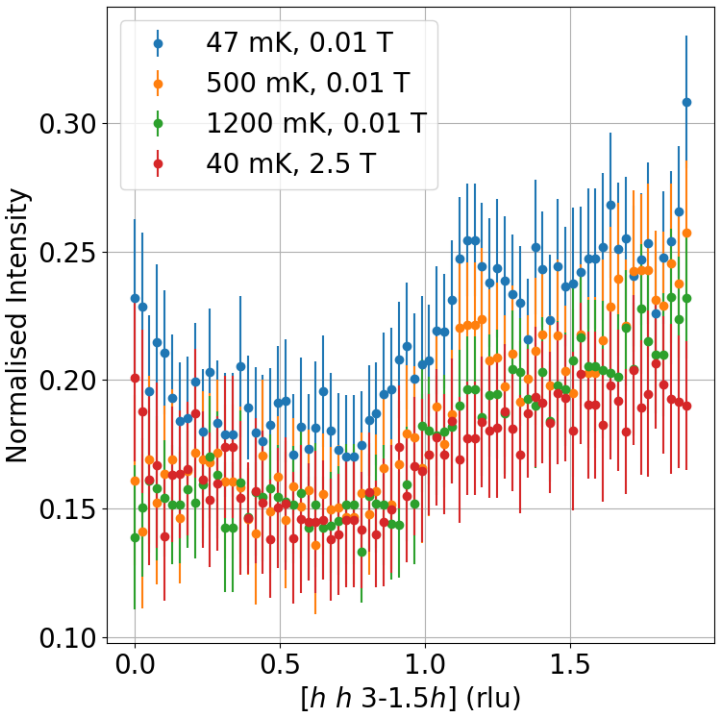

Figure 4.23: $[hh\ 3\text{-}1.5h]$ cut for oxygen depleted $Yb_2Ti_2O_7$ measurements in the spin-flip channel. All measurements away from the base temperature and field show reduced scattering intensity corresponding to the reduced correlations in the sample.

Each measurement shows diffuse scattering going across the [111] which is maintained going into the (220) region as shown in Fig. 4.23. The high field measurement shows the greatest suppression while the intermediate temperature samples show a reduced scattering intensity. The T $\sim$ 500 mK measurement still shows a significant intensity along the [111] direction.

4.3.4 Stuffed $Yb_{2+x}Ti_{2-x}O_{7-x/2}$

A sample of $Yb_{2+x}Ti_{2-x}O_{7-x/2}$ was mounted in a dilution refrigerator on D7 with the (hhl) plane in the scattering plane. The sample was cooled to $T \sim 60$ mK and exposed for 40 s in both channels. Fig. 4.24 shows the resultant scattering. There is evidently a region of scattering around (220) but the rods along [111] seem to have been largely suppressed, likely on account of the large amount of disorder in the system.

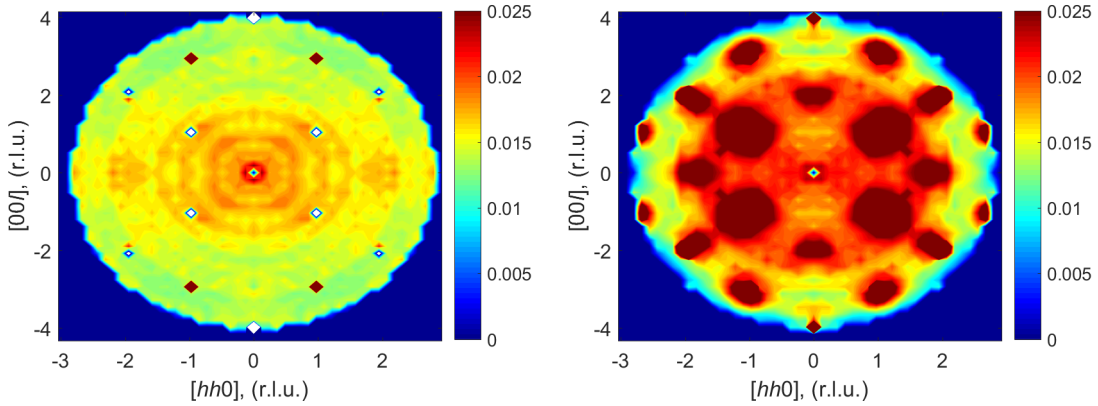

Figure 4.24: Polarised diffuse neutron scattering of stuffed $Yb_{2+x}Ti_{2-x}O_{7-x/2}$ taken at $T \sim 60$ mK in (a) the spin-flip channel and (b) the non spin-flip channel of the (hhl) plane. The magnetic diffuse scattering features are much weaker than in the less disordered samples at (220) and [111].

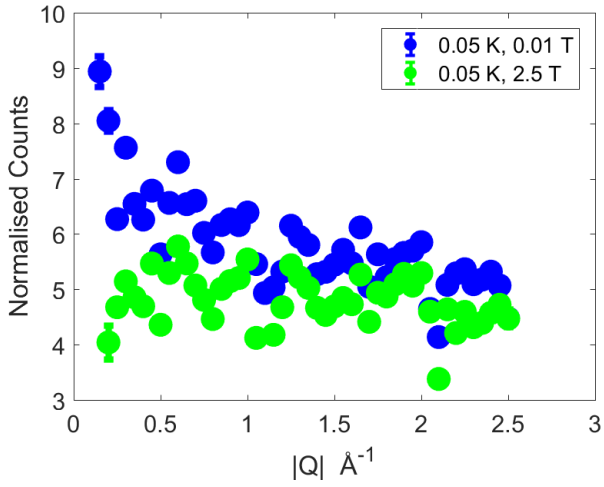

Figure 4.25: $Yb_{2+x}Ti_{2-x}O_{7-x/2}$ $|\mathbf{Q}|$ dependence with field in the spin-flip channel. Application of a 2.5 T field lead to the suppression of magnetic diffuse scattering features and short range correlations in the sample.

Figure 4.25 shows the variation of the count with $|\mathbf{Q}|$ in the spin-flip channels for both high and low field measurements. The low field measurement has an intensity that decreases as expected with $|\mathbf{Q}|$ indicating the increase in ferromagnetic ordering with applied field.

Application of a 2.5 T field perpendicular to the sample with 45 s count times in each channel (Fig. 4.26) led to the removal of the diffuse scattering features in the spin-flip channel indicating the absence of short range correlations in the system.

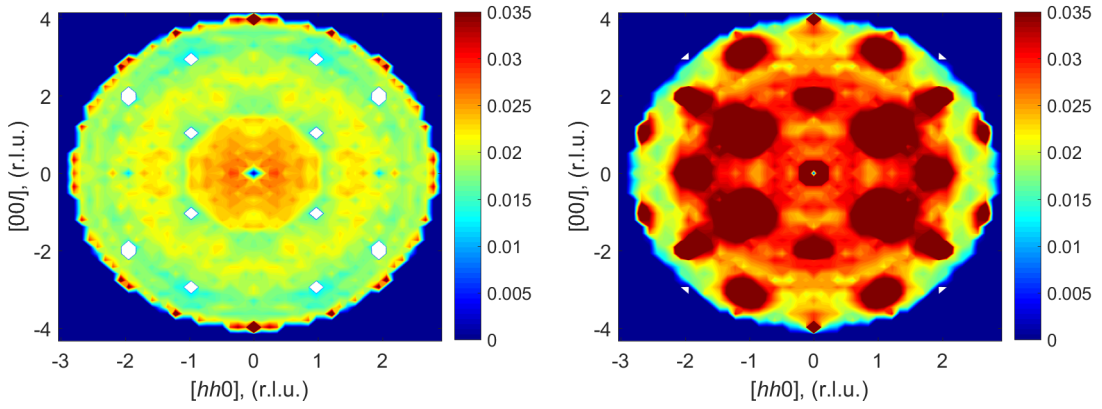

Figure 4.26: Polarised diffuse neutron scattering of stuffed $Yb_{2+x}Ti_{2-x}O_{7-x/2}$ taken at an applied field of 2.5 T in (a) the spin-flip channel and (b) the non spin-flip channel of the (hhl) plane.

The sample was warmed to $T \sim 2$ K and measured with a count time of 40 s which lead to a near complete suppression of the diffuse scattering in the spin-flip channel, shown in Fig. 4.27. Cooling and measuring at $T \sim 1$ K, Fig. 4.28, and $T \sim 500$ mK, Fig. 4.29, with the same count times showed a partial suppression of the (220) scattering seen at base temperature in the spin-flip channel.

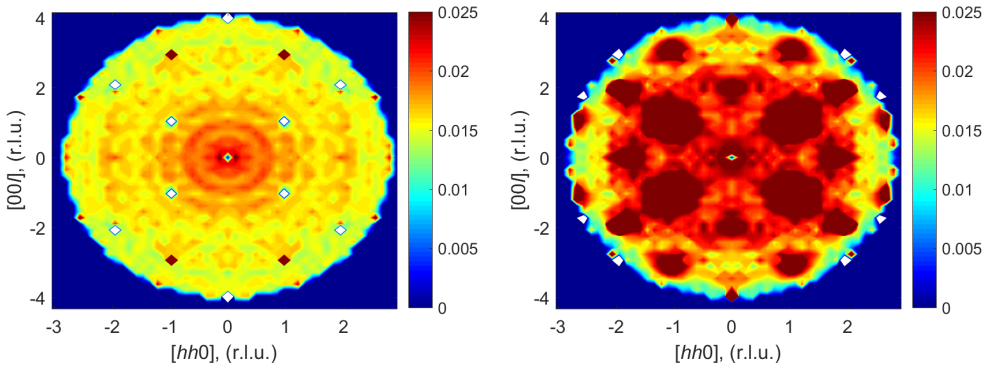

(a) (b)

Figure 4.27: Polarised diffuse neutron scattering of stuffed $Yb_{2+x}Ti_{2-x}O_{7-x/2}$ taken at $T \sim 2$ K in (a) the spin-flip channel and (b) the non spin-flip channel of the (hhl) plane. The magnetic diffuse scattering is nearly entirely suppressed in the spin flip channel as greater disorder is introduced into the system.

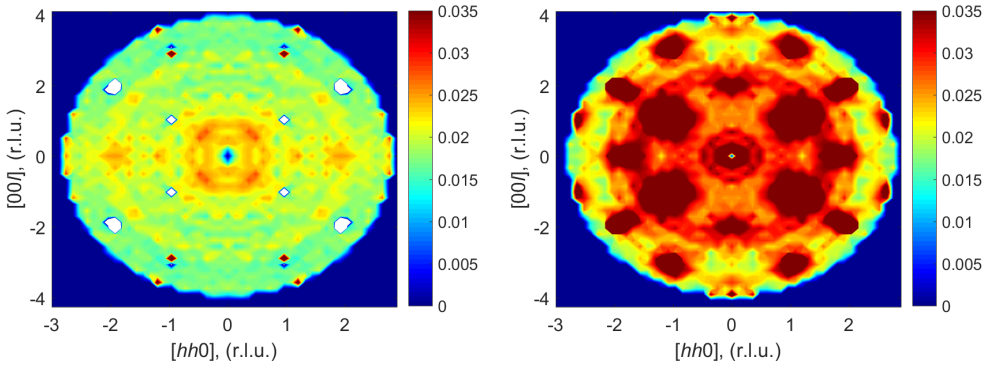

(a) (b)

Figure 4.28: Polarised diffuse neutron scattering of stuffed $Yb_{2+x}Ti_{2-x}O_{7-x/2}$ taken at $T \sim 1$ K in (a) the spin-flip channel and (b) the non spin-flip channel of the (hhl) plane. The magnetic diffuse scattering is nearly entirely suppressed in the spin flip channel although to a lesser degree than in Fig. 4.27.

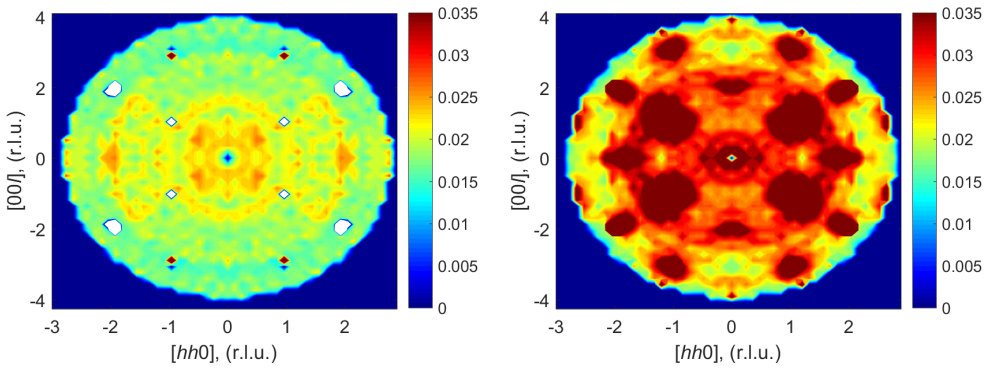

Figure 4.29: Polarised diffuse neutron scattering of stuffed $Yb_{2+x}Ti_{2-x}O_{7-x/2}$ taken at $T \sim 500$ mK in (a) the spin-flip channel and (a) the non spin-flip channel of the (hhl) plane. The increase in temperature causes the suppression of the magnetic diffuse scattering features across reciprocal space although there is still clear evidence of intensity at (220) and some along [111].

Figure 4.30 shows the scattering intensity with $|\mathbf{Q}|$ at a range of measured intensities. The decreasing intensity with $|\mathbf{Q}|$ indicates the prevalence of paramagnetism in these samples with a distinct lack of ordering up until around $|\mathbf{Q}| = 2$ Å^{-1} where the contribution of weak correlations manifesting around (220) causes the signal to flatten out somewhat.

The stuffed sample shows substantially different magnetic character to the other samples measured here. Figure 4.31 shows that the ground state exhibits a relatively flat signal with an increasing intensity in $|\mathbf{Q}|$. it does not appear to have the same diffuse features present in the other disordered samples with increased diffuse scattering absent along [111] and very weak around (220).

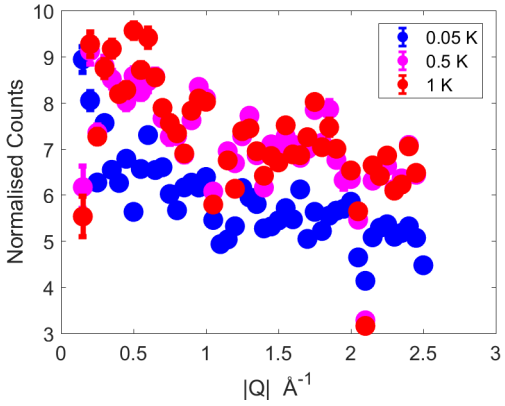

Figure 4.30: $Yb_{2+x}Ti_{2-x}O_{7-x/2}$ scattering intensity with $|\mathbf{Q}|$ at a range of measured intensities in the spin-flip channel. The reduction is intensity broadly proportional to $|\mathbf{Q}|$ indicates paramagnetism at each measurement.

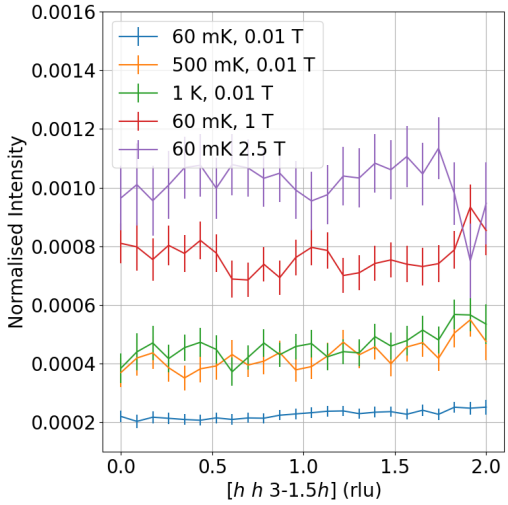

Figure 4.31: $[hh\ 3\text{-}1.5h]$ cut for $Yb_{2.5}Ti_{1.5}O_{6.75}$ measurements in the spin-flip channel showing a relatively flat signal relative to the other disordered samples showing that the nature of the disorder is fundamentally different.

4.4 Discussion

Evidently the ground state of $Yb_2Ti_2O_7$ is extremely sensitive to variations in stoichiometry with the as-grown and the oxygen-annealed samples exhibiting differing magnetic states despite having a relatively small change in the oxygen concentration. Only the oxygen-annealed sample achieves a ferromagnetic ground state at base temperature where the introduction of even a small amount of disorder renders this state inaccessible. All of the other samples exhibit some form of magnetic diffuse scattering at base temperature although the nature of the diffuse scattering is itself dependent on the degree and type of disorder. The samples with isolated oxygen vacancies, the oxygen-depleted and the as-grown $Yb_2Ti_2O_7$ show rods of scattering along the [111] direction in the spin-flip channel corresponding to a Coulomb spin phase [103]. For the stuffed sample with additional magnetic ions outside the corner-sharing tetrahedra, this feature is largely suppressed as the presence of additional exchange pathways suppresses the characteristic spin correlations associated with $Yb_2Ti_2O_7$ in the Coulomb liquid phase. All of the the disordered samples show broad scattering features around (220) indicating short-ranged antiferromagnetic correlations, which one would expected to be absent in the limit of collinear ferromagnetic order [119].

These results have significant implications with regard to the existing literature on the subject and by paying careful attention to growth conditions it is clear that the magnetic state of $Yb_2Ti_2O_7$ can be controlled. These results are consistent with the findings by Chang et al. that show low temperature depolarisation of the beam and a transition to a ferromagnetic ground state [103]. The features observed at intermediate temperatures are consistent with both their observed scattering and their calculations for the spin-flip scattering.

Chang et al. also provide a visualisation of the expected scattering that is entirely consistent with results obtained here for the oxygen-depleted and as-grown samples

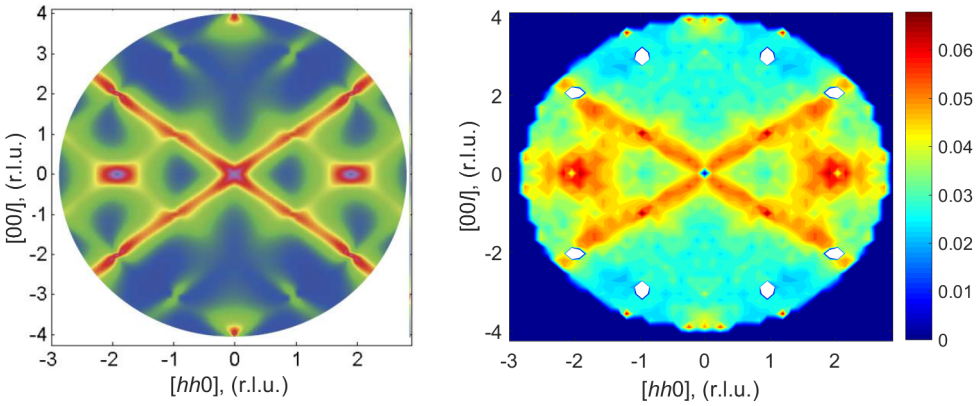

(a) (b)

Figure 4.32: Comparison of (a) calculation from Ref. [103] with (b) experimentally acquired results for as-grown $Yb_{2.5}Ti_{1.5}O_{6.75}$ in the spin-flip channel of the (hhl) plane at $T \sim 60$ mK acquired by polarised neutron scattering showing good agreement between calculation and experiment as all the strong diffuse scattering features are reproduced.

of $Yb_2Ti_2O_7$ as shown in Fig. 4.32 [103]. The calculation by Chang et al. clearly reproduces the diffuse scattering along [111] and the broad features around (220) and (004). Robert et al. [119] and Jaubert et al. [166] also provide calculations that reproduce these features suggesting the data is consistent with a range of exchange constants.

It is notable that when annealing in oxygen, Ross et al. found that there was no change in the transparency of the sample [167] whereas our results and those of Chang et al. [103] find otherwise. Each of these studies were carried out on crystals grown by the floating zone method but transparent single crystal pyrochlores have also been grown using reactive spark plasma sintering [168].

The identification of a number of distinct magnetic phases make clear the significant impact of even low levels of structural disorder in understanding $Yb_2Ti_2O_7$ and that

the true ground state of stoichiometric $Yb_2Ti_2O_7$ is ferromagnetic. This conclusion is entirely consistent with results of inelastic neutron studies of the spin Hamiltonian [138]. Exchange constants have been derived that are consistent with magnon energies at many points in reciprocal space and for different magnetic field directions, and these values are also consistent with those used by Robert et al. [119] to reproduce the magnetic diffuse scattering intensities. A semi-classical mean-field analysis with these exchange couplings places the system in the splayed ferromagnetic phase observed experimentally which is far from the quantum liquid phase but very close in parameter space to an antiferromagnetic phase [76, 131, 169]. The sensitivity of the magnetic ground state to modest hydrostatic pressure is consistent with the proposed proximity to a phase boundary. However, it was suggested that the stabilisation of the ferromagnetic phase through application of hydrostatic pressure implies that the observation of a ferromagnetic ground state arises when stuffing leads to chemical pressure [137].

It is then surprising that the deliberately stuffed sample does not exhibit a ferromagnetic ground state under any conditions. We demonstrate that stuffing has the opposite effect of washing out spin correlations on the Coulomb phase.

For the stoichiometric annealed sample, comparing our experimentally acquired values to those in the literature [114, 121, 165] leads to the conclusion the nature of the ferromagnetism is an all-in all-out state in agreement with Yaouanc et al. [121].

Chapter 5

Conclusions

The results presented in this thesis cover both the defect structure and the magnetic structure of $Yb_2Ti_2O_7$ although naturally these two properties are inextricably linked, with the defect structure strongly affecting the magnetic ground state.

Three high quality single crystal samples of $Yb_2Ti_2O_7$ were grown by Dr D. Prabhakaran using the floating zone method at the Clarendon laboratory, Oxford University and these samples were used in both the experiments performed on SXD at ISIS and D7 at the ILL. One of these samples was measured without further treatment and is referred to as 'as-grown'. The depleted sample was annealed in a mix of hydrogen and argon gas resulting in a highly oxygen deficient black crystal with isolated vacancies. An orange/brown stuffed sample was grown with an excess of Yb atoms to allow for contrast between the experimental signature resulting from isolated oxygen vacancies and those arising from stuffing. Finally after the measurements were completed on the as-grown sample it was annealed in oxygen creating a stoichiometric transparent crystal which could be used to determine the true ground state of ytterbium titanate. It is noted that Chang et al. reported a transparent sample [103], whereas the sample used by Ross et al. [167] was not transparent.

For the as-grown single crystal sample of $Yb_2Ti_2O_7$ studied here the dominant form of defects are isolated oxygen vacancies. This was demonstrated by the fact that the oxygen annealing resulted in the removal of structural diffuse scattering. In the case of a heavily oxygen-depleted sample it was possible to account for the diffuse scattering using the Monte-Carlo balls and springs model by qualitatively reproducing the scattering in a model with isolated defects.

A diffuse scattering measurement on a stuffed $Yb_{2+x}Ti_{2-x}O_{7-x/2}$ single crystal showed that its diffuse scattering features are qualitatively different to those of a sample with isolated oxygen vacancies. Once again this conclusion is supported by a balls and springs model for a stuffed system where the diffuse scattering features are well reproduced. It was also shown that using a balls and springs model for both a system with isolated vacancies and for a system with vacancies arising from stuffing that vacancies on the 48f O(2) site better reproduce the diffuse scattering features than a model with vacancies on the 8b O(1) site. It is also the case for the depleted system that from refinements on x-ray diffraction data it is shown that there is an small decrease in the lattice parameter between the oxygen annealed sample and the depleted sample. This is significant as Sala et al. [91] found that for the rare earth pyrochlore $Y_2Ti_2O_7$ isolated O(1) vacancies were the dominant form of disorder and in contrast to $Yb_2Ti_2O_7$ this led to an increase in the lattice parameter between the oxygen annealed and depleted samples.

From the modelling of the diffuse scattering of systems with isolated oxygen vacancies and vacancies arising from stuffing it can be seen that the distortions to the lattice resulting from defects is dependent on the nature of the defects. In the case of systems with isolated oxygen vacancies the nearest neighbour titanium ions move away from the vacancy site and towards the oxygen ions positioned on the vector between the vacancy and the titanium ions. This gives a second order displacement of these oxygen ions

which themselves move away from the vacancy along this vector. The resulting Ti^{3+}-O(2) bond length is in quantitative agreement with values published for $Y_2Ti_2O_{7-\delta}$ [91] and Ti_2O_3 [164]. This is interestingly in contrast to the distortions in a stuffed system. In this case the Yb ions sitting on the sites normally occupied by titanium ions move towards the vacancy site and there is negligible second order movement by nearest neighbour oxygen ions. This results in a larger Yb^{3+}-O(2) bond length than Ti^{3+}-O(2), as expected for the larger radius of Yb^{3+}.

It is important to note that the discovery that as-grown $Yb_2Ti_2O_7$ has isolated oxygen vacancies is in contrast to some of the existing suggestions in the literature for samples grown using the floating zone method. Stuffing has been proposed as the source of 'as-grown' defects [100, 101] along with the swapping of Yb and Ti ions at a level of 2% [102] and isolated Yb vacancies [103]. This result does however support the findings of Blundred et al. [93] who observe isolated oxygen vacancies on the O(2) site of $Yb_2Ti_2O_7$ for a sample reduced at low temperature in a topotactic reaction with CaH_2.

The geometric frustration experienced by pyrochlores has been previously shown to suppress long range order in the cases of the spin ices $Dy_2Ti_2O_7$ and $Ho_2Ti_2O_7$ [105, 106, 107] and the spin liquid $Tb_2Ti_2O_7$ [82, 84]. The majority of recent literature points towards $Yb_2Ti_2O_7$ exhibiting a ferromagnetic ground state although the nature of this ferromagnetism is contested with suggestions of a two-in two-out [119, 133, 165], colinear [114] and all-in all-out [121] being proposed. One recent paper suggests that the observation of ferromagnetism is the result of stuffing [137].

It is possible that the disagreements in the literature arise from the presence of low level defects as in other pyrochlores such as $Y_2Ti_2O_7$, $Ho_2Ti_2O_7$, $Tb_2Ti_2O_7$ and $Pr_2Zr_2O_7$ minor variations in the stoichiometry have lead to variations in the ground state [91, 95, 96, 97, 98]. Having established that the annealed sample is stoichiometric

it is possible to conclusively determine the true ground state of $Yb_2Ti_2O_7$.

It was proven that for a single crystal sample of stoichiometric $Yb_2Ti_2O_7$ the true magnetic ground state is ferromagnetic. The determination of the structure means that it can be said with confidence that the sample used was stoichiometric and the depolarisation of the beam and absence of diffuse scattering when the sample was measured on D7 proves that it is ferromagnetic. By studying the relative Bragg peak intensities and most significantly the systematic absences of intensity to those for the proposed models in the literature it is shown that $Yb_2Ti_2O_7$ exhibits an all-in all-out ferromagnetic ground state.

The magnetism of defective samples has also been determined. For an oxygen-depleted sample there is no depolarisation of the beam down to base temperature and the diffuse scattering in the (hhl) plane is qualitatively similar to that of the as-grown sample. This suggests that the presence of isolated oxygen vacancies suppresses the ferromagnetic phase down to the lowest measured temperature and that spin liquid behaviour is reinforced. The magnetic diffuse scattering of the samples with isolated oxygen vacancies is also consistent with the expected scattering calculated by Chang et al. [103] which shows long rods of scattering along $\langle 111 \rangle$ along with broad features around (220) and (004). This result is consistent with the calculations of Robert et al. [119] and Jaubert et al. [166] which reproduce these features suggesting that the experimentally acquired data is consistent with a range of exchange constants. In contrast to the speculation in Kermarrec et al. [137], ferromagnetism is shown to be suppressed by stuffing. The nature of the magnetic scattering is qualitatively different with some diffuse scattering features also suppressed, suggesting it is dominated by uncorrelated spins unlike in the systems with isolated defects.

It can be inferred from this that by paying careful attention to the stoichiometry which can be controlled via the growth process that the both the magnetism and com-

position of $Yb_2Ti_2O_7$ can be controlled due to the wildly varying results for even minor changes in the stoichiometry.

To summarise it has been shown that even low levels of defects change the ground state of $Yb_2Ti_2O_7$ so any future experiments on this system will need to ensure that samples are defect free or that they are at least well understood and accounted for. The sensitivity of single crystal neutron scattering to defect structures means that this technique can be used in order to gain such an understanding. The success of this technique for also determining the source of defects in $Y_2Ti_2O_7$ [91] suggests that the process used here for determination of the defect structure could be used to understand other pyrochlore systems.

One promising direction for future study would be direct comparison of the structural diffuse scattering with first-principle density functional theory. In calculating the energies of defects such as O(1) or O(2) vacancies in pyrochlores it is often difficult to distinguish between models by energy stability alone. However, the predicted ionic displacements in geometry optimisation can be directly compared with structural diffuse scattering, and this is an additional way to distinguish between defect models.

Bibliography

[1] H. Sakai, K. Yoshimura, H. Ohno, H. Kato, S. Kambe, R. E. Walstedt, T. D. Matsuda, Y. Haga, and Y. Onuki. Superconductivity in a pyrochlore oxide, $Cd_2Re_2O_7$. *J. Phys.: Condens. Matter*, 13(33):L785, 2001.

[2] P. Laurell and G. A. Fiete. Topological magnon bands and unconventional superconductivity in pyrochlore iridate thin films. *Phys. Rev. Lett.*, 118:177201, 2017.

[3] S. Yonezawa, Y. Muraoka, Y. Matsushita, and Z. Hiroi. Superconductivity in a pyrochlore-related oxide KOs_2O_6. *J. Phys.: Condens. Matter*, 16(3):L9, 2004.

[4] T. Takeda, M. Nagata, H. Kobayashi, R. Kanno, Y. Kawamoto, M. Takano, T. Kamiyama, F. Izumi, and A. W. Sleight. High−pressure synthesis, crystal structure, and metal−semiconductor transitions in the $Tl_2Ru_2O_7$ pyrochlore. *J. Solid State Chem.*, 140(2):182 – 193, 1998.

[5] G. T. Knoke, A. Niazi, J. M. Hill, and D. C. Johnston. Synthesis, structure, and ferromagnetism of the oxygen defect pyrochlore system $Lu_2V_2O_{7-x}$ ($x = 0.40 - 0.65$). *Phys. Rev. B*, 76:054439, 2007.

[6] T. Aguilar, J. Navas, D. M. De los Santos, A. Sanchez-Coronilla, C. Fernandez-Lorenzo, R. Alcantara, J. J. Gallardo, G. Blanco, and J. Martn-Calleja. TiO_2 and

pyrochlore $Tm_2Ti_2O_7$ based semiconductor as a photoelectrode for dye-sensitized solar cells. *J. Phys. D: Appl. Phys.*, 48(14):145102, 2015.

[7] B. D. Gaulin, J. S. Gardner, S. R. Dunsiger, and Z. Tun. Neutron scattering studies of geometrically frustrated pyrochlore antiferromagnets. *Physica B*, 241:511–516, 1997.

[8] A. M. Hallas, J. Gaudet, M. N. Wilson, T. J. Munsie, A. A. Aczel, M. B. Stone, R. S. Freitas, A. M. Arevalo-Lopez, J. P. Attfield, M. Tachibana, C. R. Wiebe, G. M. Luke, and B. D. Gaulin. XY antiferromagnetic ground state in the effective $s = \frac{1}{2}$ pyrochlore $Yb_2Ge_2O_7$. *Phys. Rev. B*, 93:104405, 2016.

[9] S. R. Dunsiger, R. F. Kiefl, K. H. Chow, B. D. Gaulin, M. J. P. Gingras, J. E. Greedan, A. Keren, K. Kojima, G. M. Luke, W. A. MacFarlane, N. P. Raju, J. E. Sonier, Y. J. Uemura, and W. D. Wu. Muon spin relaxation investigation of frustrated antiferromagnetic pyrochlores $A_2B_2O_7$. *Hyperfine Interact.*, 104(1):275–280, 1997.

[10] N. P. Raju, E. Gmelin, and R. K. Kremer. Magnetic-susceptibility and specific-heat studies of spin-glass-like ordering in the pyrochlore compounds $R_2Mo_2O_7$ (R=Y, Sm, or Gd). *Phys. Rev. B*, 46:5405–5411, 1992.

[11] H. Shinaoka, Y. Tomita, and Y. Motome. Spin-glass transition in bond-disordered Heisenberg antiferromagnets coupled with local lattice distortions on a pyrochlore lattice. *Phys. Rev. Lett.*, 107:047204, 2011.

[12] J. Leduc, Y. Gonullu, A. Raauf, T. Fischer, and S. Mathur. Rare-earth-containing materials for photoelectrochemical water splitting applications. *Semiconduct. Semimet.*, 97:185 – 219, 2017.

[13] N. Kumar, A. Roy, Z. Wang, E. M. L′Abbate, D. Haynes, D. Shekhawat, and J. J. Spivey. Bi-reforming of methane on Ni-based pyrochlore catalyst. *Appl. Catal., A: General*, 517:211 – 216, 2016.

[14] S. Gaur, D. J. Haynes, and J. J. Spivey. Rh, Ni, and Ca substituted pyrochlore catalysts for dry reforming of methane. *Appl. Catal., A*, 403(1):142 – 151, 2011.

[15] F. Zhong, L. Shi, J. Z., G. Cai, Y. Zheng, Y. Xiao, and J. Long. Ce incorporated pyrochlore $Pr_2Zr_2O_7$ solid electrolytes for enhanced mild-temperature NO_2 sensing. *Ceram. Int.*, 43(15):11799 – 11806, 2017.

[16] A. Shlyakhtina and L. G. Shcherbakova. New solid electrolytes of the pyrochlore family. *Russ. J. Electrochem.*, 48:1–25, 2012.

[17] J. W. Fergus. Zirconia and pyrochlore oxides for thermal barrier coatings in gas turbine engines. *Metall. Mater. Trans. E*, 1(2):118–131, 2014.

[18] R. Vassen, F. Traeger, and D. Stover. New thermal barrier coatings based on pyrochlore/YSZ double-layer systems. *Int. J. Appl. Cerman. Tec.*, 1:351 – 361, 2004.

[19] K. E. Sickafus, L. Minervini, R. W. Grimes, J. A. Valdez, M. Ishimaru, F. Li, K. J. McClellan, and T. Hartmann. Radiation tolerance of complex oxides. *Science*, 289(5480):748–751, 2000.

[20] R. C. Ewing, W. J. Weber, and J. Lian. Nuclear waste disposal − pyrochlore ($A_2B_2O_7$): Nuclear waste form for the immobilization of plutonium and minor actinides. *J. Appl. Phys.*, 95(11):5949–5971, 2004.

[21] J. Prakash, D. Tryk, W. Aldred, and E Yeager. *Transition-Metal Oxide Electrocatalysts for O2 Electrodes: The Pyrochlores*. Springer US, Boston, MA, 1992.

[22] T. Siritanon. Structure-property relationships in oxides containing tellurium. Master's thesis, Oregon State University, 2011.

[23] M. A. Subramanian, G. Aravamudan, and G. V. S. Rao. Oxide pyrochlores a review. *Prog. Solid State Chem.*, 15(2):55 – 143, 1983.

[24] H. R. Hoekstra and S. Siegel. Variation of the oxygen positional parameter in pyrochlores. *Inorg. Chem.*, 8(9):2039–2039, 1969.

[25] F. Jona, G. Shirane, and R. Pepinsky. Dielectric, x-ray, and optical study of ferroelectric $Cd_2Nb_2O_7$ and related compounds. *Phys. Rev.*, 98:903–909, 1955.

[26] E. Aleshin and R. Roy. Crystal chemistry of pyrochlore. *J. Am. Ceram. Soc.*, 45(1):18–25, 1962.

[27] W. R. Cook and H. Jaffe. Ferroelectricity in oxides of face-centered cubic structure. *Phys. Rev.*, 89:1297–1298, 1953.

[28] J. M. Longo, P. M. Raccah, and J. B. Goodenough. $Pb_2M_2O_{7-x}$ (M = Ru, Ir, Re) - preparation and properties of oxygen deficient pyrochlores. *Mater. Res. Bull.*, 4(3):191 – 202, 1969.

[29] L. Minervini, R. W. Grimes, Y. Tabira, R. L. Withers, and K. E. Sickafus. The oxygen positional parameter in pyrochlores and its dependence on disorder. *Philos. Mag. A*, 82(1):123–135, 2002.

[30] S. C. Zhang, Z. Middleburgh, M. de los Reyes, G. R. Lumpkin, B. J. Kennedy, P. E. R. Blanchard, E. Reynolds, and L. Y. Jang. Gradual structural evolution from pyrochlore to defect-fluorite in $Y_2Sn_{2-x}Zr_xO_7$: Average vs local structure. *J. Phys. Chem. C*, 117(50):26740–26749, 2013.

[31] J. Vannimenus and G. Toulouse. Theory of the frustration effect. II. Ising spins on a square lattice. *J. Phys. C: Solid State Phys.*, 10(18):L537, 1977.

[32] A. A. Zvyagin. New physics in frustrated magnets: Spin ices, monopoles, etc. (review article). *Low Temp. Phys.*, 39(11):901–922, 2013.

[33] R. D. Kamien and J. V. Selinger. Order and frustration in chiral liquid crystals. *J. Phys.: Condens. Matter*, 13(3):R1, 2001.

[34] D. Zhou, F. Wang, B. Li, X. Lou, and Y. Han. Glassy spin dynamics in geometrically frustrated buckled colloidal crystals. *Phys. Rev. X*, 7:021030, 2017.

[35] R. F. Wang, C. Nisoli, R. S. Freitas, J. Li, W. McConville, B. J. Cooley, M. S. Lund, N. Samarth, C. Leighton, V. H. Crespi, and P. Schiffer. Artificial spin ice in a geometrically frustrated lattice of nanoscale ferromagnetic islands. *Nature*, 439(7074):303–306, 2006.

[36] F. J. Fattoyev, C. J. Horowitz, and B. Schuetrumpf. Quantum nuclear pasta and nuclear symmetry energy. *Phys. Rev. C*, 95:055804, 2017.

[37] A. Leonov. Multiply periodic states and isolated skyrmions in an anisotropic frustrated magnet. *Nat. Commun.*, 6:8275, 2015.

[38] A. Fert, V. Cros, and J. Sampaio. Skyrmions on the track. *Nat. Nanotechnol.*, 8:152–156, 2013.

[39] Y. Zhou and M. Ezawa. A reversible conversion between a skyrmion and a domain-wall pair in a junction geometry. *Nat. Comm.*, 5:4652, 2014.

[40] V. Cannella and J. A. Mydosh. Magnetic ordering in gold-iron alloys. *Phys. Rev. B*, 6:4220–4237, 1972.

[41] X. Obradors, A. Labarta, A. Isalgu, J. Tejada, J. Rodriguez, and M. Pernet. Magnetic frustration and lattice dimensionality in $SrCr_8Ga_4O_{19}$. *Solid State Commun.*, 65(3):189 – 192, 1988.

[42] A. P. Ramirez, G. P. Espinosa, and A. S. Cooper. Strong frustration and dilution-enhanced order in a quasi-2D spin glass. *Phys. Rev. Lett.*, 64:2070–2073, 1990.

[43] Z. L. Dun, J. Trinh, K. Li, M. Lee, K. W. Chen, R. Baumbach, Y. F. Hu, Y. X. Wang, E. S. Choi, B. S. Shastry, A. P. Ramirez, and H. D. Zhou. Magnetic ground states of the rare-earth tripod kagome lattice $Mg_2RE_3Sb_3O_{14}$ (RE = Gd, Dy, Er). *Phys. Rev. Lett.*, 116:157201, 2016.

[44] Z. L. Dun, J. Trinh, M. Lee, E. S. Choi, K. Li, Y. F. Hu, Y. X. Wang, N. Blanc, A. P. Ramirez, and H. D. Zhou. Structural and magnetic properties of two branches of the tripod-kagome-lattice family $A_2R_3Sb_3O_{14}$ (A = Mg, Zn; R = Pr, Nd, Gd, Tb, Dy, Ho, Er, Yb). *Phys. Rev. B*, 95:104439, 2017.

[45] J. A. M. Paddison, H. S. Ong, J. O. Hamp, P. Mukherjee, X. Bai, M. Tucker, N. Butch, C. Castelnovo, M. Mourigal, and S. Dutton. Emergent order in the kagome Ising magnet $Mg_2Dy_3Sb_3O_{14}$. *Nat. Commun.*, 7(13842), 2016.

[46] A. B. Cairns, M. J. Cliffe, J. A. M. Paddison, D. Daisenberger, M. G. Tucker, F. X. Coudert, and A. L. Goodwin. Encoding complexity within supramolecular analogues of frustrated magnets. *Nat. Chem.*, 8(5):442–447, 2016.

[47] S. K. Pati and C. N. R. Rao. Kagome network compounds and their novel magnetic properties. *Chem. Commun.*, 39:4683–4693, 2008.

[48] M. E. Zhitomirsky. Octupolar ordering of classical kagome antiferromagnets in two and three dimensions. *Phys. Rev. B*, 78:094423, 2008.

[49] S. Muhlbauer, B. Binz, F. Jonietz, C. Pfleiderer, A. Rosch, A. Neubauer, R. Georgii, and P. Boni. Skyrmion lattice in a chiral magnet. *Science*, 323(5916):915–919, 2009.

[50] H. D. Zhou, B. W. Vogt, J. A. Janik, Y. J. Jo, L. Balicas, Y. Qiu, J. R. D. Copley, J. S. Gardner, and C. R. Wiebe. Partial field-induced magnetic order in the spin-liquid kagome $Nd_3Ga_5SiO_{14}$. *Phys. Rev. Lett.*, 99:236401, 2007.

[51] J. N. Reimers and A. J. Berlinsky. Order by disorder in the classical Heisenberg kagome antiferromagnet. *Phys. Rev. B*, 48:9539–9554, 1993.

[52] G. F. H. Smith. Paratacamite, a new oxychloride of copper. *Mineral. Mag.*, 14(65):170–177, 1906.

[53] R. S. W. Braithwaite, K. Mereiter, W. H. Paar, and A. M. Clark. Herbertsmithite, $Cu_3Zn(OH)_6Cl_2$, a new species, and the definition of paratacamite. *Mineral. Mag.*, 68(3):527–539, 2004.

[54] P. Mendels, F. Bert, M. A. de Vries, A. Olariu, A. Harrison, F. Duc, J. C. Trombe, J. S. Lord, A. Amato, and C. Baines. Quantum magnetism in the paratacamite family: Towards an ideal kagome lattice. *Phys. Rev. Lett.*, 98:077204, 2007.

[55] M. R. Norman. Colloquium: Herbertsmithite and the search for the quantum spin liquid. *Rev. Mod. Phys.*, 88:041002, 2016.

[56] M. J. Harris, S. T. Bramwell, D. F. McMorrow, T. Zeiske, and K. W. Godfrey. Geometrical frustration in the ferromagnetic pyrochlore $Ho_2Ti_2O_7$. *Phys. Rev. Lett.*, 79:2554–2557, 1997.

[57] P. W. Anderson. Resonating valence bonds: A new kind of insulator? *Mater. Res. Bull.*, 8(2):153 – 160, 1973.

[58] W. F. Giauque and M. F. Ashley. Molecular rotation in ice at 10 K. Free energy of formation and entropy of water. *Phys. Rev.*, 43:81–82, 1933.

[59] W. F. Giauque and J. W. Stout. The entropy of water and the third law of thermodynamics. The heat capacity of ice from 15 to 273 K. *J. Am. Chem. Soc.*, 58(7):1144–1150, 1936.

[60] L. Pauling. The structure and entropy of ice and of other crystals with some randomness of atomic arrangement. *J. Am. Chem. Soc.*, 57(12):2680–2684, 1935.

[61] J. D. Bernal and R. H. Fowler. A theory of water and ionic solution, with particular reference to hydrogen and hydroxyl ions. *J. Chem. Phys.*, 1(8):515–548, 1933.

[62] C. Castelnovo, R. Moessner, and S. L. Sondhi. Spin ice, fractionalization, and topological order. *Annu. Rev. Conden. Ma. P.*, 3(1):35–55, 2012.

[63] E. O. Wollan, W. L. Davidson, and C. G. Shull. Neutron diffraction study of the structure of ice. *Phys. Rev.*, 75(9):1348, 1949.

[64] J. C. Li, V. M. Nield, D. K. Ross, R. W. Whitworth, C. C. Wilson, and D. A. Keen. Diffuse neutron-scattering study of deuterated ice Ih. *Philos. Mag. B*, 69(6):1173–1181, 1994.

[65] A. P. Ramirez, A. Hayashi, R. J. Cava, R. Siddharthan, and B. S. Shastry. Zero-point entropy in spin ice. *Nature*, 399:333–335, 1999.

[66] P. Dirac. Quantised singularities in the electromagnetic field. *P. Roy. Soc. A. Math. Phy.*, 133, 1931.

[67] D. Fryberger, S. St. Lorant, E. Tillmann, and A. Wolff. Magnetic monopole detector with sensitivity to extremely small magnetic charge. *Rev. Sci. Instrum.*, 57(10):2577–2583, 1986.

[68] K. A. Milton. Theoretical and experimental status of magnetic monopoles. *Rep. Prog. Phys.*, 69(6):1637, 2006.

[69] C. Castelnovo, R. Moessner, and S. L. Sondhi. Magnetic monopoles in spin ice. *Nature*, 451:42–45, 2008.

[70] T. Fennell, P. P. Deen, A. R. Wildes, K. Schmalzl, D. Prabhakaran, A. T. Boothroyd, R. J. Aldus, D. F. McMorrow, and S. T. Bramwell. Magnetic Coulomb phase in the spin ice $Ho_2Ti_2O_7$. *Science*, 326(5951):415–417, 2009.

[71] D. J. P. Morris, D. A. Tennant, S. A. Grigera, B. Klemke, C. Castelnovo, R. Moessner, C. Czternasty, M. Meissner, K. C. Rule, J. U. Hoffmann, K. Kiefer, S. Gerischer, D. Slobinsky, and R. S. Perry. Dirac strings and magnetic monopoles in the spin ice $Dy_2Ti_2O_7$. *Science*, 326(5951):411–414, 2009.

[72] E. F. Shender. Antiferromagnetic garnets with fluctuationally interacting sublattices. *Sov. Phys. JETP*, 56:178–184, 1982.

[73] K. A. Ross, Y. Qiu, J. R. D. Copley, H. A. Dabkowska, and B. D. Gaulin. Order by disorder spin wave gap in the XY pyrochlore magnet $Er_2Ti_2O_7$. *Phys. Rev. Lett.*, 112:057201, 2014.

[74] Y. J. Kim, A. Aharony, R. J. Birgeneau, F. C. Chou, O. Entin-Wohlman, R. W. Erwin, M. Greven, A. B. Harris, M. A. Kastner, I. Ya. Korenblit, Y. S. Lee, and G. Shirane. Ordering due to quantum fluctuations in $Sr_2Cu_3O_4Cl_2$. *Phys. Rev. Lett.*, 83:852–855, 1999.

[75] J. D. M. Champion, M. J. Harris, P. C. W. Holdsworth, A. S. Wills, G. Balakrishnan, S. T. Bramwell, E. Čižmár, T. Fennell, J. S. Gardner, J. Lago, D. F. McMorrow, M. Orendáč, A. Orendáčová, D. McK. Paul, R. I. Smith, M. T. F. Telling, and A. Wildes. $Er_2Ti_2O_7$: Evidence of quantum order by disorder in a frustrated antiferromagnet. *Phys. Rev. B*, 68:020401, 2003.

[76] L. Savary, K. A. Ross, B. D. Gaulin, J. P. C. Ruff, and Balents L. Order by quantum disorder in $Er_2Ti_2O_7$. *Phys. Rev. Lett.*, 109:167201, 2012.

[77] P. A. McClarty, P. Stasiak, and M. J. P. Gingras. Order-by-disorder in the XY pyrochlore antiferromagnet. *Phys. Rev. B*, 89:024425, 2014.

[78] Y. J. Kao, M. Enjalran, A. Del Maestro, H. R. Molavian, and Michel J. P. Gingras. Understanding paramagnetic spin correlations in the spin-liquid pyrochlore $Tb_2Ti_2O_7$. *Phys. Rev. B*, 68:172407, 2003.

[79] J. P. C Ruff, B. D. Gaulin, J. P. Castellan, K. C. Rule, J. P. Clancy, J. Rodriguez, and H. A. Dabkowska. Structural fluctuations in the spin-liquid state of $Tb_2Ti_2O_7$. *Phys. Rev. Lett.*, 99(23):237202, 2007.

[80] J. Snyder, J. S. Slusky, R. J. Cava, and P. Schiffer. How spin ice freezes. *Nature*, 413(6851):48–51, 2001.

[81] L. Balents. Spin liquids in frustrated magnets. *Nature*, 464:199–208, 2010.

[82] J. S. Gardner, S. R. Dunsiger, B. D. Gaulin, M. J. P. Gingras, J. E. Greedan, R. F. Kiefl, M. D. Lumsden, W. A. MacFarlane, N. P. Raju, J. E. Sonier, I. Swainson, and Z. Tun. Cooperative paramagnetism in the geometrically frustrated pyrochlore antiferromagnet $Tb_2Ti_2O_7$. *Phys. Rev. Lett.*, 82:1012–1015, 1999.

[83] J. S. Gardner, A. Keren, G. Ehlers, C. Stock, Eva Segal, J. M. Roper, B. Fåk, M. B. Stone, P. R. Hammar, D. H. Reich, and B. D. Gaulin. Dynamic frustrated magnetism in $Tb_2Ti_2O_7$ at 50 mK. *Phys. Rev. B*, 68:180401, 2003.

[84] J. S. Gardner, B. D. Gaulin, A. J. Berlinsky, P. Waldron, S. R. Dunsiger, N. P. Raju, and J. E. Greedan. Neutron scattering studies of the cooperative paramagnet pyrochlore $Tb_2Ti_2O_7$. *Phys. Rev. B*, 64:224416, 2001.

[85] H. Takatsu, H. Kadowaki, T. J. Sato, J. W. Lynn, Y. Tabata, T. Yamazaki, and K. Matsuhira. Quantum spin fluctuations in the spin-liquid state of $Tb_2Ti_2O_7$. *J. Phys.: Condens. Matter*, 24(5):052201, 2012.

[86] L. Savary and L. Balents. Coulombic quantum liquids in spin-1/2 pyrochlores. *Phys. Rev. Lett.*, 108:037202, 2012.

[87] R. G. Melko, B. C. den Hertog, and M. J. P. Gingras. Long-range order at low temperatures in dipolar spin ice. *Phys. Rev. Lett.*, 87:067203, 2001.

[88] M. J. P. Gingras and B. C. den Hertog. Origin of spin-ice behavior in Ising pyrochlore magnets with long-range dipole interactions: an insight from mean-field theory. *Can. J. Phys.*, 79(11-12):1339–1351, 2001.

[89] S. V. Isakov, R. Moessner, and S. L. Sondhi. Why spin ice obeys the ice rules. *Phys. Rev. Lett.*, 95:217201, 2005.

[90] H. M. Revell, L. R. Yaraskavitch, J. D. Mason, K. A. Ross, H. M. L. Noad, H. A. Dabkowska, P. Henelius B. D. Gaulin, and J. B. Kycia. Evidence of impurity and boundary effects on magnetic monopole dynamics in spin ice. *Nat. Phys.*, 9:34–37, 2013.

[91] G. Sala, M. J. Gutmann, D. Prabhakaran, D. Pomaranski, C. Mitchelitis, J. B. Kycia, D. G. Porter, C. Castelnovo, and J. P. Goff. Vacancy defects and monopole dynamics in oxygen-deficient pyrochlores. *Nat. Mat.*, 13:488–493, 2014.

[92] K. E. Arpino, B. A. Trump, A. O. Scheie, T. M. McQueen, and S. M. Koohpayeh. Impact of stoichiometry of $Yb_2Ti_2O_7$ on its physical properties. *Phys. Rev. B*, 95:094407, 2017.

[93] G. D. Blundred, C. A. Bridges, and M. J. Rosseinsky. New oxidation states and defect chemistry in the pyrochlore structure. *Angew. Makromol. Chem.*, 43(27):3562–3565, 2004.

[94] R. A. Beyerlein, H. S. Horowitz, J. M. Longo, M. E. Leonowicz, J. D. Jorgensen, and F. J. Rotella. Neutron diffraction investigation of ordered oxygen vacancies in the defect pyrochlores, $Pb_2Ru_2O_7$ and $PbT1Nb_2O_6$. *J. Solid State Chem.*, 51(2):253–265, 1984.

[95] G. C. Lau, R. S. Freitas, B. G. Ueland, and B. D. Muegge. Zero-point entropy in stuffed spin-ice. *Nat. Phys.*, 2:249253, 2006.

[96] M. Wakita, T. Taniguchi, H. Edamoto, H. Takatsu, and H. Kadowaki. Quantum spin liquid and electric quadrupolar states of single crystal $Tb_{2+x}Ti_{2-x}O_{7+y}$. *J. Phys.: Conference Series*, 683(1):012023, 2016.

[97] S. M. Koohpayeh, J. J. Wen, B. A. Trump, C. L. Broholm, and T. M. McQueen. Synthesis, floating zone crystal growth and characterization of the quantum spin ice $Pr_2Zr_2O_7$ pyrochlore. *J. Cryst. Growth*, 402:291 – 298, 2014.

[98] E. Kermarrec, D. D. Maharaj, J. Gaudet, K. Fritsch, D. Pomaranski, J. B. Kycia, Y. Qiu, J. R. D. Copley, M. M. P. Couchman, A. O. R. Morningstar, H. A.

Dabkowska, and B. D. Gaulin. Gapped and gapless short-range-ordered magnetic states with $(\frac{1}{2}, \frac{1}{2}, \frac{1}{2})$ wave vectors in the pyrochlore magnet $Tb_{2+x}Ti_{2-x}O_{7+\delta}$. *Phys. Rev. B*, 92:245114, 2015.

[99] H. Takatsu, T. Taniguchi, S. Kittaka, T. Sakakibara, and H. Kadowaki. Quadrupole order in the frustrated pyrochlore magnet $Tb_2Ti_2O_7$. *J. Phys.: Conf. Series*, 683(1):012022, 2016.

[100] K. A. Ross, T. Proffen, H. A. Dabkowska, and J. A. Quilliam. Lightly stuffed pyrochlore structure of single-crystalline $Yb_2Ti_2O_7$ grown by the optical floating zone technique. *Physical Review B*, 86, 2012.

[101] A. Mostaed, G. Balakrishnan, M. R. Lees, Y. Yasui, L. J. Chang, and R. Beanland. Atomic structure study of the pyrochlore $Yb_2Ti_2O_7$ and its relationship with low-temperature magnetic order. *Phys. Rev. B*, 95:094431, 2017.

[102] K. Baroudi, B. D. Gaulin, S. H. Lapidus, J. Gaudet, and R. J. Cava. Symmetry and light stuffing of $Ho_2Ti_2O_7$, $Er_2Ti_2O_7$, and $Yb_2Ti_2O_7$ characterized by synchrotron x-ray diffraction. *Phys. Rev. B*, 92(2):024110, 2015.

[103] L. J. Chang, S. Onoda, Y. Su, Y. J. Kao, K. D. Tsuei, Y. Yasui, K. Kakurai, and M. R. Lees. Higgs transition from a magnetic Coulomb liquid to a ferromagnet in $Yb_2Ti_2O_7$. *Nat. Commun.*, 3:992, 2012.

[104] K. A. Ross, L. R. Yaraskavitch, M. Laver, J. S. Gardner, J. A. Quilliam, S. Meng, J. B. Kycia, D. K. Singh, T. Proffen, H. A. Dabkowska, and B. D. Gaulin. Dimensional evolution of spin correlations in the magnetic pyrochlore $Yb_2Ti_2O_7$. *Phys. Rev. B*, 84:174442, 2011.

[105] S. T. Bramwell, M. N. Field, M. J. Harris, and I. P. Parkin. Bulk magnetization of

the heavy rare earth titanate pyrochlores - a series of model frustrated magnets. *J. Phys.: Condens. Matter*, 12(4):483, 2000.

[106] S. T. Bramwell and M. J. Gingras. Spin ice state in frustrated magnetic pyrochlore materials. *Science*, 294(5546):1495–1501, 2001.

[107] J. P. Clancy, J. P. C. Ruff, S. R. Dunsiger, and Y. Zhao. Revisiting static and dynamic spin-ice correlations in $Ho_2Ti_2O_7$ with neutron scattering. *Phys. Rev. B*, 79:014408, 2009.

[108] K. A. Ross, J. P. Ruff, C. P. Adams, J. S. Gardner, H. A. Dabkowska, Y. Qiu, J. R. Copley, and B. D. Gaulin. Two-dimensional kagome correlations and field induced order in the ferromagnetic XY pyrochlore $Yb_2Ti_2O_7$. *Phys. Rev. Lett*, 103(22):227202, 2009.

[109] S. Onada. Effective quantum pseudospin-1/2 model for Yb pyrochlore oxides. *J. Phys. Conf. Ser*, 320(1):012065, 2011.

[110] K. A. Ross, L. Savary, B. D. Gaulin, and L. Balents. Quantum excitations in quantum spin ice. *Phys. Rev. X*, 1:021002, 2011.

[111] H. W. J. Bløte, R. F. Wielinga, and W. J. Huiskamp. Heat-capacity measurements on rare-earth double oxides $R_2M_2O_7$. *Physica*, 43(4):549 – 568, 1969.

[112] J. A. Hodges, P. Bonville, A. Forget, M. Rams, K. Krolas, and G. Dhalenne. The crystal field and exchange interactions in $Yb_2Ti_2O_7$. *J. Phys.: Condens. Matter*, 13(41):9301, 2001.

[113] J. A. Hodges, P. Bonville, A. Forget, A. Yaouanc, P. Dalmas de Réotier, G. André, M. Rams, K. Krolas, C. Ritter, P. C. M. Gubbens, C. T. Kaiser, P. J. C. King, and

C. Baines. First-order transition in the spin dynamics of geometrically frustrated $Yb_2Ti_2O_7$. *Phys. Rev. Lett.*, 88:077204, 2002.

[114] Y. Yasui, M. Soda, S. Iikubo, M. Ito, M. Sato, N. Hamaguchi, T. Matsushita, N. Wada, T. Takeuchi, and N. Aso. Ferromagnetic transition of pyrochlore compound $Yb_2Ti_2O_7$. *J. Phys. Soc. Jpn*, 72(11):3014–3015, 2003.

[115] J. S. Gardner, G. Ehlers, N. Rosov, R. W. Erwin, and C. Petrovic. Spin-spin correlations in $Yb_2Ti_2O_7$: A polarized neutron scattering study. *Phys. Rev. B*, 70:180404, 2004.

[116] S. T. Bramwell, M. J. Harris, B. C. den Hertog, M. J. Gingras, J. S. Gardner, McMorrow, D.F, A. R. Wildes, A. L. Cornelius, J. D. Champion, R. G. Melko, and T. Fennell. Spin correlations in $Ho_2Ti_2O_7$: a dipolar spin ice system. *Phys. Rev. Lett.*, 87(4):047205, 2001.

[117] H. B. Cao, A. Gukasov, I. Mirebeau, and P. Bonville. Anisotropic exchange in frustrated pyrochlore $Yb_2Ti_2O_7$. *J. Phys.: Condens. Matter*, 21(49):492202, 2009.

[118] L. J. Chang, M. R. Lees, I. Watanabe, A. D. Hillier, Y. Yasui, and S. Onoda. Static magnetic moments revealed by muon spin relaxation and thermodynamic measurements in the quantum spin ice $Yb_2Ti_2O_7$. *Phys. Rev. B*, 89:184416, 2014.

[119] J. Robert, E. Lhotel, G. Remenyi, S. Sahling, I. Mirebeau, C. Decorse, B. Canals, and S. Petit. Spin dynamics in the presence of competing ferromagnetic and antiferromagnetic correlations in $Yb_2Ti_2O_7$. *Phys. Rev. B*, 92:064425, 2015.

[120] B. Z. Malkin, A. R. Zakirov, M. N. Popova, S. A. Klimin, E. P. Chukalina, E. Antic-Fidancev, P. Goldner, P. Aschehoug, and G. Dhalenne. Optical spectroscopy of $Yb_2Ti_2O_7$ and $Y_2Ti_2O_7 : Yb^{3+}$ and crystal-field parameters in rare-earth titanate pyrochlores. *Phys. Rev. B*, 70:075112, 2004.

[121] A. Yaouanc, P. Dalmas de Réotier, C. Marin, and V. Glazkov. Single-crystal versus polycrystalline samples of magnetically frustrated $Yb_2Ti_2O_7$: Specific heat results. *Phys. Rev. B*, 84:172408, 2011.

[122] R. Siddharthan, B. S. Shastry, A. P. Ramirez, and A. Hayashi. Ising pyrochlore magnets: low-temperature properties, 'ice rules' and beyond. *Phys. Rev. Lett.*, 83(9):1854–1857, 1999.

[123] Y. Tokiwa, T. Yamashita, M. Udagawa, S. Kittaka, T. Sakakibara, D. Terazawa, Y. Shimoyama, T. Terashima, Y. Yasui, and T. Shibauchi. Possible observation of highly itinerant quantum magnetic monopoles in the frustrated pyrochlore $Yb_2Ti_2O_7$. *Nat. Comm.*, 7:10807, 2016.

[124] N. Hamachi, Y. Yasui, K. Araki, S. Kittaka, and T. Sakakibara. Ferromagnetic ordered phase of quantum spin ice system $Yb_2Ti_2O_7$ under [001] magnetic field. *AIP Advances*, 6(5):055707, 2016.

[125] R. M. D'Ortenzio, H. A. Dabkowska, S. R. Dunsiger, B. D. Gaulin, M. J. P. Gingras, T. Goko, J. B. Kycia, L. Liu, T. Medina, and T. J. Munsie. Unconventional magnetic ground state in $Yb_2Ti_2O_7$. *Phys. Rev. B*, 88(13):134428, 2013.

[126] P. Dalmas de Rotier, V. Glazkov, C. Marin, A. Yaouanc, P. C. M. Gubbens, S. Sakarya, P. Bonville, A. Amato, C. Baines, and P. J. C. King. Studies of $R_2Ti_2O_7$ (R= Gd and Yb); new results. *Physica B*, 374375:145 – 147, 2006.

[127] E. Lhotel, S. R. Giblin, M. R. Lees, G. Balakrishnan, L. J. Chang, and Y. Yasui. First-order magnetic transition in $Yb_2Ti_2O_7$. *Phys. Rev. B*, 89:224419, 2014.

[128] S. Onoda and Y. Tanaka. Quantum fluctuations in the effective pseudospin-$\frac{1}{2}$ model for magnetic pyrochlore oxides. *Phys. Rev. B*, 83:094411, 2011.

[129] R. Applegate, N. R. Hayre, R. R. P. Singh, T. Lin, A. G. R. Day, and M. J. P. Gingras. Vindication of $Yb_2Ti_2O_7$ as a model exchange quantum spin ice. *Phys. Rev. Lett.*, 109:097205, 2012.

[130] N. R. Hayre, K. A. Ross, R. Applegate, T. Lin, R. R. P. Singh, B. D. Gaulin, and M. J. P. Gingras. Thermodynamic properties of $Yb_2Ti_2O_7$ pyrochlore as a function of temperature and magnetic field: Validation of a quantum spin ice exchange Hamiltonian. *Phys. Rev. B*, 87:184423, 2013.

[131] A. W. C. Wong, Z. Hao, and M. J. P. Gingras. Ground state phase diagram of generic XY pyrochlore magnets with quantum fluctuations. *Phys. Rev. B*, 88:144402, 2013.

[132] A. Yaouanc, P. Dalmas de Réotier, P. Bonville, J. A. Hodges, V. Glazkov, L. Keller, V. Sikolenko, M. Bartkowiak, A. Amato, C. Baines, P. J. C. King, P. C. M. Gubbens, and A. Forget. Dynamical splayed ferromagnetic ground state in the quantum spin ice $Yb_2Sn_2O_7$. *Phys. Rev. Lett.*, 110:127207, 2013.

[133] J. Gaudet, K. A. Ross, E. Kermarrec, N. P. Butch, G. Ehlers, H. A. Dabkowska, and B. D. Gaulin. Gapless quantum excitations from an icelike splayed ferromagnetic ground state in stoichiometric $Yb_2Ti_2O_7$. *Phys. Rev. B*, 93:064406, 2016.

[134] P. Bonville, J. A. Hodges, E. Bertin, J. P. Bouchaud, P. Dalmas de Réotier, L. P. Regnault, H. M. Rønnow, J. P. Sanchez, S. Sosin, and A. Yaouanc. Transitions and spin dynamics at very low temperature in the pyrochlores $Yb_2Ti_2O_7$ and $Gd_2Sn_2O_7$. *Hyperfine Interact.*, 156(1):103–111, 2004.

[135] J. D. Thompson, McClarty, P. A., H. M. Rønnow, and L. P. Regnault. Rods of neutron scattering intensity in $Yb_2Ti_2O_7$: compelling evidence for significant

anisotropic exchange in a magnetic pyrochlore oxide. *Phys. Rev. Lett.*, 86:187202, 2011.

[136] J. D. Thompson, P. A. McClarty, and M. J. P. Gingras. Local susceptibility of the $Yb_2Ti_2O_7$ rare earth pyrochlore computed from a Hamiltonian with anisotropic exchange. *J. Phys.: Condens. Matter*, 23(16):164219, 2011.

[137] E. Kermarrec, J. Gaudet, K. Fritsch, R. Khasanov, Z. Guguchia, C. Ritter, K. A. Ross, H. Dabkowska, and B. Gaulin. Ground state selection under pressure in the quantum pyrochlore magnet $Yb_2Ti_2O_7$. *Nat. Commun.*, 8:14810, 2017.

[138] J. D. Thompson, P. A. McClarty, D. Prabhakaran, I. Cabrera, T. Guidi, and R. Coldea. Quasiparticle breakdown and spin Hamiltonian of the frustrated quantum pyrochlore $Yb_2Ti_2O_7$ in a magnetic field. *Phys. Rev. Lett.*, 119:057203, 2017.

[139] J. Gaudet, D. D. Maharaj, E. Kermarrec, G. Sala, K. A. Ross, H. A. Dabkowska, A. I. Kolesnikov, G. E. Granroth, and B. D. Gaulin. Neutron spectroscopic study of crystalline electric field excitations in stoichiometric and lightly stuffed $Yb_2Ti_2O_7$. *Phys. Rev. B*, 92:134420, 2015.

[140] B. T. M. Willis and C. J. Carlile. *Experimental neutron scattering.* Oxford University Press, 1st edition, 2009.

[141] D. Sivia. *Elementary scattering theory: for X-ray and neutron users.* Oxford University Press, 1st edition, 2011.

[142] L. Schwartz and J. B. Cohen. *Diffraction from materials.* Springer Science & Business Media, 2nd edition, 2013.

[143] SXD. https://www.isis.stfc.ac.uk/Pages/SXD.aspx, Accessed 09 2017.

[144] D. J. P. Morris. *Sodium Ordering and the control of properties in sodium cobaltate*. PhD thesis, University of Liverpool, 2007.

[145] D7 - diffuse scattering spectrometer. https://www.ill.eu/instruments-support/instruments-groups/instruments/d7/description/instrument-layout/, Accessed 09 2017.

[146] V. Petricek, M. Dusek, and L. Palatinus. Crystallographic computing system jana2006: General features. *Z. Kristallogr.*, 229(5):245–352, 2014.

[147] W. Massa. *Crystal structure determination*. Springer Science & Business Media, 1st edition, 2013.

[148] W. Pauli. Über den zusammenhang des abschlusses der elektronengruppen im atom mit der komplexstruktur der spektren. *Zeitschrift für Physik*, 31(1):765–783, 1925.

[149] S. Onoda and Y. Tanaka. Quantum melting of spin ice: Emergent cooperative quadrupole and chirality. *Phys. Rev. Lett.*, 105:047201, 2010.

[150] S. Blundell. *Magnetism In Condensed Matter*. Oxford University Press, 2001 edition, 1967.

[151] B. Tomasello. *A quantum mechanical study of the dynamical properties of spin-ice materials*. PhD thesis, University of Kent, 2014.

[152] A. P. Ramirez. Strongly geometrically frustrated magnets. *Annu. Rev. Mater. Sci.*, 24(1):453–480, 1994.

[153] M. T. Dove. *Structure and dynamics: an atomic view of materials*. Oxford University Press, 1st edition, 2003.

[154] K. W. H. Stevens. Matrix elements and operator equivalents connected with magnetic properties of rare earth ions. *Proc. Phys. Soc.*, 65(209), 1952.

[155] G. C. Lau, B. D. Muegge, T. M. McQueen, E. L. Duncan, and R. J. Cava. Stuffed rare earth pyrochlore solid solutions. *J. Solid State Chem.*, 179(10):3126 – 3135, 2006.

[156] G. C. Lau, R. S. Freitas, B. G. Ueland, M. L. Dahlberg, Q. Huang, H. W. Zandbergen, P. Schiffer, and R. J. Cava. Structural disorder and properties of the stuffed pyrochlore Ho_2TiO_5. *Phys. Rev. B*, 76:054430, 2007.

[157] N. Metropolis and S. Ulam. The Monte Carlo method. *J. Am. Stat. Assoc.*, 44(247):335–341, 1949.

[158] T. R. Welberry and D. J. Goossens. The interpretation and analysis of diffuse scattering using Monte Carlo simulation methods. *Acta Crystallogr., Sect. A: Found. Crystallogr.*, 64(1):23–32, 2008.

[159] D. J. Goossens, A. P. Heerdegen, E. J. Chan, and T. R. Welberry. Monte Carlo modeling of diffuse scattering from single crystals. *Metall. Mater. Trans. A*, 42(1):23–31, 2011.

[160] G. Marsaglia and T. A. Bray. Toward a universal random number generator. *Florida State University Report: FSU-SCRI-87-50*, 1987.

[161] T. R. Welberry. Diffuse x-ray scattering and models of disorder. *Rep. Prog. Phys.*, 48(11):1543, 1985.

[162] T. R. Welberry, M. J. Gutmann, H. Woo, D. J. Goossens, G. Xu, C. Stock, W. Chen, and Z. G. Ye. Single-crystal neutron diffuse scattering and Monte Carlo

study of the relaxor ferroelectric $PbZn_1/3Nb_2/3O_3$ (PZN). *J. Appl. Crystallogr.*, 38(4):639–647, 2005.

[163] M. J. Gutmann. Accelerated computation of diffuse scattering patterns and application to magnetic neutron scattering. *J. Appl. Crystallogr.*, 43(2):250–255, 2010.

[164] S. C. Abrahams. Magnetic and crystal structure of titanium sesquioxide. *Phys. Rev.*, 130:2230–2237, 1963.

[165] A. Scheie, J. Kindervater, S. Säubert, C. Duvinage, C. Pfleiderer, H. J. Changlani, S. Zhang, L. Harriger, K. Arpino, S. M. Koohpayeh, O. Tchernyshyov, and C. Broholm. Reentrant phase diagram of $Yb_2Ti_2O_7$ in a $\langle 111 \rangle$ magnetic field. *Phys. Rev. Lett.*, 119:127201, 2017.

[166] L. D. C. Jaubert and P. C. W. Holdsworth. Signature of magnetic monopole and dirac string dynamics in spin ice. *Nat. Phys.*, 5:258–261, 2009.

[167] K. A. Ross. *Neutron Scattering Studies of the Quantum Spin Ice Material* $Yb_2Ti_2O_7$. PhD thesis, McMaster University, 2012.

[168] T. Goto, Y. B. Cheng, and T. Akatsu. Fabrication of transparent $La_2Zr_2O_7$ by reactive spark plasma sintering. *Key. Eng. Mater.*, 484:135–138, 2011.

[169] H. Yan, O. Benton, L. Jaubert, and N. Shannon. Theory of multiple-phase competition in pyrochlore magnets with anisotropic exchange with application to $Yb_2Ti_2O_7$, $Er_2Ti_2O_7$, and $Er_2Sn_2O_7$. *Phys. Rev. B*, 95:094422, 2017.